Kalman-Filter Design and Evaluation for PMSM Rotor-Temperature Estimation

Daniel Mårtensson

LUND
UNIVERSITY

Department of Automatic Control

MSc Thesis
TFRT-6156
ISSN 0280-5316

Department of Automatic Control
Lund University
Box 118
SE-221 00 LUND
Sweden

Printed in Sweden by Tryckeriet i E-huset
Lund 2022

Abstract

The permanent magnet synchronous motor, PMSM, is an efficient electrical motor that has seen a greater prevalence in the automotive industry from the increasing demand for electrical vehicles. Managing the temperature of the permanent magnet rotor is important to optimize motor utilization and avoid hardware failures. Direct temperature measurements of the moving rotor with a sensor are, however, both difficult and costly and an observer-based approach to estimate the rotor temperature can instead be attained using measured currents, voltages and a model.

The work in this thesis studies observers based on a Kalman Filter, KF, and an extended Kalman filter, EKF. The observability of the system was found to be poor at low rotational speeds and filter designs were implemented that used low-speed estimators, that slowly drive the rotor temperature estimate towards the coolant temperature. For circumstances when the inductance accuracy in the model was limited, EKFs with inductance estimation and gain scheduled noise covariance matrices were also evaluated. There were also potential numerical robustness issues, so normalized and rescaled state variable system descriptions were evaluated.

The simulation analysis of the KFs showed a great reduction in rotor temperature estimation error of roughly 40 °C when using a low-speed estimator, compared to without the use of a low-speed estimator. In circumstances with limited inductance accuracy, the EKF with inductance estimation had a maximum temperature estimation error magnitude of $\approx 2.5\,^{\circ}\mathrm{C}$ compared to $\approx 11\,^{\circ}\mathrm{C}$ of the KF design. Using an EKF with lower sampling frequency and gain scheduling did, however, come at the cost of robustness. Normalizing or rescaling state variables had a visible effect on the noise covariance settings but did not show noticeable improvements of the computational robustness in a simulation environment with high numerical precision.

The thesis was concluded with a brief analysis using measurement from a real but different motor model. The worst case estimation error magnitudes was approximately 12 °C for the rotor temperature. The estimation results were very sensitive to model parameter accuracy and more testing has to be conducted using experimental data, but the results presented show some promise.

Acknowledgements

I would like to express my sincerest gratitude to all my supervisors for the help they have provided me. I am profoundly grateful for the guidance of my industrial supervisors at BorgWarner, Gabriel Turesson and Peter Jonsson, and my academic supervisor Björn Olofsson from the Department of Automatic Control, for his valuable feedback. I would also like to thank my family for all the support. This project would not have been possible without the aid I received.

Contents

List of Abbreviations and Symbols

λ	Flux Linkage [Wb-turns]
λ_{m0}	Flux linkage operating point reference [Wb-t].
P_{pole}	Number of magnetic pole pairs.
θ	Electrical angle [rad].
L_s	Average per phase stator self-inductance [H].
L_m	Stator self and mutual inductance fluctuations [H].
M_s	Average mutual inductances between stator windings [H].
δ	Load angle [°].
ω_m	Angular mechanical rotor speed [rad/s].
ω_e	Angular electrical rotor speed [rad/s].
τ	Torque [Nm].
I	Current [A].
L	Inductance [H].
V	Voltage [V].
T_r	Permanent magnet rotor temperature [°C].
T_0	Permanent magnet rotor temperature operating point reference [°C].
B_r	Permanent magnet remanent flux density temperature coefficient [1/°C].
T_s	Stator temperature [°C].
T_{s0}	Stator temperature operating point reference [°C].
T_c	Coolant temperature [°C].
R_s	Stator resistance [Ω].
R_{m0}	Stator resistance operating point reference [Ω].
α_R	Resistance temperature coefficient [1/°C].
T_c	Coolant temperature [°C].
u_a, u_b, u_c	Voltages of a three-phase system [V].
e_a, e_b, e_c	The induced voltages of a three-phase system [V].
$\alpha\beta$	Index indicates orthogonal two-axis reference frame.
abc	Index indicates three-phase reference frame.

dq	Index indicates rotating direct and quadrature two-axis reference frame.
h	Sampling time [s].
A	System matrix.
B	Input matrix.
C	Output matrix.
D	Feed-forward matrix.
Φ	Discrete-time state transition matrix
Γ	Discrete-time input matrix.
x	State vector.
y	Output vector.
u	Input vector.
e	Measurement noise.
v	Process noise.
ε	Innovation term.
S	Innovation term covariance matrix.
Q	Process noise covariance matrix.
R	Measurement noise covariance matrix.
K	Observer gain.
k_R	Gain applied to noise covariance matrix R.
P	Estimation error covariance matrix.
f	Non-linear state transition function.
F	Jacobian of the state transition function f.
h	Non-linear state observation function.
H	Jacobian of the state observation function h.
σ	Standard deviation. A subscript is often employed of the state it refers to, e.g. σ_{L_d} is the standard deviation of the direct axis inductance.
$\kappa()$	Condition number of a matrix.
$\mathcal{O}$	Observability matrix.
$\mathcal{O}_x$	Observability Gramian.
σ_1, σ_r	The largest and smallest singular values of a matrix.
τ_m	Permanent magnet temperature time-constant [s].
τ_L	Inductance time-constant [s].
τ_{LP}	First-order low-pass filter time-constant [s].
$\|\|x\|\|_1$	L_1-norm of a vector x.
PMSM	Permanent Magnet Synchronous Motor.
PM	Permanent Magnet.
RL-circuit	Resistance and inductance circuit.
KF	Kalman filter.
EKF	Extended Kalman filter.
LP	Low-pass.
(back-) EMF	Electromotive force

DC	Direct current
PWM	Pulse-width modulation
LUT	Lookup table
DARE	Discrete-time algebraic Riccati equation
LPV	Linear parameter varying.
SD	Standard deviation.
LPTM	Lumped parameter thermal model.
FEA	Finite element analysis.
CFD	Computational fluid dynamics.
NEDC	New European Driving Cycle.
WLTC	Worldwide harmonized Light-duty vehicle Test Cycles.
CDC	City Driving Cycle.

1

Introduction

1.1 Motivation

The permanent magnet synchronous motor, PMSM, is a synchronous electric motor that is driven by alternating current with field excitation from a permanent magnet rotor [Linquip Technews, 2021]. The PMSM has traditionally been found in high-performance servo applications like the industrial robotics industry. The PMSM is an attractive choice for their quick dynamics and high precision of control, which has lead to their expanded use in a wide variety of fields. The lack of current for magnetization also leads to a highly efficient motor that has a high torque density [Alaküla et al., 2013]. However, operating a PMSM requires a control system utilizing sinusoidal waveforms. One such technique to produce optimal torque is through Field-Oriented Control, a common practice for PMSMs in the automotive industry [Linquip Technews, 2021]. The analysis in this thesis is mainly intended for PMSMs in battery electrical vehicles, BEV, and hybrid electric vehicles, HEV.

To achieve a high degree of utilization, there is, however, an associated cost in the form of high-quality sensor data. One of the important variables for maintaining high performance is the rotor temperature. The rotor temperature affects torque because of its effect on rotor demagnetization. To avoid unsafe operating temperatures that could lead to hardware failure, the rotor temperature can also be used as an input to a thermal management control system. Excessive rotor temperature can also lead to permanent demagnetization. Direct measurement of the rotor temperature with a sensor is both difficult to implement and costly [Wallscheid et al., 2017]. There is, however, more easily available sensor information such as motor currents and the voltage controller references, which could be used to estimate the rotor temperature with an observer based on modeled motor characteristics.

Scientific Background

Sensorless state estimation of PMSMs is a extensively researched topic. Originally, the PMSM was common in high precision servo systems with intricate sensor installations but has expanded to the Adjustable Speed Drives market, which includes

the automotive industry, because of its energy efficiency [Bojoi et al., 2013]. Position sensors are expensive to install and not always reliable in harsh operating environments. Because of the difficulty associated with direct measurements on the moving rotor, obtaining rotor position, flux linkage, and temperature can be problematic [Bojoi et al., 2013]. It might also be beneficial to retain the sensors and use the sensorless estimation as back-up to aid in the detection of hardware failures. Sensorless PMSM schemes refer to methods that do not have sensors for direct measurements on the rotor. Measured currents and voltage references can instead be used for estimation of PM flux linkage, and in turn rotor temperature, with the use of a mathematical model of the motor. The reason for using current measurements and voltage references is because these quantities are already available and used by the PMSM current controller.

There are many different sensorless methods and a way to divide the approaches is by categorizing them by direct and passive methods. A direct approach is by utilizing some form of signal injection to extract state information [Bojoi et al., 2013]. Disrupting the control signal is, however, in opposition to the overarching goal of the thesis of maintaining a high level of accuracy in the control. Signal injection methods are generally more applicable at lower speeds, where the PM thermal stress tends to be low and therefore not as interesting to analyze. It also comes with disadvantages such as reduced efficiency and torque harmonics [Wallscheid et al., 2017]. Comprehensive background information regarding the topic of sensorless control of PMSM motors can be found in [Bojoi et al., 2013]. The methods found in [Kumar et al., 2014] are developed for induction motors but the paper gives nevertheless a good overview of Model Reference Adaptive techniques for state estimation in electric motors. The techniques reviewed in that paper concerns sensorless vector-control strategies. It is also stated in that paper that variations of important induction motor parameters across the operating range, such as the stator and rotor resistances, inhibit accurate speed estimations. The article also remarks on that some of the more advanced techniques to account for parameter variations include the integration of machine learning. In [Ichikawa et al., 2006], they instead try to correct for position estimation errors caused by deviations of the inductances for synchronous reluctance motors and an extended motor model for inductance compensation caused by magnetic saturation is presented. An Extended Kalman Filter, EKF, for stator flux linkage estimation with an augmented state vector that includes inductances can be found in [Vyncke et al., 2010]. The proposed observer was used for direct torque control (DTC) of a PMSM by controlling the stator flux linkage vector, where added parameter estimations are evaluated for both isotropic and anisotropic motors. Isotropy refers to the characteristic of uniformity in different directions as opposed to anisotropy which refers to property dissimilarities along different axes. In the context of electrical motors, the an/-isotropic characteristic concerns the reluctance along different axes [Vyncke et al., 2010]. The article also highlighted the possibility of introducing inverted inductances in the model for reducing the complexity of partial differentiation.

An overview of a few issues for rotor-temperature estimation, which includes low-speed operations, inverter model inaccuracies and some proposed solutions can be found in [Wallscheid et al., 2017]. Temperature management is an important factor in optimizing motor utilization and reducing the risk of destroying insulation varnish and to prevent irreversible permanent magnet demagnetization. It can also help alleviate thermal stress that might reduce motor lifetime. The article also emphasizes that sensor-based temperature measurement on rotating motor parts can be costly and difficult and that accurate models involving finite element analysis or computational fluid dynamics might be inapt for real-time monitoring. A different method for inductance estimation through an affine projection of the motor model is used in [Cho et al., 2018], where an adaptive model is used for flux linkage estimation to the purpose of torque compensation. The increase in rotor permanent magnet temperature is observed as a decrease of the magnetic flux linkage, which in turn decreases the torque. A rotor temperature estimation with neural-network techniques to handle inductance uncertainty and low-speed estimation can be found in [Ding et al., 2020], where the temperature estimation is motivated by safe and efficient drive operation. Fuzzy control is used as part of the adaptation mechanism in that approach.

1.2 Objectives

The focus of this thesis is a passive and indirect approach to rotor temperature estimation by utilizing an observer with current and voltage measurements. Attempts to estimate the torque will also be performed alongside the PM temperature, using the flux linkage estimation. The actuation torque is an important quantity for regulating the motor and even with the presence of torque measurement sensors, the torque estimation can be useful as a backup or for error-detection in hardware. A common method for state estimation is the Kalman filter. The Kalman filter can be described as an optimal estimator for linear systems with Gaussian noise assumptions [Gustafsson, 2012]. There are, however, flux linkage observability issues at low-speed operating points or when fully stopped. The motor model is also affected by parameter-varying characteristics from varying motor speed and magnetic saturation, which introduces further difficulty in accurate state estimation [Wallscheid et al., 2017]. Because of these issues, the standard Kalman filter might not be directly applicable. There are a multitude of different approaches and research on how to deal with these issues [Bojoi et al., 2013]. The current state-of-the-art research is primarily on augmenting the more traditional approach of state observers with some form of machine learning [Ding et al., 2020]. For this thesis, external environmental temperature measurements are already assumed to exist and the estimator is expected to make use of this for low flux linkage observability compensation, which was a solution inspired by [Wallscheid et al., 2017]. The objective of this thesis is to provide a basis for decision-making of observer design through

analysis and comparisons of different state-estimation schemes of rotor temperature estimation.

Important considerations for the evaluation include:

- The ability to deal with potential observability problems at certain operating points and limited, non-persistent excitation.
- Sensitivity to model parameter uncertainty.
- Investigate for possible relationships between the optimal observer gain and the operating speed.
- Computational and memory demand. This includes, e.g., performance evaluations with different filter sampling frequencies.

1.3 Delimitations

There are a variety of different adaptive schemes and sensorless flux-estimation techniques that deal with the issues concerning both low-speed operating points and standstill for observer-based methods and the parameter-varying characteristics of PMSM. To limit the scope of the thesis, certain restrictions are placed on the adaptive schemes. One such restriction includes machine-learning methods because of their significant difference in approach to development. This thesis is also limited to not study methods based on Lumped Parameter Thermal Modeling, LPTM, even though it is a non-invasive technique used for temperature estimation [Wallscheid et al., 2017]. A LPTM of the PMSM typically requires a larger amount of parameters compared to the proposed Kalman filter. If the parameters of the LPTM are unknown they also have to be identified. An example of a LPTM model of the PMSM can be found in [Touhami et al., 2017].

1.4 Methods/Outline

The approach chosen to estimate rotor temperature is based on utilizing the relationship between rotor flux linkage and temperature. Calculations are usually most easily done in a rotating reference frame, a direct-quadrature (dq) model of the PMSM, which can be obtained by applying a Clarke and Park transformation on the standard three-phase system [Bojoi et al., 2013]. The flux linkage can then be estimated with a Kalman filter design. The PMSM can be modeled as a linearly parameter varying system, LPV-system, with rotor speed as the varying parameter. As a baseline approach, the flux linkage is estimated with a Kalman filter with accurate inductance information. The inductance accuracy was found to be important for estimation performance, which resulted in the development and testing of EKF

designs that augmented the state estimation vector with inductances, for circumstances where only limited or poor inductance accuracy is available.

The outline of the thesis follows:

- 2. Modeling Introduction
  - Introducing and deriving the PMSM model used for state estimation.
  - Introducing other important equations later used during the simulation.
  - Background on the more advanced and detailed model used to generate reference signal data for the simulation analysis.
- 3. State Estimation Theory
  - Detailing the model discretization methods.
  - A description of the Kalman filter and the extended Kalman filter.
  - Defining the observability attribute of a system, along with a description of the observability Gramian.
- 4. Kalman Filter Design
  - Analysis to determine a suitable sampling frequency.
  - Preliminary analysis on how the system behaves with varying rotor speeds.
  - Observability analysis, for determining troublesome operating regions.
  - A presentation of the different Kalman filter designs used during the simulation analysis.
- 5. Kalman Filter Simulation Study
  - An evaluation of the different designs and features introduced in the Kalman filter design section, as well as possible effects of the calibration.
  - Sensitivity analysis of the different model parameters and input signals.
- 6. Extended Kalman Filter Design
  - Description of the process of discretizing and analytically differentiating the system.
  - Preliminary analysis to guide the design.
  - Presentation of the different designs used during the simulation study.
- 7. Extended Kalman Filter Simulation Study
  - Evaluation of the different designs, features and calibrations.

  - Comparison between the extended Kalman filter with inductance estimation and a Kalman filter design with limited inductance information.

- 8. Measurement Data Study

  - Brief experimental setup description and the results of an analysis conducted with measurement data from a real, but different e-machine than the one used in the simulation study.

- 9. Conclusion and Future Work

2

Modeling

2.1 Introduction to PMSM Model

The PMSM is customarily driven as a three-phase electrical machine with the alternating currents in the stator windings generating a combined rotating magnetic field with a rotational frequency proportional to the frequency of the currents. The term synchronous originates from the proportionality. The PMSM generates torque by the rotor's own magnetic flux from the permanent magnet aligning itself with the rotating flux axis generated by the stator windings. The number of magnetic pole pairs, P_{pole}, the rotor has, determine the relation between the mechanical and electrical angular speed. To transition between the mechanical, ω_m, and electrical, ω_e, angular speed, the following relation is used:

$$\omega_e = P_{pole}\omega_m \tag{2.1}$$

The angle between the stator and rotor flux axis is called the load angle, denoted δ, and the relation between torque τ and the load angle can be described with:

$$\tau \propto \sin(\delta) \tag{2.2}$$

This means that at no load, δ is close to 0. At maximum torque, the load angle is instead at $\delta = 90°$. Greater load angles, $\delta > 90°$, will lead to loss of synchronicity [Alaküla et al., 2013]. Another way to generate torque is by creating non-uniform air gaps in the rotor. This design characteristic leads to salient motors. The airgaps in the rotor have an increased reluctance, which inhibits the flow of magnetic flux. By placing the airgaps strategically, the rotor will align itself to minimize the reluctance under the centers of poles and moving the airgaps to be between poles instead. This non-uniform flux distribution does unfortunately also lead to oscillations, torque ripples, during operation [Linquip Technews, 2020].

Thermal PMSM Modelling

Very accurate thermal PMSM models can be created using methods of finite element analysis, FEA, or computational fluid dynamics, CFD, the downside being that they

are incredibly computationally demanding [Bojoi et al., 2013]. For practical runtime rotor temperature estimations, the motor in this thesis is instead modeled by a simplified dynamic equivalent RL-circuit. The equivalent circuit model is the basis of the model to be employed as the state dynamics. The actual state being estimated using the circuit model is the flux linkage λ. Flux linkage is the combined contribution of the magnetic flux from the PM passing through all the windings in the motor [Alaküla et al., 2013]. Flux linkage is dependent on the PM temperature and this relation is utilized to estimate the rotor temperature. The details can be found in Section 2.4.

2.2 PMSM Equivalent Circuit Model

The PMSM motor can be modeled as a three-phase system, where each phase *abc* is separated by 120°. An equivalent RL-circuit can be used to model one of the phases with the phase voltage u_a across the stator winding as shown in Figure 2.1. The resistor R_a models the voltage drop over the cables and windings, and the inductance L_a models the stator winding currents own contribution to flux linkage. The voltage e_a is the induced voltage caused by the rotating permanent magnet, where the polarity of the induced voltage is chosen to oppose the applied voltage that caused it, as stated by Lenz's law [Cheng, 1989]. This induced voltage is sometimes also referred to as the back-EMF. The equation for how the induced voltage is related to the flux linkage of the PM rotor, λ_m, and rotor speed, ω, is based on Faraday's law of induction [Alaküla et al., 2013] and is given by:

$$e_a = \omega \lambda_m \tag{2.3}$$

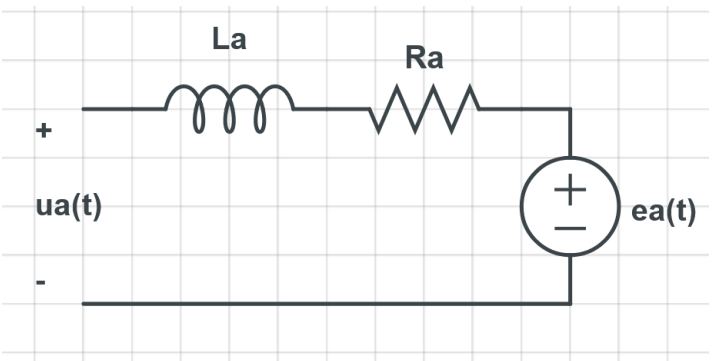

Figure 2.1: An equivalent RL-circuit of phase A.

The resulting voltage equation derived from the equivalent circuit is then given by:

$$u_a = R_a i_a + L_a \frac{di_a}{dt} + \omega \lambda_m \tag{2.4}$$

The three-phase signals can be represented using vectors in a complex plane, perpendicular to the motor axis, placed at the origin. With a stationary complex reference frame, the equivalent circuit can be represented in a vector model with sinusoidal-shaped coordinates for the electrical quantities [Alaküla et al., 2013]. The three-phase equivalent circuit model is useful for an intuitive understanding of the model derivation, but it is not the final model used in the implementation. There is, for instance, another important part in fully deriving the inductance L_a in the equivalent circuit in Figure 2.1. The total inductance for each phase-equivalent circuit is the sum of the self- and mutual inductances, where the self-inductance denotes the effect the current through a conductor winding has on itself and the mutual induction is the contribution of the change in current from other nearby conductors [Cheng, 1989]. This results in a combination of 5 separate, self- and mutual inductances to keep track of for a three-phase equivalent system, which also vary as a function of the electrical rotor angle [MathWorks, n.d.(c)]. In Section 2.3, a transformation into a two-phase dq-reference frame is explained, which alleviates the concern of keeping track of the rotor angle for state estimation.

2.3 dq-model

Clarke and Park transformations can be applied to the three-phase system model to facilitate vector control of electrical quantities. A Clarke transformation converts the stationary three-phase *abc*-reference frame to an orthogonal two-axis $\alpha\beta$-frame. The transformation matrix to convert between the different vector quantities is given by [MathWorks, n.d.(b)]:

$$\begin{bmatrix} \alpha \\ \beta \end{bmatrix} = \frac{2}{3} \begin{bmatrix} 1 & -\frac{1}{2} & -\frac{1}{2} \\ 0 & \frac{\sqrt{3}}{2} & -\frac{\sqrt{3}}{2} \end{bmatrix} \begin{bmatrix} a \\ b \\ c \end{bmatrix} \tag{2.5}$$

$\alpha\beta$, dq, and abc refer to the electromagnetic vector quantities such as current, voltage or magnetic flux in their respective reference frames. Figure 2.2 illustrates how the vector quantities transform in the complex plane and develop in time and the illustration is inspired by [MathWorks, n.d.(b)]. The Park transformation

$$\begin{bmatrix} d \\ q \end{bmatrix} = \begin{bmatrix} \cos(\theta) & \sin(\theta) \\ -\sin(\theta) & \cos(\theta) \end{bmatrix} \begin{bmatrix} \alpha \\ \beta \end{bmatrix} \tag{2.6}$$

depicts the conversion from $\alpha\beta$-quantities to a direct and quadrature, dq-reference, frame that rotates with the speed of the rotor. The transformation matrix chosen and shown in (2.6) is for an initial alignment between the a and d axes,

where θ is the electric angle between the a and d axes alignment and follows the rotor position angle in the rotating dq-reference frame [MathWorks, n.d.(a)].

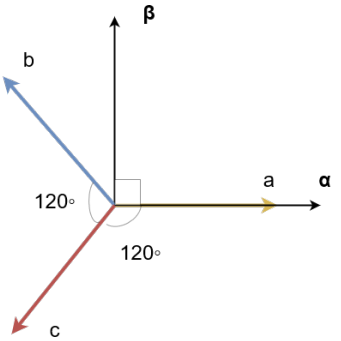

(a) The vector quantities of abc and $\alpha\beta$ in the complex plane.

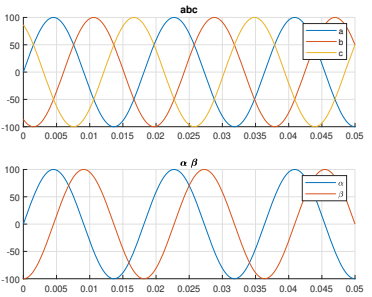

(b) The time-response of the quantities in the abc and $\alpha\beta$ systems.

Figure 2.2: Clarke transformation.

The relation between the reference frame and the magnetic flux of the motor is such that the d-axis is aligned with the rotors permanent magnet flux axis λ_m [Štulrajter et al., 2007].

Utilizing the Clarke and Park transformations in sequence, changes the time-varying quantities in the system equations of the state-space dynamics to time-invariant ones. The transformation of the vector quantities in the complex plane and their respective time-responses can be found in Figure 2.3, with inspiration taken from [MathWorks, n.d.(a)].

Under the assumption of a balanced symmetrical system, the zero sequence has been excluded in the two-axis reference frames, as it is only expected to be equal to 0 [MathWorks, n.d.(a)]. The dq-reference equivalent circuit voltage equations, rearranged in a suitable structure for the state dynamics is given by [MathWorks, n.d.(c)]:

$$\begin{aligned} \frac{dI_d}{dt} &= \frac{1}{L_d}(-R_s I_d + \omega_e L_q I_q + V_d) \\ \frac{dI_q}{dt} &= \frac{1}{L_q}(-\omega_e L_d I_d - R_s I_q - \omega_e \lambda_m + V_q) \end{aligned} \tag{2.7}$$

The definition of the d-axis inductance L_d and the q-axis inductance L_q is given by:

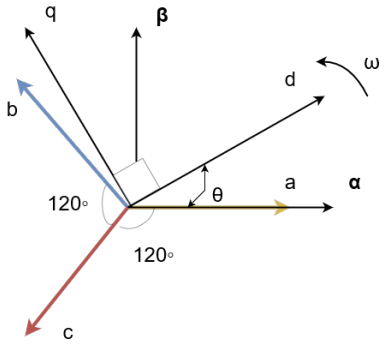

(a) The vector quantities of abc, $\alpha\beta$ and dq in the complex plane.

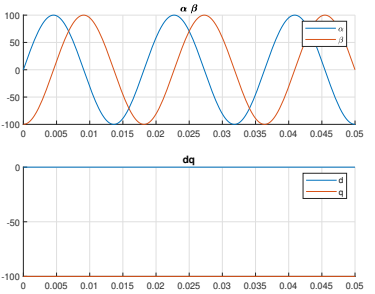

(b) The time-response of the quantities in the $\alpha\beta$ and dq systems.

Figure 2.3: Park transformation.

$$L_d = L_s + M_s + \frac{3}{2}L_m \tag{2.8}$$
$$L_q = L_s + M_s - \frac{3}{2}L_m$$

where R_s is the equivalent resistance of each stator winding, I_d, I_q are the currents, and V_d, V_q are the voltages of the d and q axis, respectively. The variable λ_m refers to the permanent magnet flux linkage, and L_s is the average per phase stator self-inductance. L_m is the stator self- and mutual inductance fluctuation and M_s is the average mutual inductance between the stator windings [MathWorks, n.d.(c)].

To find the rotor torque τ for a given flux linkage, the following equation is applied [MathWorks, n.d.(c)]:

$$\tau = \frac{3}{2}P_{pole}(\lambda_m I_q + (L_d - L_q)I_d I_q) \tag{2.9}$$

In the torque equation, it is also possible to identify the two different components that contribute to the ability of the motor to generate torque. The first term in (2.9) is from the PM magnetization and the second term is from the reluctance difference between the d and q axes. The unit for magnetic reluctance is defined as inverse Henry [Cheng, 1989].

2.4 Parameter Temperature Dependence

Rotor Temperature

The output from the PMSM state estimation model is the PM magnetic flux linkage, λ_m, which ultimately only is useful as an intermediary state. The desired final

quantities used for evaluation are rotor temperature and torque. To convert between flux linkage and rotor temperature, equation (2.10) is used, which is based on a linearized relationship between the two quantities at well parameterized reference points.

$$\lambda_m = \lambda_{m0}(1 + B_r(T_r - T_0)) \tag{2.10}$$

Here, λ_m is the magnetic flux linkage of the PM rotor and λ_{m0} is instead the value at the well known operating point. The rotor temperature is similarly classified in a current PM temperature estimate, T_r, and the reference operating point T_0. The parameter B_r is the PM remanent flux density temperature coefficient [Wallscheid et al., 2017].

Stator Resistance

Either a stator temperature measurement or estimate is assumed to be available during run-time operations. Unlike the rotor temperature, stator temperature is easier to measure because of its lack of movement during operation. It is also a useful variable for overheat protection and resistance calculation. To take advantage of the stator temperature measurement signal, equation

$$R_s = R_{s0}(1 + \alpha_R(T_s - T_{s0})) \tag{2.11}$$

is used to compensate for the temperature dependence on stator winding resistance R_s, where similar to equation (2.10) R_{s0} is a parameterized reference resistance at the reference temperature T_{s0}, and T_s is the stator temperature. The resistance temperature coefficient of the winding is given by α_R and is determined by the material of the conductor [MathWorks, n.d.(d)].

2.5 PMSM Model Assumptions and Uncertainties

For high-performance systems, it is important to have accurate knowledge of all motor parameters, which can be tricky for PMSMs because parameters tend to vary around different operating points. The relation between flux and current is non-linear and for practical applications, lookup tables or LUTs, are commonly employed to find the inductance of a certain working point as a function of speed and torque. This non-linearity is partly because of the magnetic saturation of the rotor, when an increase in external magnetic fields stops increasing the material magnetization further, and all domains of the material, are practically already aligned. Salient motors have the additional property of an anisotropic rotor. The non-uniform air gaps cause the reluctance, and in turn inductance, along distinct phase axes to differ [Vyncke et al., 2010].

The reason PMSM motors experience a decrease in flux linkage and consequently in torque during operation, is because of the rotor core losses, which are

results of the permanent magnetic rotor being subjected to time-varying magnetic fields. These losses are lower compared to other types of losses, but also highly dependent on rotor speed and can end up having a tremendous effect on maximum achievable speeds. The two main culprits for core losses can be explained with hysteresis and eddy current loss effects [Zarei et al., 2012]. Hysteresis losses refer to the energy that is lost during the constant redirection of the magnetic domains of the PM rotor when the flux axis is changed. Eddy currents generate losses when the conducting materials in the rotor induce electromagnetic force that opposes the magnetic flux it is exposed to [Zarei et al., 2012]. This reduction of the flux linkage is what the estimation hopefully captures and what ultimately accounts for the rotor losses and the resulting rotor temperature increase.

The model neglects the effects of space harmonics in air-gaps [Zarei et al., 2012]. Another neglected effect is the skin effect, referring to the conductor property differences at high frequencies, that leads to increased resistances [Cheng, 1989]. To run the PMSM at different speeds, a pulse-width modulation (PWM) inverter feeds the motor with voltages at varying frequencies. The inverter switches the DC voltages on and off at a high frequency to create a phase voltage that also varies in frequency [Alaküla et al., 2013]. The errors that arise from a PWM inverter generating imperfect three-phase sinusoidal voltage are also neglected.

2.6 Motor-CAD Model

A more advanced and complete model was used for performance evaluations of the state-estimation model. The model performed more computationally demanding multi-physics calculations to create a more accurate motor model to generate reference signals for the estimation methods to be evaluated against. Motor-CAD is a dedicated electrical motor design software that combines electromagnetic, thermal, and mechanical design modules. The software uses 2D transient and magneto-static finite element analysis (FEA) solvers in conjunction with thermal analysis using computational fluid dynamics (CFD), FEA, and empirical correlations. Figure 2.4 illustrates a 3D motor model appearance in Motor-CAD. It is also possible to see the salient PM rotor design with non-uniform airgaps and consequently also reluctance along the rotor. The Motor-CAD software [ANSYS Inc, 2019] was also used to generate motor maps to analyze motor behavior for different dynamic drive cycles.

Dynamic Drive Cycles

Examples of drive cycles used for evaluation of the designed state estimator are WLTC (Worldwide harmonized Light-duty vehicles Test Cycles) and NEDC (New European Driving Cycle), which are standardized drive cycles for motor emissions-level test evaluations. The dynamic test cycles' profile can be specified as vehicle speed as a function of time [DieselNet, 2019]. To get corresponding motor torque and rotor speed data for a given motor and cycle, a simple vehicle model with a

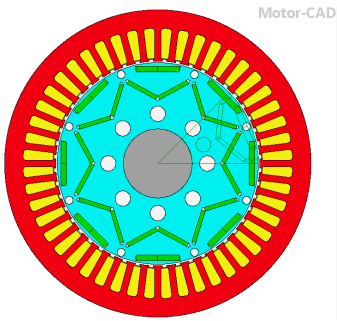

Figure 2.4: A cross-section view of the motor in Motor-CAD, with the motor axis pointing out of the page. The stator windings are represented by the outer yellow partitions. The rotor is represented by the inner circle with a blue hue. The permanent magnets in the rotor correspond to the green sections. From the image it is also possible to ascertain that the motor has 4 pole pairs.

vehicle-speed regulator was used to calculate the required torque for a given reference speed. The computed torque was then sent to a vehicle model with loss calculations to calculate the resulting vehicle speeds.

PMSM Simulink Model

The reference-signal generation from motor maps exported from Motor-CAD were done in Matlab Simulink and is illustrated in a block diagram representation of the Simulink model, shown in Figure 2.5. For a given dynamic cycle, reference torque and speed create reference currents I_d and I_q from Motor-CAD motor maps. An internal feedback control loop is then employed to produce the associated reference voltages. A coolant temperature is used as input to an exported lumped parameter thermal model (LPTM) from Motor-CAD. This consequently generates magnet temperature and flux linkages to get the final actuating currents and torque.

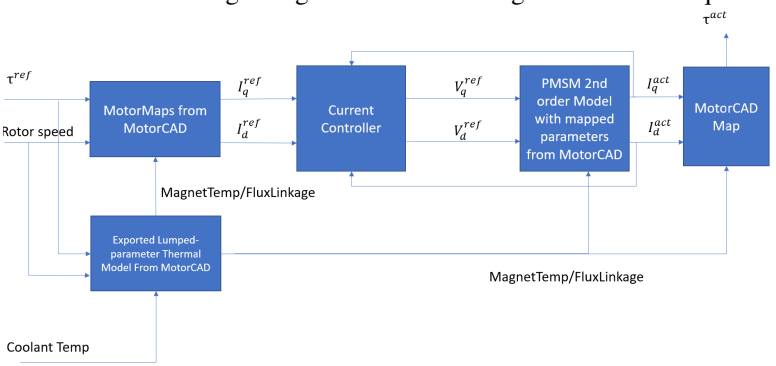

Figure 2.5: Motor-CAD block model structure in Matlab Simulink

3

State Estimation Theory

3.1 Model Discretization

When designing an observer for a larger embedded computer system, there are a lot of benefits in working with digital control systems. Two major attributes are their flexibility and cost efficiency. Discretizing the continuous-state form of the PMSM motor, derived in Section 2.3, can be done in many different ways. A common approach is to convert the process to a stroboscopic model, which shares the computers' sampled discrete-time sequence view of signals. Signals are often sampled with a hold circuit that holds the input signals to be piece-wise constant, i.e., a zero-order-hold transformation (ZOH). Applying the discrete piecewise-constant input signals to the continuous state-space system given in (3.1),

$$\begin{aligned} \dot{x} &= Ax_c + Bu_c \\ y &= Cx_c + Du_c \end{aligned} \tag{3.1}$$

transforms the description to the sampled data system shown in (3.2),

$$\begin{aligned} x[k+1] &= \Phi x[k] + \Gamma u[k] \\ y[k] &= Cx[k] + Du[k] \end{aligned} \tag{3.2}$$

where the state vector is given by x, the input by u and the output by y. The conversions of the dynamics with sample time h is given by:

$$\begin{aligned} \Phi &= e^{Ah} \\ \Gamma &= \int_0^h e^{As} ds B \end{aligned} \tag{3.3}$$

The discrete-time state dynamics can be computed in many different ways, here a numerical approach in Matlab was chosen using `expm()`. The simultaneous calculations of Φ and Γ matrices are given by [Wittenmark et al., 2016]:

$$\begin{bmatrix} \Phi & \Gamma \\ 0 & I \end{bmatrix} = \exp\left(\begin{bmatrix} A & B \\ 0 & 0 \end{bmatrix} h \right) \tag{3.4}$$

Another approach of approximating analog systems is by converting continuous differential equations to discrete difference equations. By approximating the differential operator with the forward Euler method, a substitution of operators is given by:

$$\frac{dx(t)}{dt} \approx \frac{x[k+1]-x[k]}{h} \tag{3.5}$$

The continuous system is then transformed into the resulting system:

$$\begin{aligned} x[k+1] &= (I+hA)x[k]+hBu[k] \\ y[k] &= Cx[k]+Du[k] \end{aligned} \tag{3.6}$$

An alternative approximation of the differential operator is with the backward Euler method. A substitution using:

$$\frac{dx(t)}{dt} \approx \frac{x[k]-x[k-1]}{h} \tag{3.7}$$

gives the resulting system after shifting forward one step, $x'[k] = x[k-h]$:

$$\begin{aligned} x'[k+1] &= (I-hA)^{-1}x'[k]+(I-hA)^{-1}hBu[k] \\ y[k] &= C(I-hA)^{-1}x'[k]+(C(I-hA)^{-1}hB+D)u[k] \end{aligned} \tag{3.8}$$

Euler's conversion schemes supposedly work well when the sampling frequency is fast relative to the control signal. A general rule of thumb for the choice of the sampling period is obtained with (3.9),

$$h\omega_c \approx 0.05-0.14 \tag{3.9}$$

where ω_c is the crossover frequency in radians per second of the continuous-time system. The interval gives a Nyquist frenquency that is about 23-70 times higher than the crossover frequency [Wittenmark et al., 2016].

3.2 Kalman Filter

With a model definition expanded with measurement noise e and process noise v in state-space form (3.10),

$$\begin{aligned} \dot{x} &= Ax + Bu + Nv \\ y &= Cx + Du + e \end{aligned} \tag{3.10}$$

we have the ability to reconstruct the state vector x from measured outputs y and input signal u as long as the system is observable. The noise covariance matrices are given by:

$$\begin{aligned} \text{cov}(v) &= \text{E}[vv^T] = Q \\ \text{cov}(e) &= \text{E}[ee^T] = R \end{aligned} \tag{3.11}$$

Further discussion on the observability of a system can be found Section 3.4. By using an observer, a model of the plant dynamics separately simulating the system, we can construct a state-estimate vector $\hat{x}$. Regulating the estimate in a feedback structure with the output estimation error, gives the complete observer:

$$\begin{aligned} \dot{\hat{x}} &= A\hat{x} + Bu + K(y - C\hat{x} - Du) \\ \hat{y} &= C\hat{x} + Du \end{aligned} \tag{3.12}$$

The estimation error can also be defined using the innovation term ε, named for how it relates to the innovation in the measurement signal, and it is defined by $\varepsilon = y - C\hat{x} - Du$.

The effect of the observer gain K can be seen more clearly by the state-estimation error dynamics, $\tilde{x} = x - \hat{x}$. Rearranging (3.12) into the state-estimation error dynamics gives

$$\dot{\tilde{x}} = (A - KC)\tilde{x} + Nv - Ke \tag{3.13}$$

Equation (3.13) illustrates the competing objectives of the observer gain K; the speed of minimizing the transient error determined by $A - KC$ versus balancing the sensitivity to measurement noise e. By taking the properties of the process noise v and the measurement noise e into account we can find the optimal observer gain K [Glad and Ljung, 2003]. The observer gain K is then derived from minimizing the expected error estimate variance. This leads to a stationary Riccati equation, with the stabilizing constraint that the estimation error $\tilde{x} \to 0$ over an infinite time horizon [Glad and Ljung, 2003]. The complication arises from the fact that the PMSM model derived Section 2.3, Equations (2.7), is a LPV system that varies with rotor speed ω. The LPV system allows for linear estimation techniques, but since the rotor speed is expected to vary during operation it also means that the state dynamics are time-varying and inhibit the use of the stationary solution.

The following chapters utilize the discrete-time state description, so the final results will also be presented as such. Previous equations are still applicable with a replacement of notation, differential $\dot{x}$ operators are changed to left shift operators x_{k+1}. Double time index $k|m$ is read as value at time k given measurements up to time m. The discrete-time observer description is then given as:

$$\begin{aligned}\hat{x}_{k+1|k} &= \Phi_k \hat{x}_{k|k-1} + \Gamma_k u_k + N_k v_k + K_k(y_k - C\hat{x}_{k|k-1} - Du_k) \\ \hat{y}_k &= C\hat{x}_{k|k-1} + D_k u_k + e_k\end{aligned} \tag{3.14}$$

The discrete-time estimation error goes to zero when the eigenvalues of the dynamics $\Phi_k - K_k C_k$ fall within the unit circle. To solve the compromise of minimizing the transient error and suppression of process and measurement noise, we once again refer to the state-estimation error:

$$\tilde{x}_{k+1|k} = (\Phi_k - K_k C_k)\tilde{x}_{k|k-1} + N_k v_k - K_k e_k \tag{3.15}$$

The recursive form of the estimation error covariance matrix is then given by:

$$\begin{aligned}P_{k+1|k} &= \text{cov}(\tilde{x}_{k+1|k}) = \text{cov}(x_{k+1} - \hat{x}_{k+1|k}) = \\ &(\Phi_k - \tilde{K}_k C_k)P_{k|k-1}(\Phi_k - \tilde{K}_k C_k)^T + N_k Q_k N_k^T + \tilde{K}_k R_k \tilde{K}_k^T\end{aligned} \tag{3.16}$$

$\tilde{K}$ is to denote the need to solve for an optimal observer gain. The complete derivation of the recursive form involves more steps, but is based on the substitution of $\hat{x}_{k+1|k}$ with (3.15). Then collecting the error vector and using the assumption that the stochastic variables, $\tilde{x}_k, v_k$, and e_k, are uncorrelated in order to separate the stochastic terms. Vector covariance properties then allow for the following substitution:

$$\begin{aligned}\text{cov}[(\Phi_k - \tilde{K}_k C_k)(x_k - \hat{x}_{k|k-1})] &= (\Phi_k - \tilde{K}_k C_k)\text{cov}(x_k - \hat{x}_{k|-1})(\Phi_k - \tilde{K}_k C_k)^T \\ &= (\Phi_k - \tilde{K}_k C_k)P_{k|k-1}(\Phi_k - \tilde{K}_k C_k)^T\end{aligned} \tag{3.17}$$

Completing the squares in Equation (3.16) and using compact notation results in the following definition for $P_{k+1|k}$:

$$\begin{aligned}P_{k+1|k} =&(\tilde{K} - \Phi P C^T(CPC^T + R)^{-1})(CPC^T + R)(\tilde{K} - \Phi P C^T(CPC^T + R)^{-1})^T \\ &+ \Phi P \Phi^T - \Phi P C^T(CPC^T + R)^{-1} CP\,\Phi^T + NQN^T\end{aligned} \tag{3.18}$$

In this form the choice of $\tilde{K}$ can be induced. With $\tilde{K}$ chosen to minimize the covariance matrix $P_{k+1|k}$ using (3.19),

$$\tilde{K}_k = \Phi_k P_{k|k-1} C_k^T (C_k P_{k|k-1} C_k^T + R_k)^{-1} \tag{3.19}$$

the minimal state prediction-error covariance becomes:

$$P_{k+1|k} = \Phi_k (P_{k|k-1} - P_{k|k-1} C_k^T (C_k P_{k|k-1} C_k^T + R_k)^{-1} C_k P_{k|k-1}) \Phi_k^T + N_k Q_k N_k^T \tag{3.20}$$

The resulting Kalman filter algorithmic structure can be found in Algorithm 1. It uses a description that includes the innovation term ε_k, with its covariance matrix S_k. The matrix I_k is a square identity matrix with dimensions matching the state-space system. The structure is employed to avoid repeating computations. The optimal observer gain K is affected by a large amount of process noise Q by putting a greater trust in the measurements and a large amount of measurement noise R by putting greater emphasis on the model. The Kalman filter is described to yield the best linear unbiased estimate, BLUE, and conditional expectation estimate [Gustafsson, 2012]. With the assumption of uncorrelated stochastic variables with Gaussian noise distribution, it is also the minimum variance, MV, and maximum likelihood, ML, estimate [Gustafsson, 2012].

Algorithm 1 Kalman filter [Gustafsson, 2012]

Initialize internal states: $\mathrm{E}(x_0) = \hat{x}_{1|0}$, $\mathrm{cov}(x_0) = P_{1|0}$
1: **repeat**
2: **function** <KALMAN FILTER>(u_k, y_k)
Measurement update
3: $\varepsilon_k = y_k - C_k \hat{x}_{k|k-1} - D_k u_k$
4: $S_k = C_k P_{k|k-1} C_k^T + R_k$
5: $K_k = P_{k|k-1} C_k^T S_k^{-1}$
6: $\hat{x}_{k|k} = \hat{x}_{k|k-1} + K_k \varepsilon_k$
7: $P_{k|k} = (I - K_k C_k) P_{k|k-1}$
Time Update
8: $\hat{x}_{k+1|k} = \Phi_k \hat{x}_{k|k} + \Gamma_k u_k$
9: $P_{k+1|k} = \Phi_k P_{k|k} \Phi_k^T + N_k Q_k N_k^T$
10: **return:** $\hat{x}_{k+1}$
11: **end function**
12: **until** Shutdown

3.3 Extended Kalman Filter

For non-linear models there exist many alternative variations for state-estimation filters. Unlike the linear case there is no optimal equivalent to the Kalman filter. The

states and outputs are not guaranteed to have Gaussian distributions even though the noise might be. Calculating the mean and covariance is not sufficient to describe the conditional probability distribution from previous measurements [Glad and Ljung, 2003]. A non-linear system description with the same uncorrelated noise assumptions and covariance matrices as in (3.11), is given by:

$$\begin{aligned} x_{k+1} &= f(x_k, u_k, v_k) \\ y_k &= h(x_k, u_k, e_k) \end{aligned} \tag{3.21}$$

with functions f and h. To find an observer gain K, we attempt to linearize the system around a working point. Related to the Taylor expansion, the standard extended Kalman filter linearizes around the current state estimate $\hat{x}$. Similar to the previous section, the standard EKF uses a discrete-time algebraic Riccati equation, DARE, for propagating the state vector covariance. The estimation-error covariance matrix P_k is instead updated using matrices of the partial derivates of the non-linear functions in (3.21):

$$F_k = \left. \frac{\partial f(x,u,0)}{\partial x} \right|_{\hat{x}_{k|k}, u_k} \tag{3.22}$$

$$H_k = \left. \frac{\partial h(x,u,0)}{\partial x} \right|_{\hat{x}_{k|k-1}, u_k} \tag{3.23}$$

F_k and H_k are intended to be symbolically defined Jacobian matrices, but numerical derivatives might be considered if the non-linear system is too computationally demanding or complex to differentiate. The standard EKF using only first-order compensation should work well when the degree of model non-linearity is small. There are, however, few guarantees regarding convergence for arbitrary set initial conditions. The complete algorithmic structure is shown in Algorithm 2. It can also be recognized that a linear state description will revert the standard EKF to a similar structure as found in the original Kalman filter [Gustafsson, 2012].

Algorithm 2 Extended Kalman filter [Gustafsson, 2012]

Initialize internal states: $\mathrm{E}(x_0) = \hat{x}_{1|0}$, $\mathrm{cov}(x_0) = P_{1|0}$
1: **repeat**
2: **function** <EXTENDED KALMAN FILTER>(u_k, y_k)
Measurement update
3: $\varepsilon_k = y_k - h(\hat{x}_{k|k-1}, u_k, 0)$
4: $S_k = H_k P_{k|k-1} H_k^T + R_k$
5: $K_k = P_{k|k-1} H_k^T S_k^{-1}$
6: $\hat{x}_{k|k} = \hat{x}_{k|k-1} + K_k \varepsilon_k$
7: $P_{k|k} = (I - K_k H_k) P_{k|k-1}$
Time Update
8: $\hat{x}_{k+1|k} = f(\hat{x}_{k|k}, u_k, 0)$
9: $P_{k+1|k} = F_k P_{k|k} F_k^T + Q_k$
10: **return:** $\hat{x}_{k+1}$
11: **end function**
12: **until** Shutdown

3.4 Observability

The observability of a system is an attribute of grave importance for the performance of estimators. It signifies the relation between the internal states and measured outputs. States that are unobservable span the kernel of the observability matrix $\mathcal{O}$, which for a continuous-time linear system is defined by:

$$\mathcal{O}(A,C) = \begin{bmatrix} C \\ CA \\ \vdots \\ CA^{n-1} \end{bmatrix} \tag{3.24}$$

The system is defined as observable when $\mathcal{O}$ has full rank. Full rank of the observability matrix $\mathcal{O}$ for the system $A \in \mathbb{R}^{n \times n}$ means that there are n linearly independent rows to recreate the full state vector through linear combinations of the measured output y [Glad and Ljung, 2003].

A test of the rank of the observability matrix $\mathcal{O}$ does, however, lead to very binary results. For improved insight of the degree of observability, we can instead analyze the eigenvector decomposition of the observability Gramian, $\mathcal{O}_x$. A definition of $\mathcal{O}_x$ can be derived from observing the energy of the output signal $y(t)$ [Glad and Ljung, 2003]. With no input signal and the initial state x_0, the output is then given by:

$$y(t) = Ce^{At}x_0 \tag{3.25}$$

A scalar measure of the output signals energy is then given by:

$$\int_0^\infty y^T(t)y(t) = x_0^T \int_0^\infty e^{A^T t} C^T C e^{At} dt x_0 = x_0^T \mathcal{O}_x x_0 \tag{3.26}$$

The Observability Gramian $\mathcal{O}_x$ can then be expressed as:

$$\mathcal{O}_x = \int_0^\infty e^{A^T t} C^T C e^{At} dt \tag{3.27}$$

An eigenvector decomposition of the observability Gramian $\mathcal{O}_x$ gives a measure of the relative observability of the different states. A way to present the results is by solving for the initial states x_0 that give the output magnitude $\|y\| = 1$ or:

$$x_0 \in \mathbb{R}^n; \quad x_0^T \mathcal{O}_x x_0 = 1 \tag{3.28}$$

The results were derived for continuous-time systems but are just as applicable for discrete-time systems [Glad and Ljung, 2003]. The observability analysis for the non-linear system is, however, a bit more obfuscated. The observability Gramian created using F_k and H_k are only relevant around the linearized points but will hopefully lead to some insight.

The condition number will also be employed in the observability analysis. The condition number of a matrix, $\kappa(A)$, is a measure of how close to singular the matrix A is. It is also used as a rough estimate for the arithmetic precision that may be required. The condition number defined with singular values, is given by [Holst and Ufnarovski, 2014]:

$$\kappa(A) = \frac{\sigma_1}{\sigma_r} \tag{3.29}$$

where σ_1 is the largest and σ_r is the smallest singular value for the matrix A.

4

Kalman Filter Design

4.1 Analysis of System Dynamics

To determine an appropriate Kalman filter sample time h, the system dynamics were analyzed. The system dynamics are in the form of the dq-model in Equation (2.7), with constant values for the inductances L_d, L_q and stator winding resistance R_s. The system is LPV with respect to the electrical angular speed ω_e, which increases proportionally to the rotor speed. Because the thesis almost exclusively deals with the electrical angular speed, the notation will be shortened to ω, and for the same reason the PM magnetic flux linkage λ_m will instead be referred to simply as λ. To visualize how the dynamics change, Figure 4.1 displays the eigenvalues of the continuous system, $A(\omega)$, in a root locus plot with varying electrical angular speed.

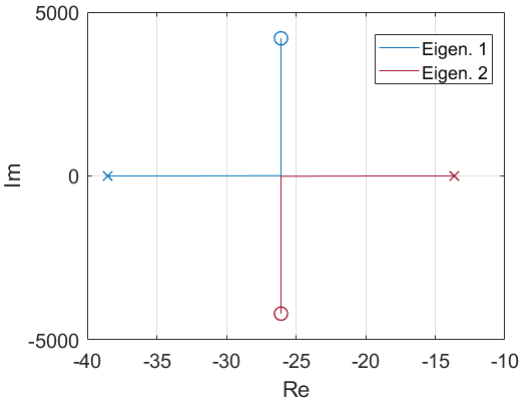

Figure 4.1: Eigenvalues for the continuous-time system $A(\omega)$, as $\omega : 0 \rightarrow 4200$ rad/s. The response shows that the oscillation frequency increases with increasing rotor speed, where the cross indicates the starting value 0 rad/s and the circle the end point 4200 rad/s.

The real parts of the eigenvalues remain constant when $\omega \geq 15$ rad/s, while the imaginary parts increase linearly with ω, which implies that the oscillation frequency of the system response increases proportionally with rotor speed. At the motor's maximum rotor speed, 10 000 rpm, the maximum electrical angular speed is ≈ 4200 rad/s and the complex eigenvalues of the continuous-time system is approximately $-26 \pm i4200$. The system has complex eigenvalues, which have a decaying sinusoidal response, $A_{amp}e^{-26t}\sin(4200t + \phi)$, where the amplitude A_{amp} and phase ϕ are determined by initial conditions [Massachusetts Institute of Technology, n.d.] The quickest system dynamics occur when the rotor is spinning at maximum velocity and the highest oscillation frequency is around 668 Hz. For reassurance of this observation, step-responses of the system dynamics at different ω are given in Figure 4.2.

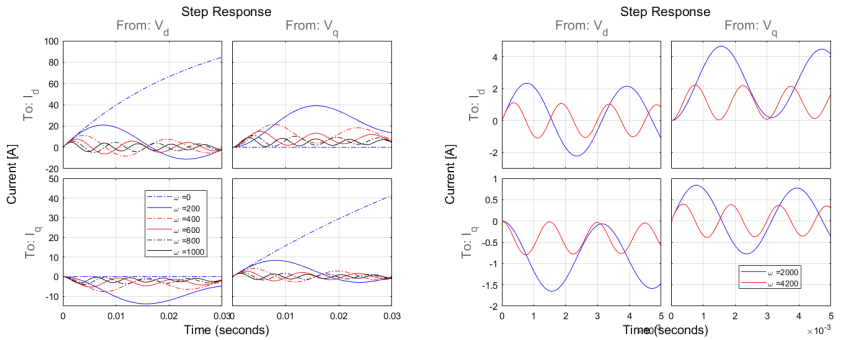

Figure 4.2: Step-responses of the continuous-time system matrix $A(\omega)$ for increasing ω, from inputs V_d and V_q to outputs I_d and I_q. The figure shows how the system's eigenfrequency, gain and coupling interactions changes for different ω.

From the step-responses, it is also possible to observe how the oscillation frequency of the response increases with increasing ω. The step-responses also reaffirm an oscillation frequency of ≈ 668 Hz at the motor's maximum rotor speed. To sufficiently capture the fastest system dynamics, a sample rate of $f_s > 2 \cdot 668$ Hz is required to avoid aliasing [Wittenmark et al., 2016].

A different approach to finding an appropriate sampling frequency is by utilizing the crossover frequency ω_c, when the open-loop system response has unity gain. The rule of thumb for choosing the sample time when approximating analog controllers was shown in Equation (3.9). At maximum rotor speed, the crossover frequency is $\omega_c \approx 7870$ rad/s which gives a recommended sampling interval of $f \approx 56\,\text{kHz} - 0.15\,\text{MHz}$. The sampling rate of the Kalman filter will be further evaluated in the simulation study, with considerations of the expected embedded hardware clock-frequency limitations. To evaluate if the recommended sampling frequency from the crossover frequency ω_c is imperative for the observer design,

Bode plots comparing if the frequency characteristics of the discrete-time system are sufficiently close to the continuous-time system are given in Figure 4.3. The discrete-time system is discretized with ZOH with sampling frequencies 1 kHz and 2 kHz. The figures show that with sampling frequency 1 kHz, the lower frequency characteristics are mostly accurate except for the phase characteristics for $V_d \rightarrow I_d$ and $V_q \rightarrow I_q$. With sampling frequency 2 kHz, the frequency characteristics are mostly accurate up to around 1 kHz. With the assumption that the current and voltage frequencies will not exceed 1 kHz, a sampling frequency of 2 kHz ought to suffice.

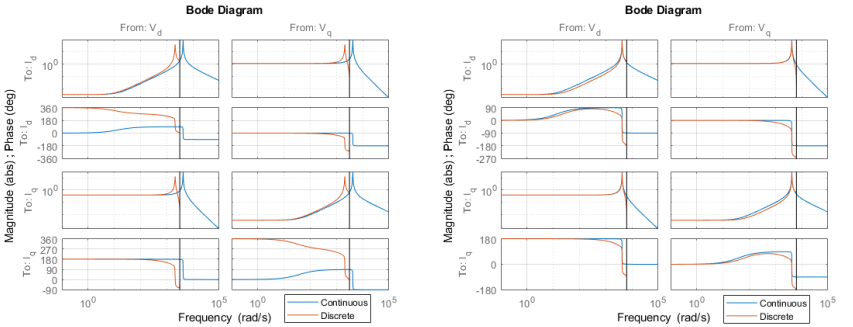

(a) Sampling frequency 1 kHz.

(b) Sampling frequency 2 kHz.

Figure 4.3: Bode plot of the continuous-time and discrete-time systems, comparing frequency characteristics. The discrete-time systems were sampled at 1 kHz in (a) and 2 kHz in (b).

4.2 Design of PMSM Kalman Filter

A few different variations of the Kalman filter design were analyzed in this thesis. To be able to estimate the flux linkage λ, the system description found in (2.7) from Section 2.3, is expanded with 0 flux linkage dynamics. The most basic design is with a $\mathbb{R}^{3\times3}$ system dynamics matrix, with the state vector augmented to include a λ estimate and it is described by the relations:

$$\begin{aligned} \dot{x} &= Ax + Bu \\ y &= Cx \end{aligned} \tag{4.1}$$

$$A = \begin{bmatrix} -\frac{R_s}{L_d} & \frac{\omega L_d}{L_q} & 0 \\ -\frac{\omega L_d}{L_q} & -\frac{R_s}{L_q} & -\frac{\omega}{L_q} \\ 0 & 0 & 0 \end{bmatrix} \quad B = \begin{bmatrix} \frac{1}{L_d} & 0 \\ 0 & \frac{1}{L_q} \\ 0 & 0 \end{bmatrix} \quad C = \begin{bmatrix} 1 & 0 & 0 \\ 0 & 1 & 0 \end{bmatrix} \tag{4.2}$$

with the internal states x, input u and measured output y:

$$x = [I_d, I_q, \lambda]^T \quad u = [V_d, V_q]^T \quad y = [I_d, I_q]^T \tag{4.3}$$

The system in (4.1) – (4.3) will eventually be augmented to include slow flux linkage time dynamics in Section 4.4 to allow for an observability analysis, which requires an asymptotically stable system. Later on in the Sections 4.8, an expanded KF design that includes the coolant temperature as a state will also be introduced.

Constant-valued inductances and stator winding resistance were used to conduct a parameter-sensitivity analysis. The matrix A, that describes the system in (4.2) is, however, forced to be recreated every sample period to account for the varying parameter ω. Incorporating updated parameter information can be done in conjunction with the change in rotor speed if the remaining time-varying parameters can be efficiently updated. A performance comparison utilizing lookup tables, LUTs, for inductances and temperature compensation for the stator winding resistance can be found in the simulation study.

The P_0 matrix was initialized as Q, which means that the initial variance of the state error is given as the process noise. With no particular information on how the process noise enters the system, it is simply chosen as three uncorrelated stochastic disturbances on the states. The process error dynamics N_k is therefore chosen as the identity matrix. The term $N_k Q_k N_k^T$ in the time update of $P_{k|k-1}$ in Algorithm 1, line 9, simplifies into Q. Without added noise in the reference signal generation, the exact calibration of the process and measurement noise covariance matrices Q and R, are not directly apparent during estimation simulations. With the assumption of uncorrelated stochastic disturbances on the states and measured outputs, Q and R are chosen as:

$$Q = \begin{bmatrix} \sigma_{x_1}^2 & 0 & 0 \\ 0 & \sigma_{x_2}^2 & 0 \\ 0 & 0 & \sigma_{x_3}^2 \end{bmatrix} \quad R = \begin{bmatrix} \sigma_{y_1}^2 & 0 \\ 0 & \sigma_{y_2}^2 \end{bmatrix} \tag{4.4}$$

with σ referring to the standard deviation of the respective signals. The initialization of the state vector $\hat{x}_0$ is chosen to match startup values. With currents at zero and a λ_c that corresponds to motor coolant temperature, the initial values are:

$$\hat{x}_0 = [0, 0, \lambda_c]^T \tag{4.5}$$

4.3 Kalman-Gain Analysis

This section presents a preliminary analysis of how the observer gain K as well as the error covariance matrix P behave as a function of the electrical angular speed,

$K(\omega)$ and $P(\omega)$. The dimensions of the observer gain matrix are $K \in \mathbb{R}^{n\times m}$, where n is the number of states and m is the number of measured outputs and the error covariance matrix has the same dimensions as the system A matrix, $P \in \mathbb{R}^{n\times n}$.

Figures 4.4 – 4.6 display the values of $K(\omega)$ and the diagonal of $P(\omega)$, the state estimation error variance $\text{var}(\tilde{x})$, as a function of ω after 50 iterations of Algorithm 1. Through testing it was deemed that the rate of change of the estimation error covariance matrix P was small after 50 iterations of the KF algorithm. The model of the third order state-space system is described in Section 4.2, discretized with ZOH. The chosen Kalman filter sample rates effect how the error-variance oscillates. At standstill, the flux linkage uncertainty increases and the observer gain increases as compensation, with the opposite effect for the current estimation. The greatest change in result occurs from 1 kHz to 2 kHz, when the sampling frequency $f_s > 2 \cdot 668$ Hz.

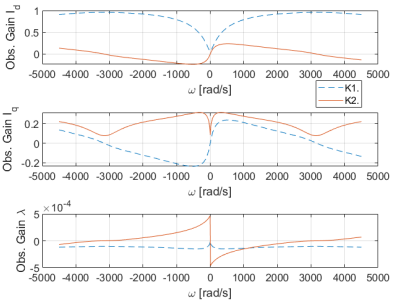

(a) $K(\omega)$ as a function of ω.

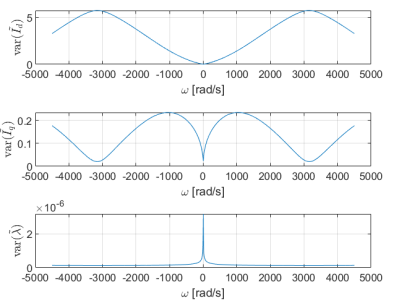

(b) $P(\omega)$ diagonal, as a function of ω.

Figure 4.4: $K(\omega)$ and $P(\omega)$ of the discrete-time system, converted with ZOH with the sampling frequency 1 kHz. The observer gains K_1 and K_2 correspond to the their respective measured states in y, or I_d and I_q.

Figure 4.7 displays the effect of increasing the magnitude of the noise covariance matrices Q and R, respectively, with a gain of 1000. The effect of increasing the process noise Q results in observer gains $K(\omega)$ that to a large extent rely on their respective current measurements for the current estimation and a minimal and slow compensation of the flux linkage with an observer gain close to zero at medium and higher speeds. Increasing the measurement noise R, increases the reliance on the model and the observer gains for the currents' estimation decrease in turn. Unlike all other designs, the I_d measurement has a more prominent influence than I_q on the flux linkage estimation result with the configuration that increases the magnitude of R.

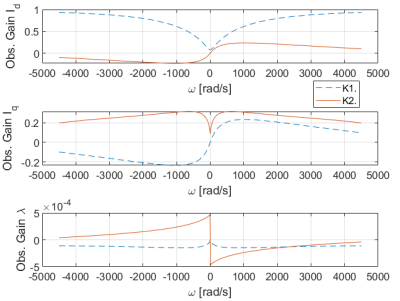

(a) $K(\omega)$ as a function of ω.

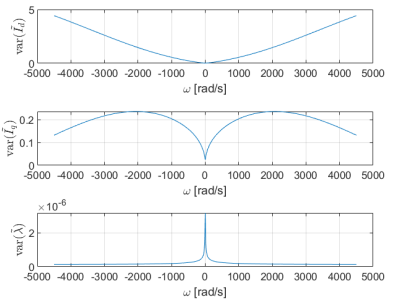

(b) $P(\omega)$ diagonal, as a function of ω.

Figure 4.5: $K(\omega)$ and $P(\omega)$ of the discrete-time system, converted with ZOH with the sampling frequency 2 kHz.

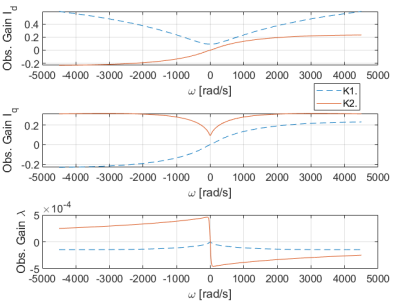

(a) $K(\omega)$ as a function of ω.

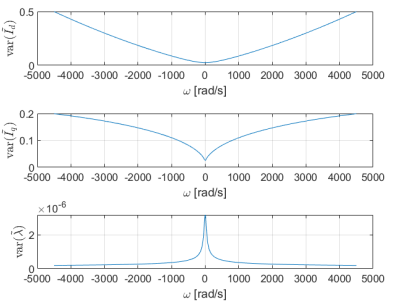

(b) $P(\omega)$ diagonal, as a function of ω.

Figure 4.6: $K(\omega)$ and $P(\omega)$ of the discrete-time system, converted with ZOH with the sampling frequency 10 kHz.

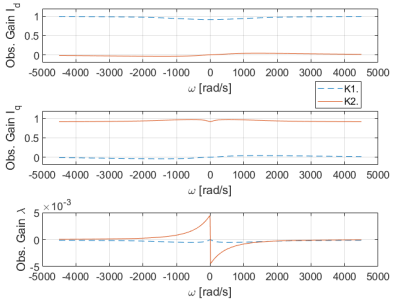

(a) $K(\omega)$ as a function of ω.

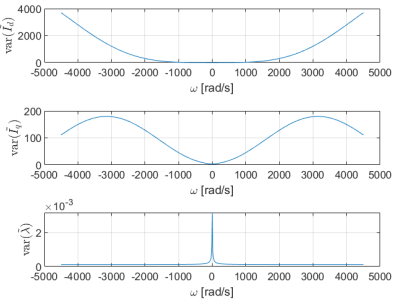

(b) $P(\omega)$ diagonal, as a function of ω.

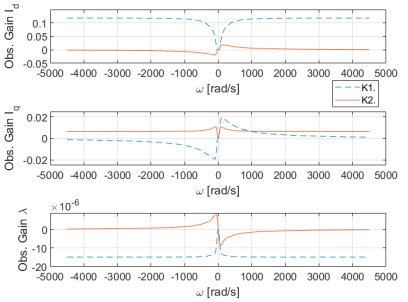

(c) $K(\omega)$ as a function of ω.

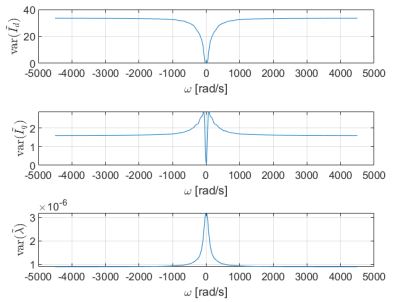

(d) $P(\omega)$ diagonal, as a function of ω.

Figure 4.7: $K(\omega)$ and $P(\omega)$ of the discrete-time system, converted with ZOH with the sampling frequency 2 kHz. The top row are the results from Q multiplied with a factor of 10^3 and the bottom row is the same factor instead multiplied with R.

4.4 Slow Flux Linkage Dynamics

Because of the poor flux linkage observability at low rotor speeds, an electrical angular speed threshold, $\omega_{threshold}$, was introduced to determine when the standard Kalman filter was active. To more accurately asses the value of $\omega_{threshold}$, an observability analysis of the observability Gramian $\mathcal{O}_x$ can be conducted. The system does, however, need to be stable to be able to generate the observability Gramian. By introducing a slow flux linkage dynamic, that minimally alters the behavior of the KF, $\mathcal{O}_x$ can be generated and analyzed. The PM temperature time-constant value is $\tau_m = 1800$ s, which is obtained from observing a step response of a PM rotor temperature change using the lumped parameter model from Motor-CAD. The dynamics can be written:

$$\dot{\lambda} = -\frac{1}{\tau_m}\lambda \tag{4.6}$$

A comparison of the observer gain $K(\omega)$ and error covariance matrix $P(\omega)$ was done with different sample times and the results are shown in Figures 4.8 and 4.9. The percentage error is defined by:

$$\%Error = \frac{Slow - Ref}{|Ref|} \cdot 100 \tag{4.7}$$

with the reference value Ref being $K(\omega)$ or $P(\omega)$ with zero flux linkage dynamics and $Slow$ the corresponding quantity with slow flux linkage dynamics. From Figures 4.8 – 4.9 we can observe only a negligible difference, most pronounced when the observer gain crosses zero, which occurs at $\omega \approx 3000$ rad/s when the sampling rate is 1 kHz and at standstill when the sampling rate is 2 kHz. The ω value when the observer gain crosses zero can be seen for the different sampling rates in Figures 4.4 – 4.5.

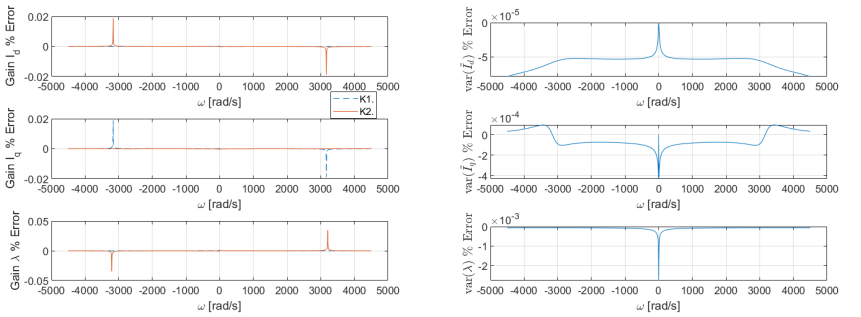

(a) Percentage deviation of $K(\omega)$ between slow and zero λ dynamics.

(b) Percentage deviation of $P(\omega)$ between slow and zero λ dynamics.

Figure 4.8: Percentage deviation of $K(\omega)$ and $P(\omega)$ with slow and zero λ dynamics, with sampling frequency 1 kHz.

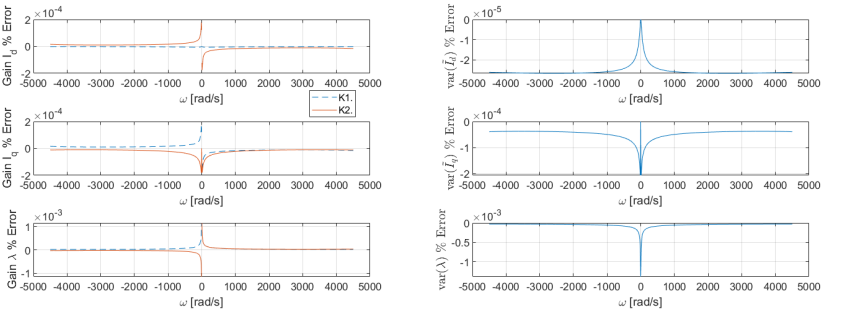

(a) Percentage deviation of $K(\omega)$ between slow and zero λ dynamics.

(b) Percentage deviation of $P(\omega)$ between slow and zero λ dynamics.

Figure 4.9: Percentage deviation of $K(\omega)$ and $P(\omega)$ with slow and zero λ dynamics, with sampling frequency 2 kHz.

4.5 Observability Gramian

With the introduction of slow flux linkage time dynamics that only alter the behavior of the filter minimally, the system dynamics are stable and we are able to generate the observability Gramian $\mathcal{O}_x$. By observing how the observability of λ changes for different ω, we can find an initial estimate for $\omega_{threshold}$ that can be further evaluated during simulations.

An eigenvector decomposition of $\mathcal{O}_x$ does not always lead to near linearly independent state compositions. For the system dynamics utilized in the standard KF they are, however, closely associated with the original states. A 3D representation

of the eigenvector directions of $\mathcal{O}_x$ is shown in Figure 4.10. From the figure, it is possible to observe the close relation between the eigenvectors and the associated original states. The eigenvectors associated to the currents also have a negative orientation for $\omega \geq 50$.

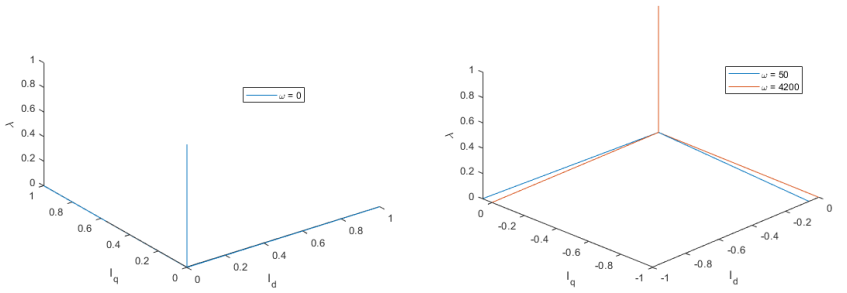

(a) (b)

Figure 4.10: Eigenvectors of $\mathcal{O}_x$ for the third order continuous-time system in (4.2) – (4.3) modified with slow flux linkage dynamics (4.6), with electrical angular speed 0 rad/s in (a) and 50 and 4200 rad/s in (b).

The eigenvalues of $\mathcal{O}_x$ are shown in Figure 4.11. From the figure, we can observe a big jump in magnitude of the eigenvalue for λ that levels off after $\omega \approx 250$ rad/s. The magnitude difference of the eigenvalues is quite large and is approximately at worst case a difference of 10^{12}. This difference is potentially exacerbated by how different physical variables are numerically quantified for different SI units.

The observability is poor at low rotational speeds and near standstill because the back-EMF is small during these conditions and as a result the connection between the flux linkage and the currents is weak. The weak connection essentially inhibits the ability to estimate the flux linkage from the currents.

To improve the visibility of the results, a table of the required input-signal magnitudes for a resulting output norm equal to 1 is presented in Table 4.1. The set of states x, that have an output norm $\|y\| = 1$, is given by the ellipsoid $\{x \in \mathbb{R}^n;\ x^T \mathcal{O}_x x = 1\}$ [Stanford University, 2001]. The Table 4.1 and Figure 4.11 show that unlike the other signals, I_d observability worsens slightly with increased rotor speed and that the observability has mostly converged at $\omega \approx 500$ rad/s.

Because of the large difference in the magnitude of the eigenvalues, we can also expect that the condition number $\kappa(\mathcal{O}_x(\omega))$ is large as well, which is shown in Figure 4.12. This is also a possible motivation for normalizing the system dynamics to improve the numerical stability of the system. The condition number is generated both from a Matlab routine as well as the singular value definition in (3.29) for reassurance.

An observability analysis of the ZOH discretized system was also conducted

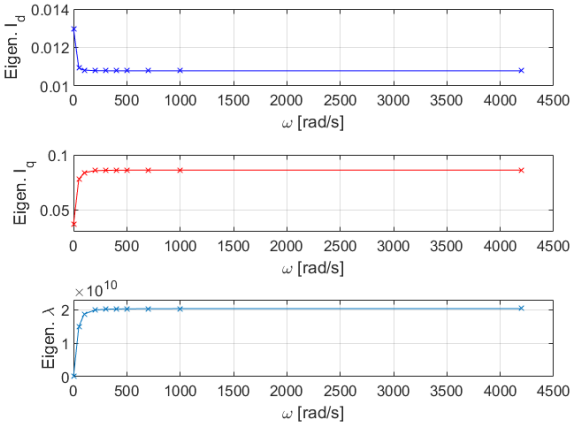

Figure 4.11: Eigenvalues of $\mathscr{O}_x(\omega)$ of the third-order continuous-time system in (4.2) – (4.3) modified with slow flux linkage dynamics (4.6) as a function of ω.

Table 4.1

State magnitudes $\{x \in \mathbb{R}^n;\ x^T \mathscr{O}_x(\omega)x = 1\}$			
ω [rad/s]	$\lvert I_d \rvert$ [A]	$\lvert I_q \rvert$ [A]	$\lvert \lambda \rvert$ [Wb-turns]
50	9.46	3.59	$8.18 \cdot 10^{-6}$
500	9.62	3.41	$7.02 \cdot 10^{-6}$
4200	9.63	3.40	$7.00 \cdot 10^{-6}$

with sampling frequencies 1 kHz and 2 kHz. The discrete-time system with sampling frequency 2 kHz had a similar eigenvector decomposition of $\mathscr{O}_x$ as the continuous-time system. With sampling frequency 1 kHz, however, the eigenvectors associated with the currents become positively oriented once again when $\omega \geq 3200$ rad/s. This change occurred at around the same ω that the state estimation error variance changes, seen in Figure 4.4. Figure 4.13 displays the eigenvalues of the observability Gramian $\mathscr{O}_x(\omega)$ and Figure 4.14 is a plot of the condition number $\kappa(\mathscr{O}_x(\omega))$ calculated from a Matlab routine for the discrete-time systems. The figure with eigenvalues show that using a 2 kHz sampling frequency gives slightly larger eigenvalue magnitudes and the condition number is also slightly smaller except for when the motor is at maximum velocity, $\omega = 4200$ rad/s. The eigenvalue magnitude proportions of the discrete-time system is relatively similar to the continuous-time system, but altered in such a way that it drastically reduces the condition number.

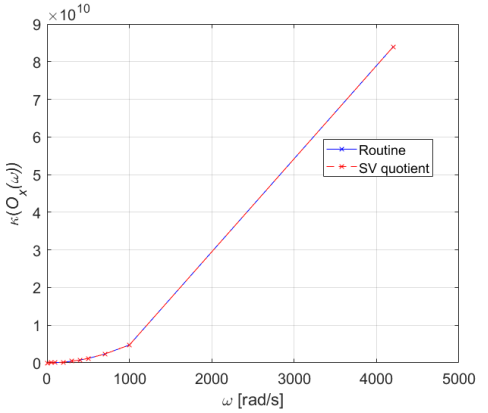

Figure 4.12: The condition number $\kappa(\mathscr{O}_x(\omega))$ of the third-order continuous-time system in (4.2) – (4.3) modified with slow flux linkage dynamics (4.6) as a function of ω, using both a Matlab routine and the singular value definition.

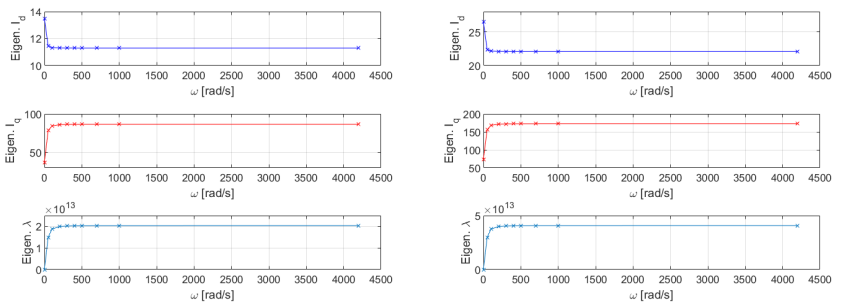

(a) Eigenvalues of $\mathscr{O}_x(\omega)$ at sampling frequency 1 kHz.

(b) Eigenvalues of $\mathscr{O}_x(\omega)$ at sampling frequency 2 kHz.

Figure 4.13: Eigenvalues of the observability Gramian of the third-order system (4.2) – (4.3) modified with slow flux linkage dynamics (4.6) and ZOH discretized, as a function of ω.

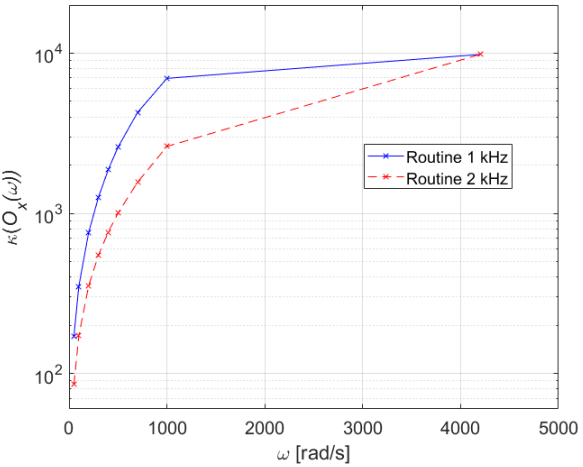

Figure 4.14: The condition number $\kappa(\mathcal{O}_x(\omega))$ of the third-order (4.2) – (4.3) modified with slow flux linkage dynamics (4.6) and ZOH discretized with sampling frequencies 1 kHz and 2 kHz. The condition number was calculated using a Matlab routine and the y-axis is defined in logarithmic scale.

4.6 Noise Transfer Function Gain

The effect measurement and process noise have on the flux linkage estimation result was analyzed for different rotor speeds. A Bode magnitude plot of the transfer function of the measurement noise e to the estimation error $\tilde{\lambda}$ is given in Figure 4.15 and correspondingly for the process noise v to $\tilde{\lambda}$ in Figure 4.16. The noise transfer functions were derived from the plant model:

$$\begin{aligned} x[k+1] &= \Phi x[k] + \Gamma u[k] + v[k] \\ y[k] &= Cx[k] + e[k] \end{aligned} \tag{4.8}$$

and the observer model:

$$\begin{aligned} \hat{x}[k+1] &= \Phi \hat{x}[k] + \Gamma u[k] + K(y[k] - C\hat{x}[k]) \\ \hat{y}[k] &= C\hat{x}[k] \end{aligned} \tag{4.9}$$

where the resulting dynamics of the estimation error $\tilde{x} = x - \hat{x}$ can be described as:

$$\begin{aligned} \tilde{x}[k+1] &= \Phi x[k] + \Gamma u[k] + v[k] - \Phi \hat{x}[k] - \Gamma u[k] - K(Cx[k] + e[k] - C\hat{x}[k]) \\ &= (\Phi - KC)\tilde{x}[k] + v[k] - Ke[k] \end{aligned} \tag{4.10}$$

which gives the process noise to estimation error transfer function $H_v(z)$:

$$H_v(z) = (zI - (\Phi - KC))^{-1} \tag{4.11}$$

and the measurement noise to estimation error transfer function $H_e(z)$:

$$H_e(z) = -(zI - (\Phi - KC))^{-1}K \tag{4.12}$$

The transfer functions vary with ω, which affects the system dynamics matrix Φ, as well as observer gain K, which in turn are both affected by the noise covariance matrices Q and R and the number of iterations. The calibration of the noise covariance matrices are described in greater detail in Section 5.6. Figures 4.15 and 4.16 both include the results on the observer gain K_k after 1 and 50 iterations of the time-varying KF algorithm on the state estimation-error covariance matrix P_k. The model is of the discrete-time dynamic coolant temperature system with sampling frequency 2 kHz. The dynamic coolant temperature KF has an expanded state vector which includes the coolant temperature and is described in further detail in Section 4.8.

From the figures, it is possible to observe that the measurement noise is strongly attenuated and that for both transfer functions, the differences in gain characteristics

for different ω are reduced after multiple KF algorithm iterations. It is also possible to observe a strong sensitivity to flux linkage process noise during low rotor speeds, when the flux linkage observer gain increases. At these low rotor speeds when $\omega = 10$ rad/s, the dynamic coolant temperature KF will, however, switch to a low-observability estimator (see Section 4.7) and avoid the increase in process-noise sensitivity.

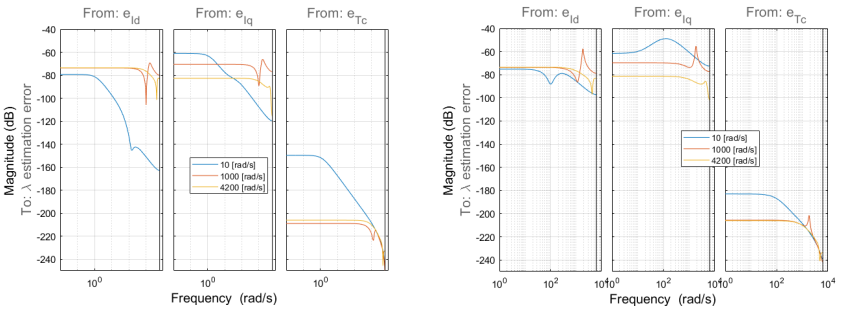

(a) After 1 iteration of observer gain K. (b) After 50 iterations of observer gain K.

Figure 4.15: Bode magnitude plot of the transfer function for measurement noise e to λ estimation error for varying ω.

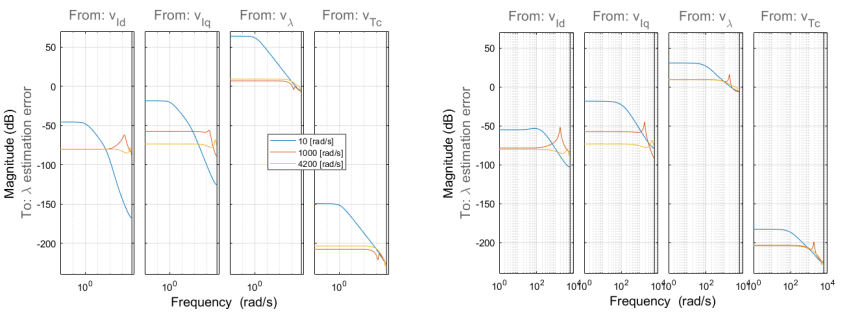

(a) After 1 iteration of observer gain K. (b) After 50 iterations of observer gain K.

Figure 4.16: Bode magnitude plot of the transfer function for process noise v to λ estimation error for varying ω.

4.7 Description and Motivation for Low-speed Mode with Switching

Based on the related research on PM rotor temperature estimation from the back-EMF [Wallscheid et al., 2017], the observability of the flux linkage is found to be low during operating ranges near standstill, which the results in Section 4.5 also confirm. This leads to an observer gain for λ that spikes when $\omega = 0$. Inspired by [Wallscheid et al., 2017], a PM rotor temperature estimation scheme that switches for rotor speeds under a specified $\omega_{threshold}$ is presented. An algorithm design was tested that keeps the original system dimensions. Because the rotor thermal stress is generally lower during low rotor speeds, when $\omega \leq \omega_{threshold}$, the low-speed estimator does not use the model to update the state estimation and λ is instead estimated using (2.10) from Section 2.4, from a PM rotor temperature estimation that exponentially decays to the coolant temperature. When the KF is active the rotor temperature T_r is instead calculated outside the algorithm with (2.10) using the KF state estimation output. The torque is also always calculated outside the algorithm using (2.9) from Section 2.3. A more thorough analysis for finding an appropriate $\omega_{threshold}$ was conducted in Section 4.5. The switching algorithm was based on the standard Kalman filter with a ZOH discretization using the sample time h, and is presented in Algorithm 3, where T_{c_k} is the coolant temperature at sample k and $\hat{T}_{r_k}$ is the latest PM temperature estimate. The PM temperature estimate decays with a time-constant $\tau_m = 1800$ s.

Algorithm 3 Direct coolant temperature KF with low speed estimator switch

Initialize internal states: $\mathrm{E}(x_0) = \hat{x}_{1|0}$, $P_{1|0} = Q$
repeat
  function <KALMAN FILTER>$(u_k, y_k, \omega_k, T_{c_k}, \hat{T}_{r_{k-1}})$
    if $|\omega_k| \geq \omega_{threshold}$ **then**
      ZOH discretization
      $Block = expm([A_k, B_k; zeros(2,5)] \cdot h)$
      $\Phi_k = Block(1:3, 1:3)$
      $\Gamma_k = Block(1:3, 4:5)$
      Measurement update
      $\varepsilon_k = y_k - C_k \hat{x}_{k|k-1}$
      $S_k = C_k P_{k|k-1} C_k^T + R_k$
      $K_k = P_{k|k-1} C_k^T S_k^{-1}$
      $\hat{x}_{k|k} = \hat{x}_{k|k-1} + K_k \varepsilon_k$
      $P_{k|k} = (I_k - K_k C_k) P_{k|k-1}$
      Time update
      $\hat{x}_{k+1|k} = \Phi_k \hat{x}_{k|k} + \Gamma_k u_k$
      $P_{k+1|k} = \Phi_k P_{k|k} \Phi_k^T + Q_k$
    else
      Low-speed estimator
      $\hat{T}_{r_k} = T_{c_k} + (\hat{T}_{r_{k-1}} - T_{c_k}) e^{-\frac{h}{\tau_m}}$
      $\lambda_k = \lambda_0 (1 + B_r (\hat{T}_{r_k} - T_0))$
      $\hat{x}_{k+1} = [y_k, \lambda_k]^T$
    end if
    return: $\hat{x}_{k+1}$
  end function
until Shutdown

4.8 Expanded System with Coolant Temperature

A Kalman filter design that more generally takes advantage of the coolant temperature signal measurement, was also developed to include the coolant temperature T_c as a state. The system description is also based on the idea of updating the flux linkage below $\omega_{threshold}$, when it is under low thermal stress, with the coolant temperature. Applying the equation for temperature to flux linkage conversion (2.10), to drive the flux linkage estimation towards its corresponding value at the coolant temperature λ_c, gives the relation:

$$\lambda_c = \lambda_{m0}(1 + B_r(T_c - T_0)) \tag{4.13}$$

By grouping the constant terms and using it as the input signal, the input signal λ_0^0 is then described by:

$$\lambda_0^0 = \lambda_{m0}(1 - B_r \cdot T_0) \tag{4.14}$$

where λ_0^0 is the equivalent of the flux linkage estimation at 0 °C. The well parameterized reference point λ_{m0} was acquired from a LUT that uses both the rotor speed and torque to generate an output and this is the same parameter used for determining the current PM temperature estimate T_{r_k} using (2.10). The final $\mathbb{R}^{4\times4}$ system matrix was obtained after the inclusion of slow PM time dynamics τ_m, to circumvent the previous problem of generating the observability Gramian $\mathscr{O}_x$. The dynamic coolant temperature system has T_c as a state with dynamics and a measurement signal but this should not greatly affect the results in comparison to the direct coolant temperature system because the measurement noise and model disturbance for T_c are assumed to be low. The coolant temperature does, however, affect the flux linkage estimation even when $\omega > \omega_{threshold}$, which could have a non-negligible bias towards the coolant temperature even at higher rotor speeds. Considering that the time constant τ_m is long, it should, however, only be a minor difference to the direct coolant temperature observer. The expanded state-space model is described with the following matrices and state, input and output vectors:

$$A = \begin{bmatrix} -\frac{R_s}{L_d} & \frac{\omega L_d}{L_d} & 0 & 0 \\ -\frac{\omega L_d}{L_q} & -\frac{R_s}{L_q} & -\frac{\omega}{L_q} & 0 \\ 0 & 0 & -\frac{1}{\tau_m} & \frac{\lambda_{m0} B_r}{\tau_m} \\ 0 & 0 & 0 & -\frac{1}{\tau_m} \end{bmatrix} \quad B = \begin{bmatrix} \frac{1}{L_d} & 0 & 0 \\ 0 & \frac{1}{L_q} & 0 \\ 0 & 0 & \frac{1}{\tau_m} \\ 0 & 0 & 0 \end{bmatrix} \quad C = \begin{bmatrix} 1 & 0 & 0 & 0 \\ 0 & 1 & 0 & 0 \\ 0 & 0 & 0 & 1 \end{bmatrix} \tag{4.15}$$

$$x = [I_d, I_q, \lambda, T_c]^T \quad y = [I_d, I_q, T_c]^T \quad u = [V_d, V_q, \lambda_0^0]^T \tag{4.16}$$

The process and measurement noise covariance matrices Q and R were expanded to $\mathbb{R}^{4\times4}$ and $\mathbb{R}^{3\times3}$, respectively, with the modelled covariance of coolant temperature T_c to be relatively constant and the signal variance subsequently chosen to be relatively low. The final algorithm description for the expanded KF with coolant temperature is shown in Algorithm 4. The expanded KF also utilizes $\omega_{threshold}$ and will at low operating speeds stop updating the estimation error covariance matrix and update the flux linkage estimation solely with the system model, unlike the direct coolant temperature KF, which utilizes an initial λ value based on the rotor temperature estimation from when the system states were easier to observe. The dynamic coolant temperature KF had difficulties with λ estimation during strong deceleration below the observability speed threshold. A torque threshold $\tau_{threshold}$ and $\omega_{threshold}$ combination was instead used to switch to the low-speed estimator. As a result of the torque being able to vary widely when the observer has low observability, the parameter λ_{m0} also has the ability to vary widely because of the change in operating point for the LUT, while the low-speed λ estimator only changes slowly. To improve the accuracy of the PM temperature estimation, the parameter value λ_{m0} in (4.15) was kept from before the switch to the low-speed estimator.

Algorithm 4 Dynamic coolant temperature KF with low speed estimator switch

Initialize internal states: $\mathrm{E}(x_0) = \hat{x}_{1|0}$, $P_{1|0} = Q$
repeat
  function <KALMAN FILTER>$(u_k, y_k, \omega_k, \tau_k)$
    ZOH discretization
    $Block = expm([A_k, B_k; zeros(3,7)] \cdot h)$;
    $\Phi_k = Block(1:4, 1:4)$;
    $\Gamma_k = Block(1:4, 5:7)$;
    if $|\omega_k| \geq \omega_{threshold}$ AND $\tau_k \geq \tau_{threshold}$ **then**
      Measurement update
      $\varepsilon_k = y_k - C_k \hat{x}_{k|k-1}$
      $S_k = C_k P_{k|k-1} C_k^T + R_k$
      $K_k = P_{k|k-1} C_k^T S_k^{-1}$
      $\hat{x}_{k|k} = \hat{x}_{k|k-1} + K_k \varepsilon_k$
      $P_{k|k} = (I_k - K_k C_k) P_{k|k-1}$
      Time update
      $\hat{x}_{k+1|k} = \Phi_k \hat{x}_{k|k} + \Gamma_k u_k$
      $P_{k+1|k} = \Phi_k P_{k|k} \Phi_k^T + Q_k$
    else
      Low-speed estimator
      $\varepsilon_k = y_k - C_k \hat{x}_{k|k-1}$
      $S_k = C_k P_{k|k-1} C_k^T + R_k$
      $K_k = P_{k|k-1} C_k^T S_k^{-1}$
      $K_k(3,:) = 0$
      $\hat{x}_{k|k} = \hat{x}_{k-1|k-1} + K_k \varepsilon_k$
      $\hat{x}_{k+1|k} = \Phi_k \hat{x}_{k|k} + \Gamma_k u_k$
    end if
    return: $\hat{x}_{k+1}$
  end function
until Shutdown

4.9 Normalized System Dynamics

The analysis of the observability Gramian gave an early intuition of possible numerical computation uncertainties. To attempt to alleviate some of the numerical concerns that might arise from the different signal units, a normalized system description found in [Glad and Ljung, 2003] was implemented. In an effort to improve the condition number $\kappa(\mathscr{O}_x(\omega))$, we can normalize the signals and limit their operating range to the interval $|x_i| \leq 1$. The normalized signals x_n, y_n and u_n are transformed to their original signal values by applying diagonal matrices composed of the largest operational signal magnitudes across the diagonal, where the largest signal magnitudes were found in simulations with the greatest operating dynamics:

$$x = D_x x_n \quad y = D_y y_n \quad u = D_u u_n \tag{4.17}$$

The state-space matrices were then converted to normalized equivalents with the diagonal matrices as:

$$A_n = D_x^{-1} A D_x \quad B_n = D_x^{-1} B D_u \quad C_n = D_y^{-1} C D_x \tag{4.18}$$

The eigenvalues of the observability Gramian of the continuous $\mathbb{R}^{4\times4}$ system as a function of ω are shown in Figure 4.17, for both the standard and normalized system. A comparison of the condition number $\kappa(\mathscr{O}_x(\omega))$ between the standard and normalized system is shown in Figure 4.18. The magnitude difference of the eigenvalues is smaller after normalizing the system, with the most pronounced change in eigenvalue corresponding to λ, resulting in a reduction of the maximum condition number $\kappa(\mathscr{O}_x(\omega))$ by an order of $\approx 10^4$. The dynamic coolant temperature system has an observability Gramian eigenvector decomposition that still is nearly linearly independent and closely associated with the original states, but unlike the direct coolant temperature system it also has a parameter that is dependent on the torque. An estimate of λ_{m0} is obtained for every ω using reasonable values for the rotor speed and torque combinations.

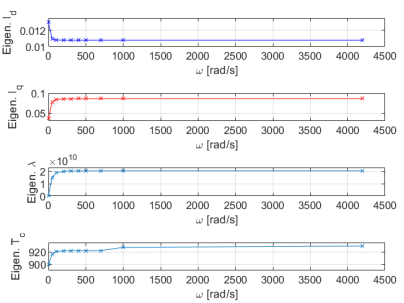

(a) Eigenvalues of $\mathscr{O}_x(\omega)$.

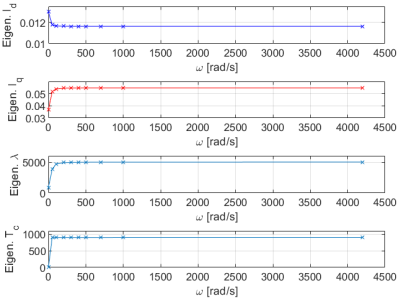

(b) Eigenvalues of $\mathscr{O}_x(\omega)$ of the normalized system.

Figure 4.17: Eigenvalues of the observability Gramian of the fourth-order continuous-time standard and normalized system as a function of ω.

A comparison of the standard and normalized discrete-time systems is also given, with the eigenvalues of the observability Gramian displayed in Figure 4.19 and condition number in Figure 4.20, using a sampling frequency of 1 kHz. Figures 4.21 and 4.22 display the eigenvalues and condition numbers of the discretized system with sampling frequency 2 kHz. Discretizing the dynamic coolant temperature system lowers the condition number significantly compared to the

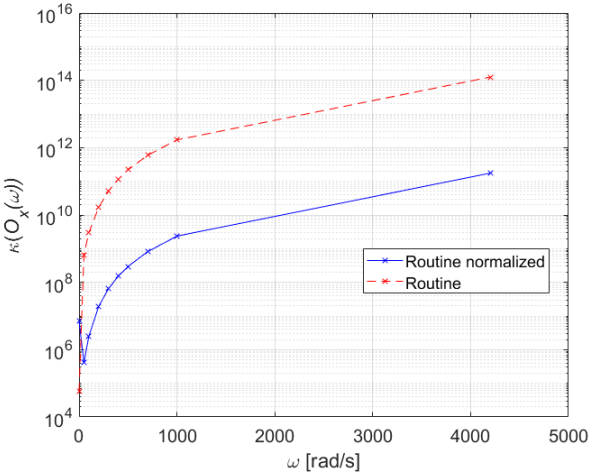

Figure 4.18: Condition number $\kappa(\mathcal{O}_x(\omega))$ of the standard and normalized continuous-time fourth-order systems as a function of ω. The condition number was calculated using the Matlab routine `cond()` and the y-axis is in logarithmic scale.

continuous-time system. After normalizing the system, the biggest change in eigenvalue magnitude was once again for λ and unlike its continuous-time counterpart, the condition number also decreased with increased rotor speed. The system with 2 kHz sampling frequency also had slightly higher eigenvalues, improved observability, with only a minor increase in the condition number.

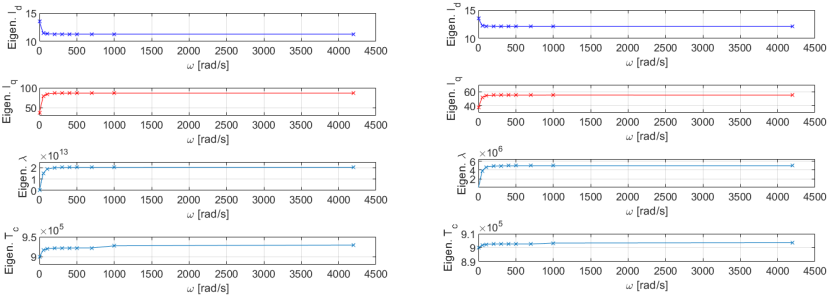

(a) Eigenvalues of $\mathscr{O}_x(\omega)$.

(b) Eigenvalues of $\mathscr{O}_x(\omega)$ of the normalized system.

Figure 4.19: Eigenvalues of the observability Gramian of the fourth-order discrete-time system as a function of ω, with sampling frequency 1 kHz.

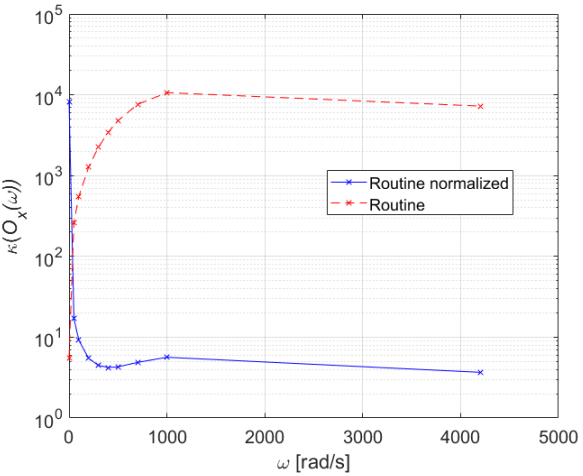

Figure 4.20: Condition number $\kappa(\mathscr{O}_x(\omega))$ of the standard and normalized observability Gramian of the fourth-order discrete-time system as a function of ω, with sampling frequency 1 kHz. The condition number was calculated using the Matlab routine `cond()` and the y-axis is in logarithmic scale.

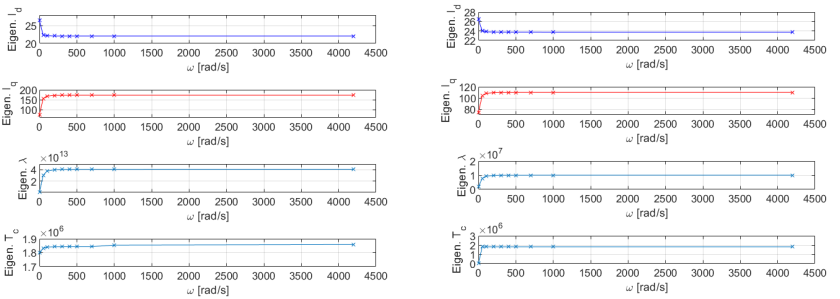

(a) Eigenvalues of $\mathcal{O}_x(\omega)$.

(b) Eigenvalues of $\mathcal{O}_x(\omega)$ of the normalized system.

Figure 4.21: Eigenvalues of the observability Gramian of the fourth-order discrete-time system as a function of ω, with sampling frequency 2 kHz.

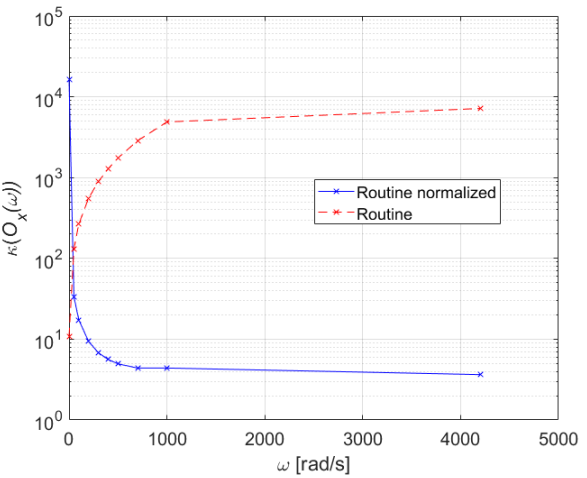

Figure 4.22: Condition number $\kappa(\mathcal{O}_x(\omega))$ of the standard and normalized observability Gramian of the fourth-order discrete-time system as a function of ω, with sampling frequency 2 kHz. The condition number was calculated using the Matlab routine `cond()` and the y-axis is in logarithmic scale.

4.10 Kalman Filter Simulation Environment

The Kalman filters were implemented in Matlab Simulink to simulate the sensorless PMSM estimation schemes. The input signals for the system are reference signals generated from Motor-CAD simulations. The KF model was initialized with noise covariance matrices and parameters for the system dynamics. The stator winding resistance R_s was a constant value, defined at a well parameterized reference temperature. The initialization also included the requisite parameters for the equations to compensate the stator winding resistance with the stator temperature T_s (2.11) and calculating the torque and rotor temperature from the flux linkage estimation. The inductances L_d and L_q were both defined as LUTs that matched the inductance with a specific rotor speed and torque combination as well as constant values based on the average of the LUT. Figure 4.23 shows a depiction of the inductance LUTs.

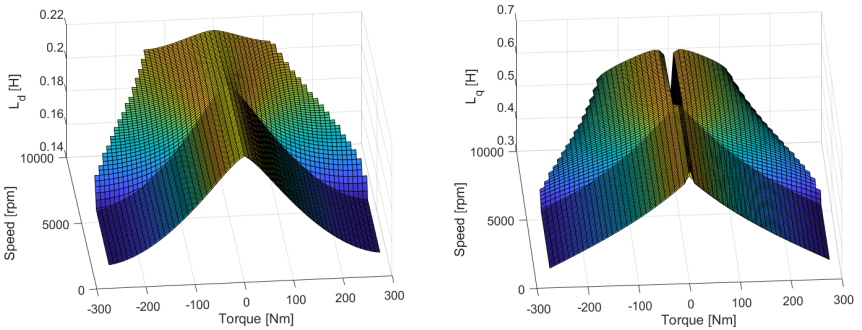

(a) L_d LUT representation.

(b) L_q LUT representation.

Figure 4.23: A depiction of the L_d and L_q LUT, respectively, which gives an inductance value in units of mH from a given torque and rotor speed combination.

The Kalman filters executed at sampling-time intervals h. The current flux linkage estimation $\hat{\lambda}_k$ from the Kalman filter was used to estimate both the torque and PM rotor temperature from Equations (2.9) and (2.10). The rotor temperature was calculated by reordering Equation (2.10) to instead calculate the rotor temperature for a given flux linkage value. The flux linkage to rotor temperature conversion was very sensitive because of the divisions with both the reference point λ_{m0} and the remanent induction temperature coefficient B_r, which both are small numbers. A change in flux linkage of ≈ 1 mWb-turns corresponds to a temperature change of $\approx 15^{\circ}$C.

The Simulink model also included a number of first-order low-pass (LP) filters. The Kalman filter itself possessed the capability to filter out noise from the input signal if calibrated correctly but additional LP-filters have been added to separately tune the estimations of the different signals. The transfer function of the continuous-time representation of the LP-filter with unit filter gain is described by:

$$H(s) = \frac{1}{\tau_{LP}s + 1} \tag{4.19}$$

where τ_{LP} is the filter time constant which is inversely proportional to the cut-off frequency. The overarching goal was to estimate the PM rotor temperature change, which occurs on a significantly longer time frame, and introducing minor time delays from LP-filters with shorter time constants can be reasonably motivated. An LP-filter was applied to the rotor temperature estimation. The PM rotor temperature was calculated from flux linkage reference points λ_{m0} that were obtained from a LUT at a given torque and rotor speed combination. The time constant for the LP-filter used in rotor temperature estimation was instead chosen to smooth out the change in working points λ_{m0}. An additional LP-filter was placed on the input actuation torque from the Motor-CAD reference signal. The current regulator can cause noise in the actuation torque reference-signal generation during noisy test cycles and high speed, low torque steady-state operations. The torque LP-filter time constant was chosen to be relatively fast and was used to avoid changes in LUT tables and low-speed estimator switches because of noise. A block model representation of the Simulink KF implementation is shown in Figure 4.24.

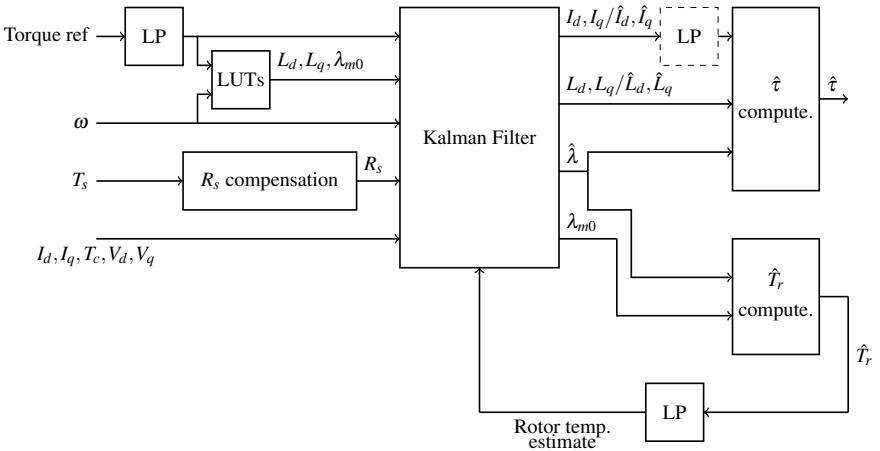

Figure 4.24: Block model of the Simulink KF implementation. The dashed LP-filter for the current input signals for the $\hat{\tau}$ computation is not always active. There are also variations of the design that use either reference or estimated input currents for the $\hat{\tau}$ computation block. The EKF model uses estimated inductances instead of the LUT results to calculate the torque. Only the direct-T_c KF uses the T_r estimate, during the low-speed estimator.

5

Kalman Filter Simulation Study

5.1 Motor-CAD Reference Signals and Motor Model

The simulation study contains the results and analysis of the KF observer designs and was run with reference signals, generated from Motor-CAD simulations using two dynamic cycles, NEDC and WLTC. The test cycles are standardized vehicle drive cycles that were used in conjunction with the generated Motor-CAD reference signals for Kalman filter evaluation. The test cycles are illustrated in Figures 5.1 and 5.2, which show how the electrical angular speed and torque evolve in time. A NEDC test cycle is shown in Figure 5.1 and a WLTC cycle in Figure 5.2. To evaluate the different low-speed estimators and observe the cooling process, a test cycle containing a substantial warm-up which then transitioned to a steep decline in speed was created. A modified WLTC cycle with more aggressive dynamics and a long cooldown period was used for that purpose.

In Table 5.1 a few relevant characteristics of the motor used in the simulation study is also presented.

Table 5.1: A few key characteristics of the Nissan Leaf motor used in the simulation study, which are presented in following table.

Nissan Leaf motor characteristics.	
Maximum torque [Nm]	270
Maximum rotor speed [rpm]	10 000
Average LUT L_d [H]	$2.165 \cdot 10^{-4}$
Average LUT L_q [H]	$6.5 \cdot 10^{-4}$
R_s at 25 °C [Ω]	$8.1 \cdot 10^{-3}$
Coolant water temperature [°C]	60

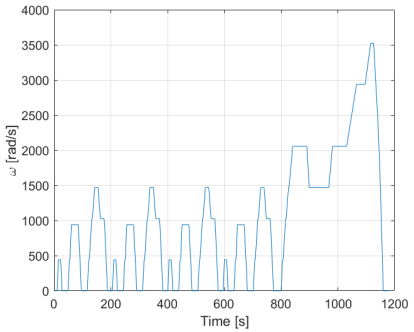

(a) NEDC electrical angular speed ω.

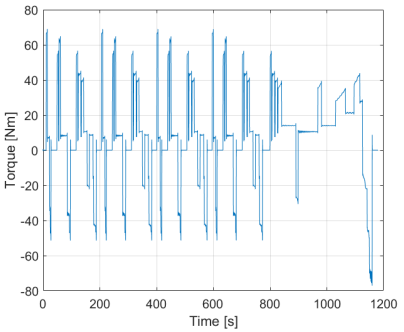

(b) NEDC torque.

Figure 5.1: NEDC cycle with ω and torque over time.

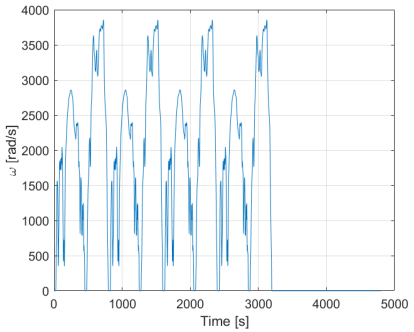

(a) WLTC electrical angular speed ω.

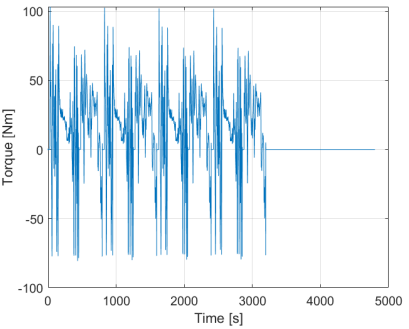

(b) WLTC torque.

Figure 5.2: Electrical angular speed ω and torque over time for the high-speed WLTC cycle with cooldown period.

5.2 Comparison with Updated Parameters

The parameters that describe the system dynamics can vary widely during operation. To determine the significance of the parameter variations, a comparison between simulations with constant parameters R_s, L_d and L_q and working-point dependent inductances from LUTs and stator-winding resistance with stator temperature compensation was done. The flux linkage estimation is shown in Figure 5.3a and the rotor temperature estimation in Figure 5.3b for the direct coolant temperature KF. A comparison between torque estimations was excluded because of the difficulty to meaningfully ascertain differences from an estimation plot. The large flux linkage estimation spikes occur when ω is low, which can be explained by the low observability. Estimating the rotor temperature from the flux linkage is very sensi-

tive to errors, resulting in large PM temperature estimation errors. Figure 5.3b does, however, show a large improvement when utilizing LUT inductances. The impact of stator winding temperature compensation was low in comparison, but its effect increased during operations that heated the stator considerably.

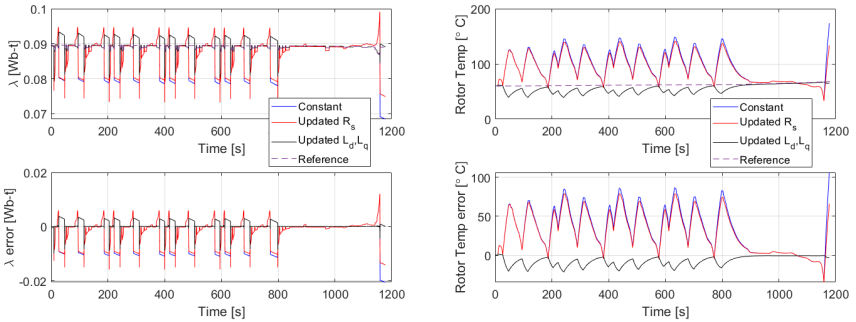

(a) Flux linkage λ estimation.

(b) Rotor temperature T_r estimation.

Figure 5.3: Results for λ and T_r estimation with NEDC cycle and error with constant model parameters, updated R_s and working-point dependent inductances. The reference signals were temperature and flux linkage generated by the Motor-CAD model. A drastic improvement in the λ and T_r estimation was obtained by correcting for the inductance variations. The tests were done using the direct-T_c KF.

5.3 Comparison with Low-speed Estimator

Low-speed Switch

To illustrate the effects of the low-speed estimator, Figure 5.4 shows the flux linkage estimation, Figure 5.5, shows the rotor temperature estimation and Figure 5.6, shows the torque estimation with and without the low-speed estimator for the direct coolant temperature KF. The low-speed estimator $\omega_{threshold}$ was chosen to be 500 rad/s in the comparisons. Figure 5.4 shows a large improvement in the λ estimation with the alternative estimation method, avoiding the use of the flux linkage observer gain when it spikes during the low-observability mode. The major improvement in λ estimation also results in a similar improvement in rotor temperature T_r estimation, but not the torque estimation.

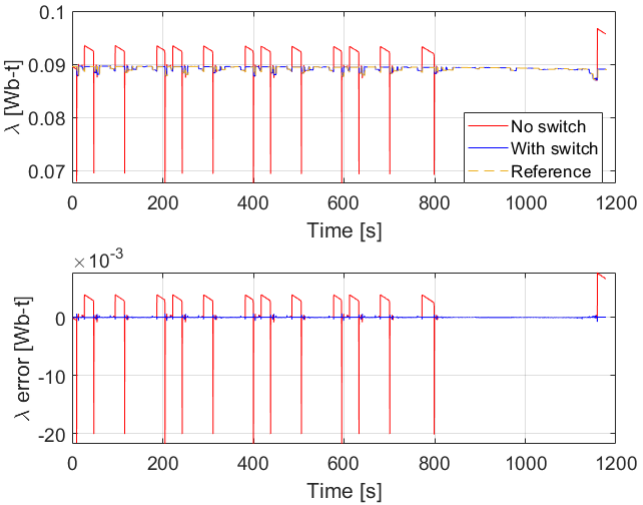

Figure 5.4: Flux linkage estimation and error comparison, with and without low-speed estimator switch. Using a low-speed estimator drastically improves the flux linkage estimation. The $\omega_{threshold}$ was chosen to be 500 rad/s using the direct-T_c KF.

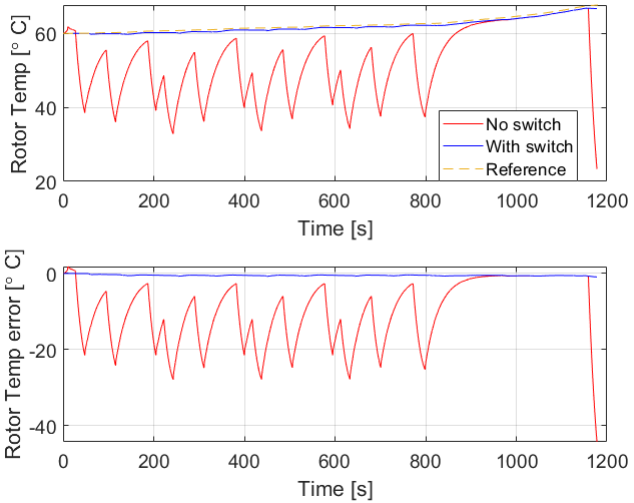

Figure 5.5: Rotor temperature estimation and error comparison, with and without low speed estimator switch. The $\omega_{threshold}$ was chosen to be 500 rad/s using the direct-T_c KF.

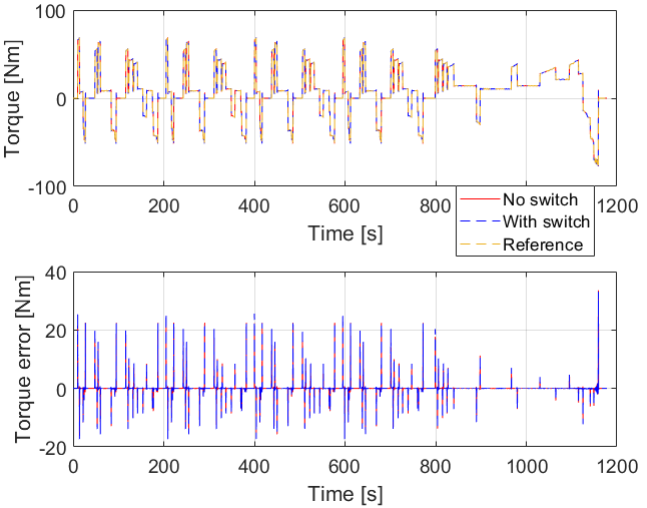

Figure 5.6: Torque estimation and error comparison, with and without low-speed estimator switch. The improvement in the flux linkage estimation does not greatly impact the torque estimation results. The $\omega_{threshold}$ was chosen to be 500 rad/s using the direct-T_c KF.

Electrical Angular Frequency Threshold

Different $\omega_{threshold}$ were tested to find what value worked best during simulations. A comparison of the rotor temperature estimation with different threshold values can be seen in Figure 5.7. A table with L_1-norm averages of the respective estimation errors is given in Table 5.2 and correspondingly for the standard deviation in Table 5.3. From Table 5.3, it is possible to observe that the error-signal variation increases with increasing $\omega_{threshold}$, but with only minor changes from 500 to 600 rad/s. In Table 5.2, the best choice of $\omega_{threshold}$ that minimized the estimation errors varied depending on which of the outputs that were prioritized. Because the purpose of estimating the flux linkage is to estimate the rotor temperature and torque, $\omega_{threshold}$ should be chosen accordingly. The design that minimized the rotor temperature estimation error used a threshold value of 600 rad/s. It should also be noted that increasing the threshold, decreased the time the KF was active and the low-observability sensitivity must be weighed against the KF inactivity time.

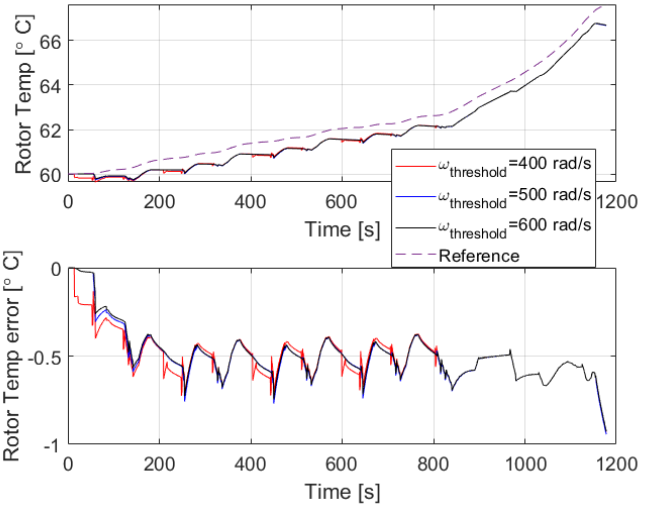

Figure 5.7: Comparison of different $\omega_{threshold}$ for rotor temperature estimation and error. Minor T_r estimation improvements can be seen by increasing the threshold slightly. Test were done using the direct-T_c KF.

Table 5.2: A $\omega_{threshold}$ at 600 rad/s was found to minimize the T_r estimation error, whereas a $\omega_{threshold}$ at 400 rad/s minimized λ and τ estimation errors.

L_1-norm average error for different $\omega_{threshold}$			
$\omega_{threshold}$ [rad/s]	$\|\tilde{\lambda}\|_1$ average [µWb-turns]	$\|\tilde{T}_r\|_1$ average [°C]	$\|\tilde{\tau}\|_1$ average [Nm]
400	31.67	0.5040	0.4439
500	34.98	0.4921	0.4458
600	34.83	0.4869	0.4460

Table 5.3: The standard deviation of the estimation error increased with increasing $\omega_{threshold}$, but levelled out at around 500 rad/s.

Standard deviation of error for different $\omega_{threshold}$			
$\omega_{threshold}$ [rad/s]	σ_λ of error [µWb-turns]	σ_{T_r} of error [°C]	σ_τ of error [Nm]
400	65.95	0.1217	1.957
500	81.51	0.1432	1.966
600	81.45	0.1433	1.966

5.4 Comparison with Coolant Temperature State Augmentation

Parameter Tuning

To be able to start the evaluation process, a few of the KF design parameters were first calibrated through simulation studies. A collection of L_1-norm error averages for the flux linkage, rotor temperature and torque estimation using varying $\omega_{threshold}$ and $\tau_{threshold}$ combinations is shown in Table 5.4. The dynamic coolant temperature KF had difficulty estimating the flux linkage when decelerating to under the observability speed threshold. The flux linkage fluctuations caused by changes in torque can not be correctly estimated during low observability, resulting in rotor temperature estimation spikes. The table shows that a $\tau_{threshold} = -20$ Nm with $\omega_{threshold} = 600$ rad/s yields the best rotor temperature estimation but considering all three estimation errors, the best results were given with $\tau_{threshold} = -20$ Nm and $\omega_{threshold} = 500$ rad/s.

Table 5.4: The best overall estimation results were given using the $\omega_{threshold} = 500$ rad/s and $\tau_{threshold} = -20$ Nm combinations for the dynamic-T_c KF.

L_1-norm error average with varying $\omega_{threshold}$ and $\tau_{threshold}$ combinations.				
$\omega_{threshold}$ [rad/s]	$\tau_{threshold}$ [Nm]	$\|\tilde{\lambda}\|_1$ average [μWb-turns]	$\|\tilde{T}_r\|_1$ average [°C]	$\|\tilde{\tau}\|_1$ average [Nm]
400	-20	188.17	0.9551	0.5042
400	-10	228.62	1.1020	0.5111
500	-20	176.59	0.6878	0.5035
500	-10	216.63	0.8169	0.5101
600	-20	185.79	0.6873	0.5061
600	-10	226.73	0.8197	0.5131
700	-20	195.32	0.6888	0.5104
700	-10	237.19	0.8245	0.5179

The KF low-speed cool-down characteristics were calibrated by reducing the PM temperature time constant τ_m. Although the tests used slightly shorter time constants τ_m, it was still slow enough to expect the same negligible difference in observer gain and estimation error covariance when comparing the slow flux linkage dynamic system with zero flux linkage dynamics. In Figure 5.8, the dynamic coolant temperature KF flux linkage and rotor temperature estimation error for varying PM temperature time constants during the cool-down period are shown. Their respective L_1-norm average errors are shown in Table 5.5. During the cool-down period, the torque was 0 and was therefore excluded for the τ_m calibration tests. From the simulation tests, it appeared that the best estimation results are given for $\tau_m = 1500$ s. To determine how the faster PM time constant performed during sporadic activation of the low-speed estimator, Table 5.6 shows the L_1-norm average estimation error for the NEDC test cycle. The table shows only a minor degradation of the estimation, indicating the new time constant may be a worthy trade-off for the improved estimation during cool down.

Table 5.5: Lowering the PM temperature time constant τ_m slightly to 1500 s improved the low-speed estimator simulations results during the cool-down period.

L_1-norm average error for different τ_m		
τ_m [s]	$\|\tilde{\lambda}\|_1$ average [µWb-turns]	$\|\tilde{T}_r\|_1$ average [°C]
1800	97.74	1.2704
1700	79.38	1.0003
1600	66.41	0.7868
1500	66.31	0.7261
1400	94.87	1.0515

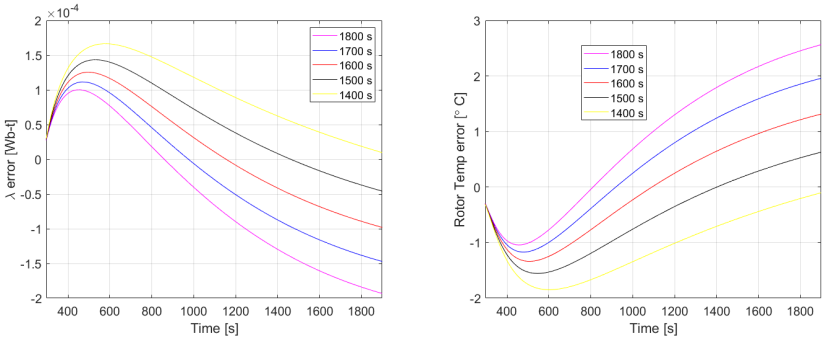

(a) Flux linkage estimation error.

(b) Rotor temperature estimation error.

Figure 5.8: Flux linkage and rotor temperature estimation errors for varying PM temperature time constants τ_m. The estimation was evaluated for the cool-down period of the motor, after a 300 second lead-in sequence with the KF active.

Table 5.6: Lowering the PM temperature time constant τ_m did lead to a minor degradation of the estimation error when the motor is more active, but can be a worthy trade-off for the improvement during extensive cool down periods.

L_1-norm average error for different τ_m, NEDC cycle			
τ_m [s]	$\|\tilde{\lambda}\|_1$ average [µWb-turns]	$\|\tilde{T}_r\|_1$ average [°C]	$\|\tilde{\tau}\|_1$ average [Nm]
1800	160.60	0.7265	0.4512
1500	160.72	0.7278	0.4512

Direct and Dynamic Coolant Temperature KF Comparison

A comparison between the direct and dynamic coolant temperature KF designs is found in Figure 5.9 and Table 5.7 using the modified high-speed WLTC test cycle with cool-down period. The flux linkage estimation was substantially better for the direct-T_c KF but that only resulted in a minor improvement in the torque estimation and a worse rotor temperature estimation. With more fine tuning, both KF designs can achieve very similar performances, however, the remaining analysis done in this

section was conducted with the dynamic-T_c design.

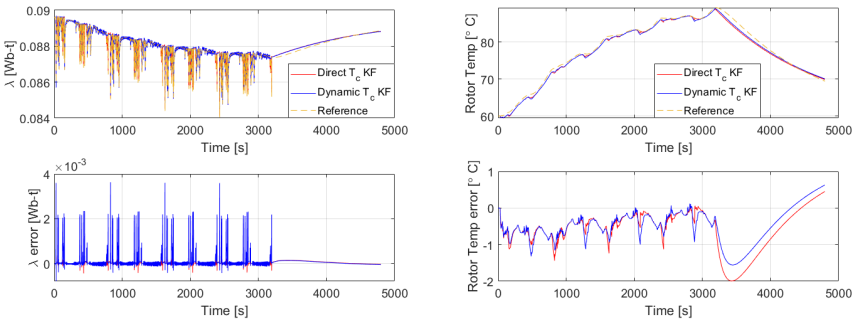

(a) Flux linkage estimation and error.

(b) Rotor temperature estimation and error.

Figure 5.9: Flux linkage and rotor temperature estimation performance for a high-speed WLTC test cycle with cool-down period, comparing the direct and dynamic coolant temperature KF design.

Table 5.7: The superior direct-T_c KF λ estimation only translates into a minor τ estimation improvement and a slightly worse T_r estimation compared to the dynamic-T_c KF design.

L_1-norm average error for different KF designs, WLTC high-speed cycle with cool-down period			
KF design	$\|\tilde{\lambda}\|_1$ average [μWb-turns]	$\|\tilde{T}_r\|_1$ average [°C]	$\|\tilde{\tau}\|_1$ average [Nm]
Direct-T_c KF	47.452	0.6144	0.4021
Dynamic-T_c KF	108.67	0.5497	0.4214

5.5 Torque Estimation

The maximum torque estimation error was fairly significant and was not improved with the refinement of the KF designs up to this point. The Motor-CAD current reference signals were used as input for both the KF and the torque estimation, but unlike the KF that can calibrate the noise covariance matrices Q and R to handle noisy input signals, the torque estimation was greatly affected by the high-frequency noise in the input current signals. The current signal estimation from the KF was, however, a LP-filtered version of the reference signal and a comparison between the reference and estimated current signal as input for the torque estimation can be found in Figure 5.10. In Figure 5.11, the torque estimation error using the estimated currents is compared to using LP-filtered reference currents that used the same time constant as the torque reference LP-filter. The torque reference signal

was used as an input to various LUTs and was LP-filtered to avoid potential issues that could occur from using a noisy input signal. The filtered reference currents were not used for the KF, which would require a recalibration of the measurement noise covariance matrix R to avoid the flux linkage estimation deteriorating. The current reference signals were LP-filtered with a time constant of 0.1 s and this yielded the best torque-estimation results. Further LP-time constant analysis can be found in Section 5.7.

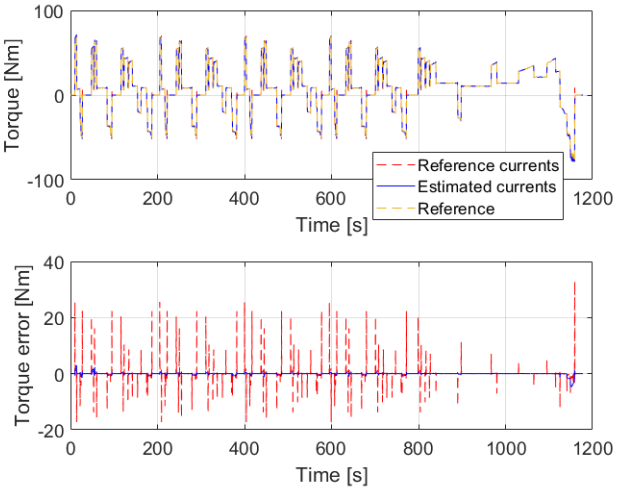

Figure 5.10: Torque estimation and error. Comparing the torque reference signal to the torque estimation using current reference signals and estimated currents from a NEDC test cycle. The torque estimation error was greatly reduced when using the estimated currents.

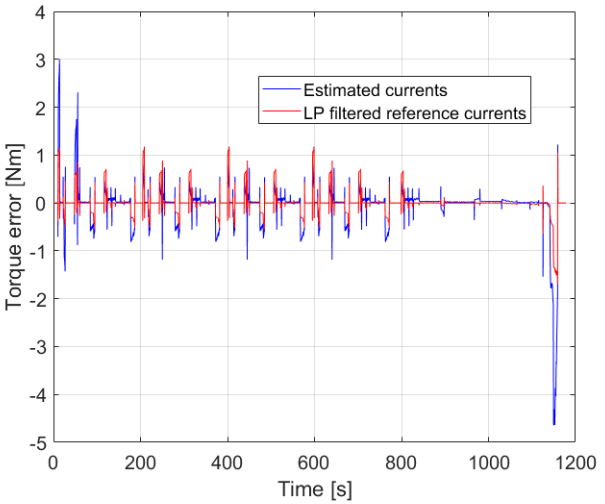

Figure 5.11: Torque estimation error using the estimated currents and the LP-filtered current reference signals from a NEDC test cycle. The estimation error was reduced when the current reference signals were low-pass filtered using the same time constant as the torque reference signal.

5.6 Effects of Different Noise Covariance Matrices

To evaluate the effect the noise covariance matrices Q and R have on estimation performance, noise was introduced in the Motor-CAD reference signal generation. How the measurement noise e and process noise v were introduced to the plant dynamics in state-space form can be seen in (3.10) and the definition of the noise covariance matrices Q and R can be found in (3.11). Noise with the following characteristics were introduced in the reference signal generation; the standard deviation of the process noise v:

$$\sigma_{I_d} = 0.05\,\text{A} \quad \sigma_{I_q} = 0.05\,\text{A} \quad \sigma_{\lambda} = 2.5 \cdot 10^{-4}\,\text{Wb-t} \quad \sigma_{T_c} = 0.1^{\circ}\text{C} \tag{5.1}$$

and the standard deviation of the measurement noise e:

$$\sigma_{I_d} = 0.5\,\text{A} \quad \sigma_{I_q} = 0.5\,\text{A} \quad \sigma_{T_c} = 0.1^{\circ}\text{C} \tag{5.2}$$

Noisy reference signals were generated for a NEDC test cycle and the Kalman filter Q and R matrices were chosen to match the noise variances of the reference signal. In practice, the noise covariance matrices needed to be tuned to work properly and to increase the weight of the model estimation, a gain was applied to the R matrices during simulation. The L_1-norm average estimation errors as a function of

R gain, k_R, can be found in Figures 5.12 and 5.13, where the torque reference signal used for the evaluation is the LP-filtered input signal to the KF and LUTs. Of the choices included in the test, $k_R = 10^5$ and $k_R = 10^6$ showed the greatest improvements in rotor temperature estimation performance. A plot of the rotor temperature estimation and error using some of the best choices of R gain along with the unmodified Q and R matrices, that matched the noise variance in the reference signal generation, are found in Figure 5.14. The final choice of k_R was dependent on the prioritization of either the rotor temperature or torque estimation.

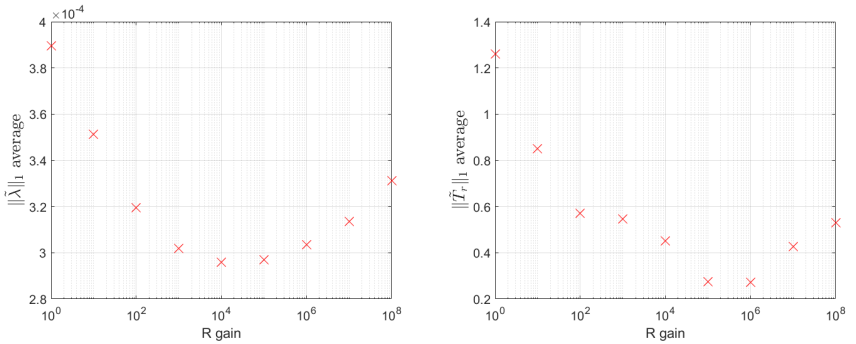

(a) Flux linkage estimation error.

(b) Rotor temperature estimation error.

Figure 5.12: L_1-norm average of flux linkage and rotor temperature estimation error with a noisy NEDC test cycle using different R gains.

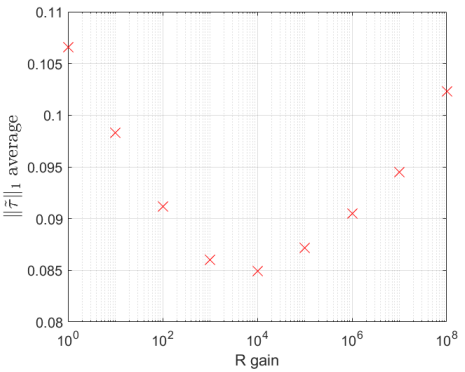

Figure 5.13: L_1-norm average of torque estimation error with a noisy NEDC test cycle using different R gains.

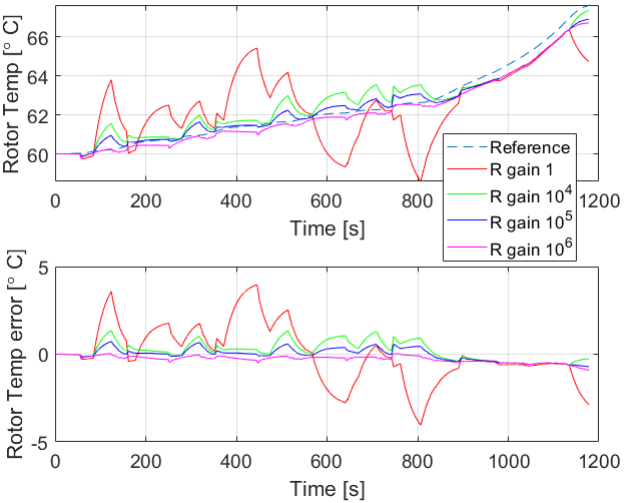

Figure 5.14: Rotor temperature estimation with a noisy NEDC test cycle for different R gains.

Increasing the magnitude of the R matrix increases the trustworthiness of the model in contrast to the measurement signal with the same order and has the ability to slow down the estimation speed. In Figure 5.15, the effects of the increasing model reliance by increasing the R gain are seen when estimating the rotor temperature without added noise in the reference signal. To more clearly see the effect on all estimation errors, the L_1-norm average error has been compiled in Table 5.8. Even with minimal reference signal noise, it appears that increasing the reliance on the model through increasing the R magnitude improves the estimation results overall. Similarly to the noisy test cycle, $k_R = 10^6$ gives the best rotor temperature estimation results with a slight sacrifice in the torque estimation performance and will therefore be utilized for the rest of the analysis.

Table 5.8: Increasing the reliance on the model by increasing the magnitude of R improves the estimation results, even with minimal reference signal noise.

L_1-norm average error for different R gains, NEDC test cycle without added noise			
R gain k_R	$\|\tilde{\lambda}\|_1$ average [µWb-turns]	$\|\tilde{T}_r\|_1$ average [°C]	$\|\tilde{\tau}\|_1$ average [Nm]
1	176.84	0.6880	0.0839
10^4	160.08	0.5228	0.0739
10^5	157.22	0.3004	0.0771
10^6	156.65	0.2619	0.0811

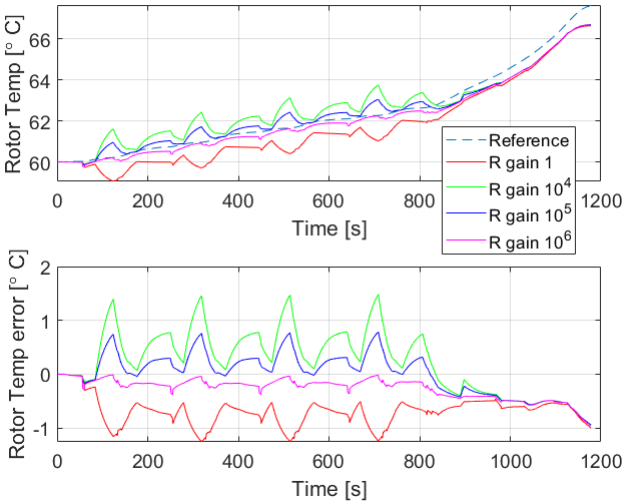

Figure 5.15: Rotor temperature estimation and error for different R gains from a NEDC test cycle without added noise.

5.7 The Effect of Low-pass Filters

Test Cycle without Added Noise

An actuation-torque reference signal LP-filter was introduced to remove high-frequency components that might arise from the current regulator and the added noise in the reference-signal generation. It is important that noise is removed from the torque-actuation reference signal because of its utilization in both the logic for the dynamic coolant temperature KF low-speed estimator switch as well as an input for LUTs. The effect of using these LP-filters was not very substantial during simulation tests without added noise in the reference signal generation, and a comparison of this can be found in Figure 5.16. It was, however, important to match the time constants of the LP-filters for the torque and current reference signals, when using the current reference signal to estimate the torque, which were both chosen as 0.1 s.

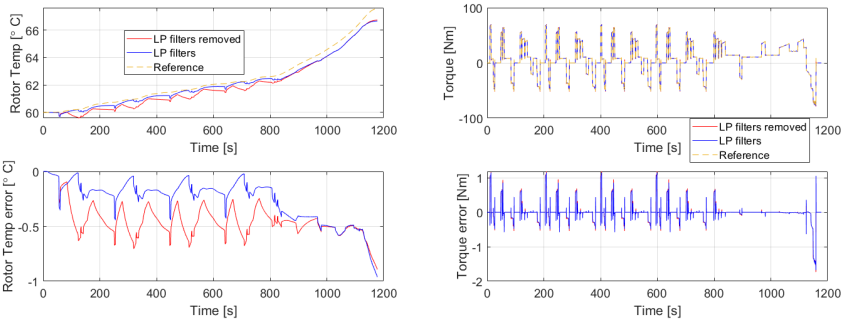

(a) Rotor temperature estimation.

(b) Torque estimation.

Figure 5.16: Rotor temperature and torque estimation with and without reference signal LP-filters, for a NEDC test cycle without added noise.

Noisy Test Cycle

The flux linkage estimation plot is not very enlightening to analyze because of the reference signals' noisiness, but the LUT inductance gives some insight into how a noisy actuation-torque reference input signal can effect the estimation, which can be seen in Figure 5.17. How the time constant for the torque-reference signal LP-filter effects the rotor temperature estimation can be seen in Figure 5.18. It can be difficult to discern any differences from a torque estimation plot. Instead, by matching the current and torque reference LP-filter time constants, the L_1-norm error average when using a time constant of 0.1 s gives an average $\|\tau\|_1 = 0.0910$ Nm and a time constant of 0.01 s gives an average $\|\tau\|_1 = 0.1162$ Nm. For both the rotor temperature and torque estimation, an LP-filter time constant choice of 0.1 s appears to work well.

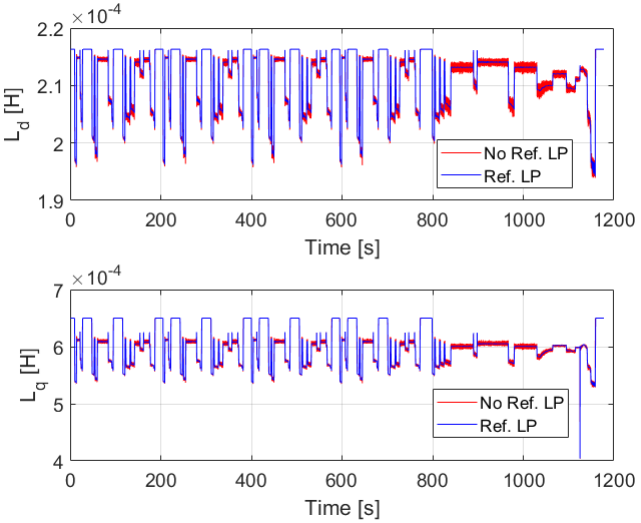

Figure 5.17: LUT inductances using noisy and LP-filtered torque-reference signal.

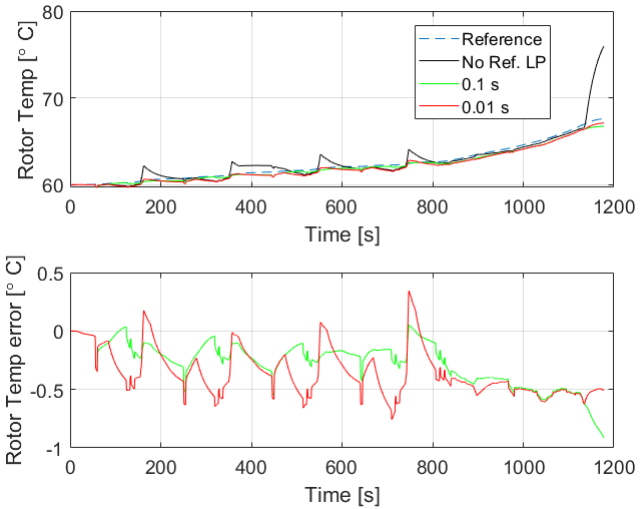

Figure 5.18: Rotor temperature estimation and error for different torque reference LP-filter time constants.

Rotor Temperature Estimation LP-Filter

The PM rotor temperature LP-filter was introduced to smooth out LUT changes in the λ_{m0} working point. The λ_{m0} working point was used in (2.10) to convert the estimated flux linkage value to its equivalent rotor temperature value. The rotor temperature estimation for different LP-filter time constants are shown in Figure 5.19, where the LP-filters are all initialized at coolant temperature. The rotor temperature estimation from a flux linkage value is very sensitive and the change in λ_{m0} working point can lead to large rotor temperature changes. Choosing the LP-filter time constant is a balancing act of increasing the average estimation error and reducing the estimation error spikes that can occur from changes in the λ_{m0} working point.

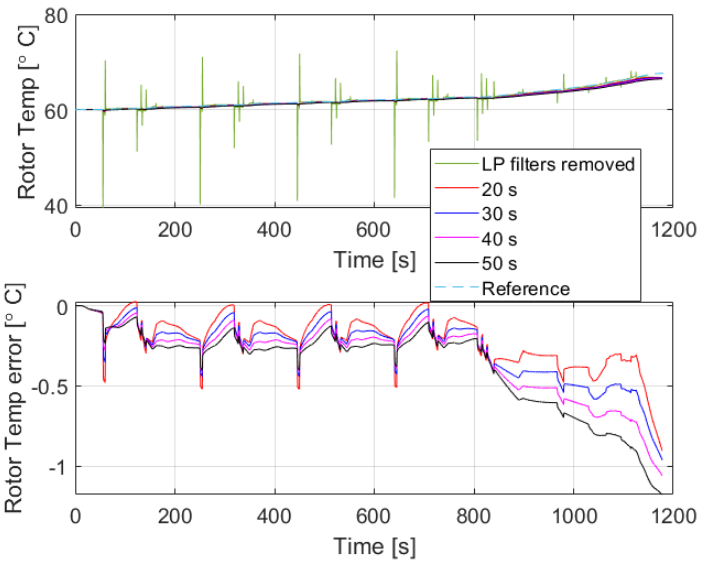

Figure 5.19: Rotor temperature estimation and error for different T_r estimate LP-filter time constants.

5.8 Sensitivity Analysis

A sensitivity analysis of the different model parameters and input signals was conducted for three steady-state operating points.

Table 5.9: Steady state operating points used for the sensitivity analysis. The approximate vehicle speed is also shown for a given rotor speed.

Operating points:	Torque [Nm]	Rotor speed [rpm]
High Torque – Low Speed:	250 Nm	1200 rpm ($\approx$ 19 km/h)
Mid Torque – Mid Speed:	100 Nm	3000 rpm ($\approx$ 50 km/h)
Low Torque – High Speed:	50 Nm	7000 rpm ($\approx$ 115 km/h)

Tables showing the results of the steady-state errors in the last 100 seconds for different operating points are presented. A parameter perturbation error of $+10\%$ was introduced to the respective parameters. The results are compiled in tables with the high torque – low speed results found in Table 5.10, the mid torque – mid speed results in Table 5.11 and the low torque – high speed results in Table 5.12.

Table 5.10: Sensitivity analysis of high torque – low speed operating point.

High Torque – Low Speed, Steady-state error table			
Parameter increase of 10%	Flux linkage error [µWb-turns]	Rotor Temperature error [°C]	Torque error [Nm]
Default	26.51	-0.0713	0.3587
R_s	-535.3	8.471	-0.6567
L_d	4300	-65.70	0.3570
L_q	335.3	-4.765	19.92
V_d	-303.5	4.946	-0.2377
V_q	3900	-58.85	7.340

Table 5.11: Sensitivity analysis of mid torque – mid speed operating point.

Mid Torque – Mid Speed, Steady-state error table			
Parameter increase of 10%	Flux linkage error [µWb-turns]	Rotor Temperature error [°C]	Torque error [Nm]
Default	-9.985	-0.4632	-0.0289
R_s	-114.2	0.9613	-0.1239
L_d	1500	-20.56	-0.0290
L_q	49.64	-1.278	3.652
V_d	-72.13	0.3862	-0.0855
V_q	7100	-98.09	6.478

Table 5.12: Sensitivity analysis of low torque – high speed operating point.

Low Torque – High Speed, Steady-state error table			
Parameter increase of 10%	Flux linkage error [µWb-turns]	Rotor Temperature error [°C]	Torque error [Nm]
Default	-6.788	-0.5183	-0.0109
R_s	-24.84	-0.2804	-0.0173
L_d	2900	-39.38	-0.0110
L_q	3.931	-0.6596	2.961
V_d	-18.08	-0.3694	-0.0149
V_q	5800	-76.94	2.060

The introduction of parameter and signal perturbations leads to several convoluted interactions. A few perturbation errors lead to errors that cancel out, the most prominent example being L_d perturbations that yield accurate torque estimations. Other perturbations lead to the default steady-state error switching sign and resulting in a similar or even smaller absolute error; this occurs for a number of V_d estimations, e.g., the torque error in the high torque – low speed operating point. The perturbations on V_d and R_s do not lead to severe estimation errors, but their effects alternate depending on the operating point, with similar performance or even an improvement for either the rotor temperature or torque estimation but a degradation of the other estimation.

The largest effect the perturbations had on the overall performance was during the high torque – low speed operating point, the operating region with the largest current magnitudes. The error appears to become more pronounced when the currents are large. The other two operating points have larger voltages instead, which appears to yield worse rotor temperature errors for V_q pertubations. Between medium torque – medium speed and low torque – high speed, medium torque and speed has a larger I_q current, but in turn the low torque – high speed point has a larger I_d current. From that, it appears that the size of the I_q current magnitude is generally more important for the estimation results.

Of the parameter and signal perturbations that have the greatest consistent impact, the inductances L_d and L_q stand out; with the rotor temperature estimation being very sensitive to L_d errors and the torque estimation to L_q errors. The V_q voltage error also appears to severely impair both the rotor temperature and torque estimation. There is also a discussion to be had on the respective error tolerances. The parameters L_d, L_q and R_s can vary during operation and if their updating mechanism is not sufficient, an error margin of 10% is more reasonable to expect for the parameters. The voltage signals are already in use to regulate the motor, and a 10% voltage error tolerance is most likely too high to warrant estimating the rotor temperature in an attempt to increase the motor performance.

5.9 Sample Rate Tests

To evaluate the theoretically hypothesized sampling rates, a number of different Kalman filter sampling rates were tested during simulation. Figures showing the results of the flux linkage estimation and torque estimation are displayed in Figure 5.20 and for the PM rotor temperature in Figure 5.21. The average estimation errors are shown in Table 5.13. The average estimation error was reduced with increasing sampling frequency; the improvement from using a 2 kHz sampling frequency to 5 kHz might, however, not justify the increase in hardware demand. The rotor temperature estimation figure also shows that the 500 Hz and 5 kHz sampling rate tests give estimation error spikes, but at different times. The 500 Hz estimation spike occurs when the KF switches from the low-speed estimator to the regular KF, while the 5 kHz sampling frequency test experiences a diverging estimation error during the low-speed estimator instead. The low-speed estimation error can, however, be tuned to better fit a 5 kHz sampling frequency by calibrating the low-speed thresholds,τ_m, or even the rotor temperature LP-filter time constant.

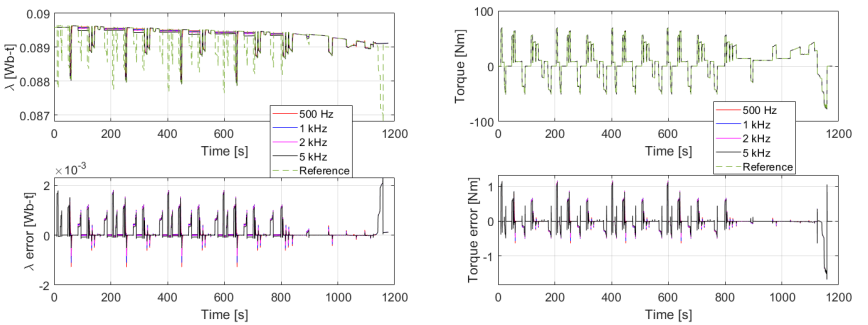

(a) Flux linkage estimation.

(b) Torque estimation.

Figure 5.20: Flux linkage and torque estimate for different ZOH discretization sampling frequencies.

Table 5.13: The average estimation error decreases with increasing sampling frequency. The estimation improvement using a 5 kHz sampling frequency compared to 2 kHz might, however, not be worthwhile.

L_1-norm average error for different ZOH discretization sampling frequencies			
Sampling frequency [kHz]	$\|\tilde{\lambda}\|_1$ average [μWb-turns]	$\|\tilde{T}_r\|_1$ average [°C]	$\|\tilde{\tau}\|_1$ average [Nm]
0.5	177.62	0.4101	0.0863
1	164.84	0.3618	0.0836
2	156.55	0.2619	0.0811
5	156.60	0.2519	0.0779

The sampling frequency effects on rotor temperature estimation with the current

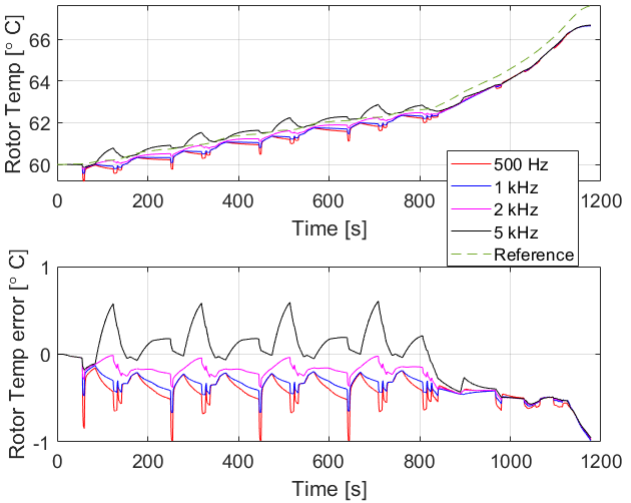

Figure 5.21: Rotor temperature estimate for different ZOH discretization sampling frequencies.

KF calibration during the WLTC cool-down period can be found in Figure 5.22 and Table 5.14. The 5 kHz sampling frequency does once again perform best, but if the marginal improvement in performance is worth the increase in hardware demand is dependent on the requirements.

Table 5.14: The average estimation error during an extensive cool-down period for different sampling frequencies. The estimation improvement using a 5 kHz sampling frequency compared to 2 kHz might, however, not be worthwhile.

L_1-norm average error for different ZOH discretization sampling frequencies, WLTC cool-down period		
Sampling frequency [kHz]	$\|\tilde{\lambda}\|_1$ average [μWb-turns]	$\|\tilde{T}_r\|_1$ average [°C]
0.5	61.885	0.6773
1	53.974	0.5498
2	46.238	0.4817
5	43.981	0.4728

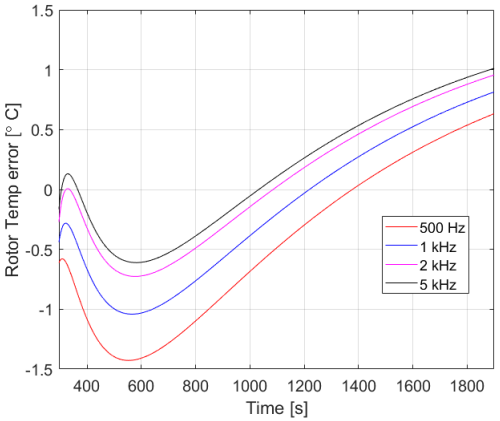

Figure 5.22: Rotor temperature estimate for different ZOH discretization sampling frequencies, during the WLTC cool-down period after a 300 second lead-in sequence with the KF active. The different initial values at the start of the cool-down period were most likely the crucial reason for the differing results.

5.10 Normalized System Simulation Analysis

The primary advantage of normalizing the system is the reduction in loss of precision. Numerical precision might not be a concern during simulation in Matlab Simulink, but it is for actual hardware implementations. The estimation results can, however, also be effected by the redistribution of signal magnitude proportions, affecting the noise covariance matrix calibrations for Q and R. In the analysis on the observability Gramian of the discrete-time system with sampling frequency 2 kHz, the largest change in eigenvalue occurred for the flux linkage state. On account of this, tests were performed on the normalized system with changes to the flux linkage process noise covariance σ_λ^2. The rotor temperature estimation in the tests can be seen in Figure 5.23. After normalizing the system, the high R gain can be removed and thereby increase the reliability of the measurement signal and the estimation speed, while having a similar estimation performance. The estimation results for the normalized system were even slightly improved by increasing the flux linkage process noise σ_λ and yielded the best overall estimation performance out of all the KF observer designs.

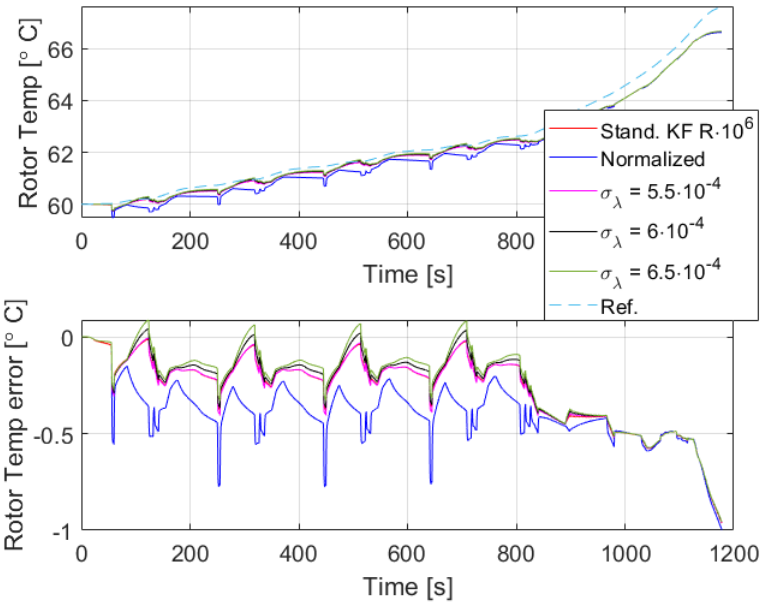

Figure 5.23: Rotor temperature estimation and error, comparing the standard KF with R gain and the normalized KF with different σ_λ.

Table 5.15: By normalizing the system, the large gain on R could be removed in favor of slight adjustments to the noise covariance matrices. The estimation results benefited slightly by increasing the λ process noise variance after normalizing the system.

L_1-norm average error for different ZOH discretization sampling frequencies			
KF Design	$\|\tilde{\lambda}\|_1$ average [μWb-turns]	$\|\tilde{T}_r\|_1$ average [°C]	$\|\tilde{\tau}\|_1$ average [Nm]
Standard KF, $R \cdot 10^6$	156.65	0.2619	0.0811
Normalized	167.52	0.3906	0.0843
Normalized, $\sigma_\lambda = 5.5 \cdot 10^{-4}$	156.96	0.2634	0.0813
Normalized, $\sigma_\lambda = 6 \cdot 10^{-4}$	156.57	0.2473	0.0809
Normalized, $\sigma_\lambda = 6.5 \cdot 10^{-4}$	156.41	0.2357	0.0806

6

Extended Kalman Filter Design

An extended Kalman filter design with inductance estimation was also developed for performance comparisons with the standard KF designs. The flux linkage estimation was highly dependent on correct inductance values and an EKF design could be a potential alternative for circumstances when the inductance accuracy in the model is poor. The EKF utilizes Jacobians of the discrete-time system model and the process of obtaining them was included in the EKF design. A preliminary analysis was also performed on the observer gains and observability Gramian to guide the design of the EKF algorithm to be implemented. An observability analysis was also conducted on a system with rescaled state variables, in place of the normalized system description in the linear case.

Inspiration for an alternative EKF design was found in [Vyncke et al., 2010], where the state vector is instead augmented with inverted inductances $\frac{1}{L_d}$ and $\frac{1}{L_q}$. The primary interest in that article was stator flux estimation of a surface-mounted PMSM in a stationary reference frame, $\alpha\beta$, where the saliency was considered low and the reluctance of the direct and quadrature axes was nearly identical. In the research article [Vyncke et al., 2010], the state vector was augmented with the inverted stator inductance, $\frac{1}{L_s}$, to reduce the complexity of the partial differentiation of the nonlinear state transition and observation functions $f(x,u)$ and $h(x,u)$, respectively. To alter between an EKF implementation with inductance estimation to an inverted inductance estimation is relatively straightforward, and as a result, both versions were chosen for comparison.

6.1 Symbolic Differentiation

The extended Kalman filter utilizes the partial differentiation of $f(x,u)$, defined by:

$$\dot{x} = f(x,u) \tag{6.1}$$

$$\begin{bmatrix} \dot{I}_d \\ \dot{I}_q \\ \dot{\lambda} \\ \dot{T}_c \\ \dot{L}_d \\ \dot{L}_q \end{bmatrix} = \begin{bmatrix} \frac{1}{L_d}(-R_s I_d + \omega_e L_q I_q + V_d) \\ \frac{1}{L_q}(-\omega_e L_d I_d - R_s I_q - \omega_e \lambda_m + V_q) \\ -\frac{\lambda}{\tau_m} + \frac{\lambda_{m0} B_r T_c}{\tau_m} + \frac{\lambda_0^0}{\tau_m} \\ -\frac{T_c}{\tau_m} \\ -\frac{L_d}{\tau_L} \\ -\frac{L_q}{\tau_L} \end{bmatrix} \tag{6.2}$$

and $h(x,u)$ defined by:

$$y = h(x,u) \tag{6.3}$$

$$\begin{bmatrix} y_1 \\ y_2 \\ y_3 \end{bmatrix} = \begin{bmatrix} I_d \\ I_q \\ T_c \end{bmatrix} \tag{6.4}$$

to linearize around the current state estimate, using the same input signal u as the dynamic-T_c KF. The partial differentiation is described by matrices F_k and H_k, defined in (3.22) and (3.23). The nonlinear state-space description is based on the system with coolant temperature (4.15) – (4.16) in Section 4.8, expanded with inductance estimation. The state observation function $h(x,u)$ does, unlike the state transition function, remain linear after the introduction of inductance estimation. To avoid the previous observability analysis issues, slow inductance time dynamics are also introduced. A brief analysis on the effects of introducing slow time dynamics for the inductances can be found in Section 6.3.

In cases where the differentiation of the nonlinear functions is deemed too complex or computationally expensive, numerical derivatives might be considered [Gustafsson, 2012]. For the PMSM model it is, however, possible to generate analytic derivatives of the continuous-time state-space model and avoid having to numerically approximate the derivatives at every sample. To define the analytic Jacobians, $f'(x,u)$ and $h'(x,u)$, symbolically in a discrete-time EKF implementation, some form of discretization of the continuous-time model dynamics has to be employed in conjunction. One approach is to start by linearizing around the current state estimate $\hat{x}_0$, utilizing a Taylor expansion. After linearization, the EKF algorithm reverts back to the standard KF, and the linear ZOH method for discretizing the system can be applied. When linearizing around a stationary equilibrium point, the new state and input vector, Δx and Δu, describe the deviation from the linearization point. We are, however, not interested in regulating the signal around a chosen constant reference signal. To be able to create Δx and Δu, that describe the deviation from the current state estimate $\hat{x}_0$, a reference trajectory of the state vector and

input signal is instead required, which is not accessible. The selection of discretization method is not directly apparent and the different methods under consideration are presented.

Forward Euler Method

The discretization of the nonlinear continuous-time state transition function $f(x,u)$, is very similar to the linear case when applying the forward Euler method. Forward Euler is an explicit method [Michael Zeltkevic, 1998a] and by using the differential operator approximation:

$$\frac{dx(t)}{dt} \approx \frac{x[k+1]-x[k]}{h} \tag{6.5}$$

the next step state-prediction and its discrete-time nonlinear state-transition $f_d(x[k],u[k])$ is given by:

$$x[k+1] = x[k] + h \cdot f(x(t),u(t)) = f_d(x[k],u[k]) \tag{6.6}$$

where the current time t is related to the time step k and sampling time h with $t = hk$. The state observation model $h(x(t),u(t))$ is unaffected by the introduction of inductance estimation as well as the forwards Euler method, leading to the EKF state observation reverting back to KF implementations. The Jacobian of the discrete-time nonlinear state-transition $F_k = f'_d(x_{k|k},u_k)$ is then given by:

$$F = \begin{bmatrix} 1-\frac{hR_s}{L_d} & \frac{h\omega L_q}{L_d} & 0 & 0 & \frac{h(R_sI_d-\omega L_qI_q-V_d)}{L_d^2} & \frac{h\omega I_q}{L_d} \\ -\frac{h\omega L_d}{L_q} & 1-\frac{hR_s}{L_q} & -\frac{h\omega}{L_q} & 0 & -\frac{h\omega I_d}{L_q} & \frac{h(\omega L_dI_d+R_sI_q+\omega\lambda-V_q)}{L_q^2} \\ 0 & 0 & 1-\frac{h}{\tau_m} & \frac{h\lambda_0 B_r}{\tau_m} & 0 & 0 \\ 0 & 0 & 0 & 1-\frac{h}{\tau_m} & 0 & 0 \\ 0 & 0 & 0 & 0 & 1-\frac{h}{\tau_L} & 0 \\ 0 & 0 & 0 & 0 & 0 & 1-\frac{h}{\tau_L} \end{bmatrix} \tag{6.7}$$

The state estimation vector $\hat{x}$, measured output y and input signal u are defined as:

$$\hat{x} = [\hat{I}_d,\hat{I}_q,\hat{\lambda},\hat{T}_c,\hat{L}_d,\hat{L}_q]^T \quad y = [I_d,I_q,T_c]^T \quad u = [V_d,V_q,\lambda_0^0]^T \tag{6.8}$$

For the inverted inductance version with $\frac{1}{L_d} = L_{d_i}$ and $\frac{1}{L_q} = L_{q_i}$, the Jacobian F_{inv_k} is instead given by:

$$F_{inv} = \begin{bmatrix} 1-hR_sL_{d_i} & \frac{h\omega L_{d_i}}{L_{q_i}} & 0 & 0 & h(-R_sI_d+\frac{\omega I_q}{L_{q_i}}+V_d) & -\frac{h\omega L_{d_i}I_q}{L_{q_i}^2} \\ -\frac{h\omega L_{q_i}}{L_{d_i}} & 1-hR_sL_{q_i} & -h\omega L_{q_i} & 0 & \frac{h\omega I_d L_{q_i}}{L_{d_i}^2} & h(-\frac{\omega I_d}{L_{d_i}}-R_sI_q-\omega\lambda+V_q) \\ 0 & 0 & 1-\frac{h}{\tau_m} & \frac{h\lambda_0 B_r}{\tau_m} & 0 & 0 \\ 0 & 0 & 0 & 1-\frac{h}{\tau_m} & 0 & 0 \\ 0 & 0 & 0 & 0 & 1-\frac{h}{\tau_L} & 0 \\ 0 & 0 & 0 & 0 & 0 & 1-\frac{h}{\tau_L} \end{bmatrix} \tag{6.9}$$

The state estimation vector $\hat{x}_{inv}$, measured output y and input signal u are defined as:

$$\hat{x}_{inv} = [\hat{I}_d, \hat{I}_q, \hat{\lambda}, \hat{T}_c, \hat{L}_{d_i}, \hat{L}_{q_i}]^T \quad y = [I_d, I_q, T_c]^T \quad u = [V_d, V_q, \lambda_0^0]^T \tag{6.10}$$

Backward Euler Method

For nonlinear systems, the backward Euler method is slightly more complicated to implement. With the differential operator approximation:

$$\frac{dx(t)}{dt} \approx \frac{x[k]-x[k-1]}{h} \tag{6.11}$$

the nonlinear state dynamics after a time shift forward becomes:

$$x[k+1] = x[k] + h \cdot f(x(t+h), u(t+h)) \tag{6.12}$$

To obtain $x[k+1], u[k+1]$, a root-finding technique such as the Newton-Raphson method [Michael Zeltkevic, 1998a] can be employed to solve the nonlinear equation:

$$x_i[k+1] - h \cdot f_i(x[k+1], u[k+1]) = x_i[k] \tag{6.13}$$

where the index i refers to the different states. Backward Euler is an implicit method and there is a trade-off between an increase in computational cost for numerical stability [Michael Zeltkevic, 1998a].

An alternative is to use a predictor-corrector method [Michael Zeltkevic, 1998b], an explicit and implicit method in combination. By first approximating $x[k+1]$ with an explicit method and then correcting with an implicit technique. A combination of forward and backward Euler method yields:
Predictor

$$x^p[k+1] = x[k] + h \cdot f(x(t), u(t))]) \tag{6.14}$$

Corrector

$$x[k+1] = x[k] + hf(x^p[k+1], u^p[k+1]) \tag{6.15}$$

The predictor-corrector method is considered an explicit method and is most often used with higher-order implicit methods for the correction step [Michael Zeltkevic, 1998b]. If a predictor-corrector method is chosen, another more commonly used implicit technique might be preferred. An issue that, also, arises with the predictor-corrector is the need for an approximation of the next input signal $u^p[k+1]$, for which we do not either have a model for or some reference trajectory.

The higher computational cost to use the implicit method with a root-finding technique could be an interesting option to investigate if numerical stability issues arise and if time is available.

6.2 Extended Kalman Gain Analysis

The EKF observer gain analysis utilizes the state-transition Jacobian F_k, which incorporates the currents and voltages. To analyze how the observer gain K behaves in relation to the electrical angular speed, a limited number of specific and properly parameterized operating points were investigated, shown in Table 6.1.

Table 6.1: Torque and rotor speed for the chosen operating points. The values within the parenthesis is a rough equivalent of the vehicle speed.

Operating points:	Torque [Nm]	Rotor speed [rpm]
High Torque - Very Low Speed (HT-VLS):	250 Nm	100 rpm ($\approx$ 1.6 km/h)
High Torque - Low Speed (HT-LS):	250 Nm	1200 rpm ($\approx$ 19 km/h)
Mid Torque - Mid Speed (MT-MS):	100 Nm	3000 rpm ($\approx$ 50 km/h)
Low Torque - High Speed (LT-HS):	50 Nm	7000 rpm ($\approx$ 115 km/h)

The observer gains K after 50 iterations of the EKF algorithm, for the four operating points using the standard inductance EKF are found in Figure 6.1. The Q and R covariance matrices are similar to the dynamic-T_c KF, using the standard deviations σ in (5.1) – (5.2) with the following alterations to the process noise v:

$$\sigma_\lambda = 2 \cdot 10^{-4}\,\text{Wb-t} \quad \sigma_{L_d} = 7 \cdot 10^{-7}\,\text{H} \quad \sigma_{L_q} = 3 \cdot 10^{-6}\,\text{H} \tag{6.16}$$

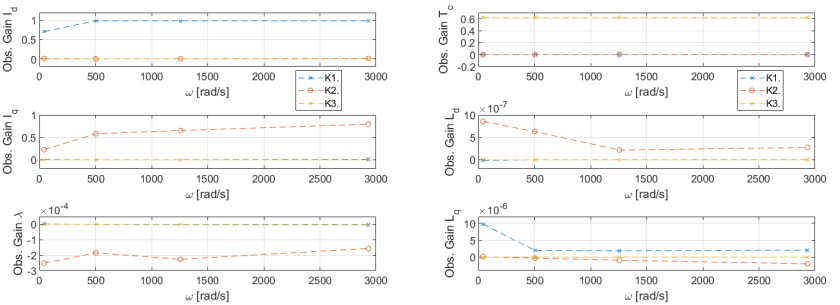

Figure 6.1: Observer gains for the standard inductance EKF, with sampling frequency 2 kHz. The observer gains K_1, K_2 and K_3 correspond to the measured states y, or I_d, I_q and T_c, respectively.

The particularly low inductance σ settings were chosen from simulations study tests, dampening rapid estimation changes. The observer gain tests show that the states I_d, I_q and T_c are largely dependent on their respective measurement signal, with the gains for the coolant temperature T_c staying constant across all operating points. The current gains experience a slight dip at very low speeds, when the currents are large but the voltages are smaller. The flux linkage estimation is mostly dependent on the measured I_q current, which is an expected result based on the model. The λ gain increase is not as pronounced at low speeds, in contrast to the linear KF model. The inductance gains do, however, experience a greater increase during lower speeds when the torque is large. The larger observer gains and currents during very slow speeds and high torques could lead to inductance estimation spikes. It also seems that L_d estimate is mostly influenced by the current measurement I_q while the L_q estimate instead primarily is influenced by the I_d measurement.

The observer gain results for the inverted inductance EKF are found in Figure 6.2. The changes to the standard deviation of the process noise v are as follows:

$$\sigma_{L_{d_i}} = 20\,\mathrm{H}^{-1} \quad \sigma_{L_{q_i}} = 100\,\mathrm{H}^{-1} \tag{6.17}$$

The only notable differences in the results are with the inductances, with the expected change to negative gains from the differentiation of the inverted variable. The inverted inductance states also experience a similar increase in gain during low speeds. The differences in state magnitudes could also have a large impact on the numerical uncertainty of the system and the necessity of rescaling the flux linkage magnitude that needs to be further investigated.

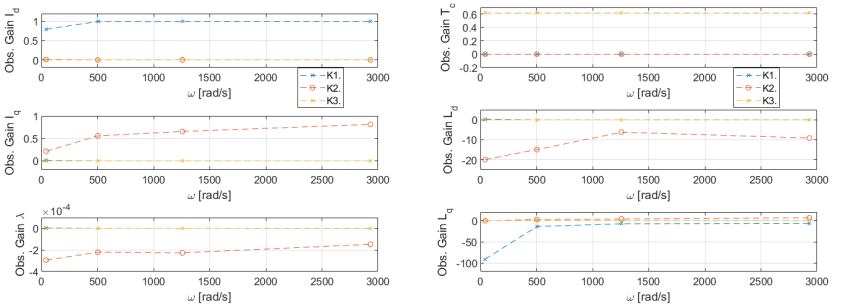

Figure 6.2: Observer gains for the inverted inductance EKF, with sampling frequency 2 kHz. The observer gains K_1, K_2 and K_3 correspond to the measured states y, or I_d, I_q and T_c, respectively.

6.3 Slow and Zero Inductance Dynamics Comparison

Similar to the KF design, a test was also conducted to investigate if the slow inductance time dynamics, introduced to be able to generate the observability Gramian, have a minimal impact on the system. The inductance time constant τ_L was chosen to be similar in size as the PM time constant, with $\tau_L = 2000$ s. The relative % difference in observer gain compared to zero inductance dynamics is shown in Figure 6.3 for the standard inductance EKF and in Figure 6.4 for the inverted inductance EKF. The difference is overall very small, with slightly smaller differences for the standard inductance EKF for some of the states.

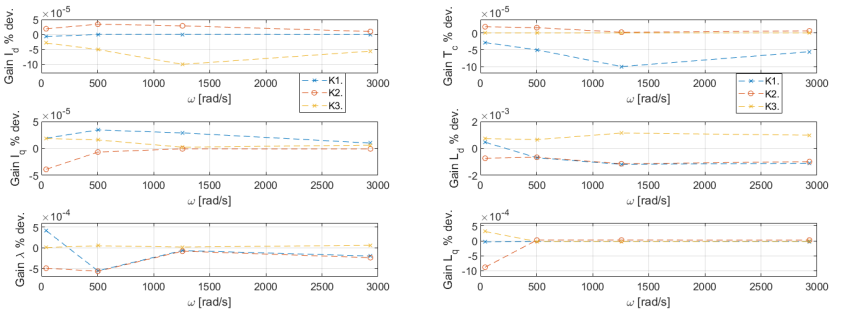

Figure 6.3: The % deviation in observer gains for the standard inductance EKF, with sampling frequency 2 kHz. Comparing no and slow inductance dynamics.

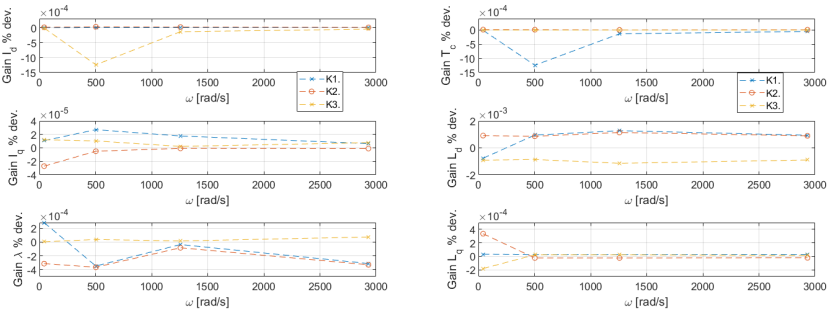

Figure 6.4: The % deviation in observer gains for the inverted inductance EKF, with sampling frequency 2 kHz. Comparing no and slow inductance dynamics.

6.4 Observability Gramian

Continuous-time System Analysis

To analyze the observability of the non-linear system, the observability Gramian $\mathscr{O}_x$ was generated with the already linear state observation function $h(x,u)$, and the Jacobian of the state transition function $f'_x(x,u)$. The linearization was conducted around the same operating points used in the observer gain analysis with a few additions. The input-signal magnitudes that result in output norm $\|y\|_1 = 1$ using $\mathscr{O}_x$ are found in Table 6.2 for the standard inductance EKF and in Table 6.3 for the inverted inductance EKF. An additional operating point at near standstill, with torque and rotor speed close to 0, was also examined.

Table 6.2: Compiled results for the standard inductance EKF. Identical results to the inverted inductance design for the currents and flux linkage were obtained, with a similar large reduction in observability at the near standstill operating point for λ, L_d and L_q.

State magnitudes $\{x \in \mathbb{R}^n;\ x^T \mathscr{O}_x(\omega)x = 1\}$					
Operating point	$\lvert I_d \rvert$ [A]	$\lvert I_q \rvert$ [A]	$\lvert \lambda \rvert$ [Wb-t]	$\lvert L_d \rvert$ [H]	$\lvert L_q \rvert$ [H]
Near standstill	8.69	5.17	29.58	$5.53{\cdot}10^{-3}$	$1.72{\cdot}10^{-2}$
HT - VLS	10.78	5.13	$8.28{\cdot}10^{-6}$	$2.65{\cdot}10^{-8}$	$3.96{\cdot}10^{-8}$
HT - LS	11.19	4.61	$5.71{\cdot}10^{-6}$	$1.79{\cdot}10^{-8}$	$3.98{\cdot}10^{-8}$
MT - MS	10.24	3.78	$6.80{\cdot}10^{-6}$	$7.46{\cdot}10^{-6}$	$1.05{\cdot}10^{-7}$
LT - HS	9.69	3.44	$7.58{\cdot}10^{-6}$	$4.58{\cdot}10^{-6}$	$3.08{\cdot}10^{-7}$

Table 6.3: Compiled results for the inverted inductance EKF. The inductance state magnitude are much larger as well as the required input-signal inductance magnitudes for an output norm equal to one compared to the standard inductance design.

State magnitudes $\{x \in \mathbb{R}^n;\, x^T \mathcal{O}_x(\omega)x = 1\}$					
Operating point	$\lvert I_d \rvert$ [A]	$\lvert I_q \rvert$ [A]	$\lvert \lambda \rvert$ [Wb-t]	$\lvert L_{d_i} \rvert$ [H^{-1}]	$\lvert L_{q_i} \rvert$ [H^{-1}]
Near standstill	8.69	5.17	29.58	$1.21{\cdot}10^{5}$	$4.70{\cdot}10^{4}$
HT - VLS	10.78	5.13	$8.28{\cdot}10^{-6}$	1.09	0.275
HT - LS	11.19	4.61	$5.71{\cdot}10^{-6}$	0.735	0.277
MT - MS	10.24	3.78	$6.80{\cdot}10^{-6}$	2.15	0.413
LT - HS	9.69	3.44	$7.58{\cdot}10^{-6}$	1.063	0.900

The table results show that both EKF designs have great difficulty estimating the flux linkage and the inductances at near standstill when both the currents and voltages are low. Of the remaining operating points, the flux linkage observability is at its worst at very low speeds, but because the EKF flux linkage observer gains do not experience any significant increases at this operating point, it might not lead to issues during simulations. It also appears that the torque has a great impact on the flux linkage observability, with the high torque - low speed operating point giving the best result. The inductances also share the highest observability at the high torque - low speed operating point, with a significant L_d observability decrease for lower torque operating points and a slightly smaller decrease for L_q. The inductance state magnitudes for the inverted inductance EKF is much larger and the required input-signal magnitude for an output norm equal to one is also much larger, but the observability results for the currents and flux linkage are still identical with the standard inductance EKF. The changes in observability for the different operating points are, however, not as dramatic for the inverted inductances. For both designs, it appears that the L_q observability is most dependent on high torque, but for L_d it is not as straightforward with the mid torque - mid speed point yielding the worst observability.

An additional operating point: mid torque - low speed: 100 Nm - 1200 rpm, was also tested to investigate how the observability changes with torque by comparing the results with the high torque - low speed operating point. The eigenvalues of $\mathcal{O}_x$ are displayed in Figure 6.5 and Figure 6.6 for the standard and inverted inductance EKF, respectively. The eigenvector decomposition of $\mathcal{O}_x$ still gives eigenvectors that are strongly associated with the original states but the inductance directions can, especially during slower speeds, be a stronger mix of each other. Both EKF designs show a clear observability increase with increased torque for all states except the currents. Comparing the eigenvalue magnitudes for the different EKF designs also shows the risk for very high condition numbers. In Figure 6.7 the condition number $\kappa(\mathcal{O}_x)$ is shown for both designs using both a Matlab routine and the singular value quotient definition. Figure 6.7 shows that the inverted inductance EKF has increased numerical sensitivity at lower speed but is surpassed by the standard inductance EKF at higher speeds.

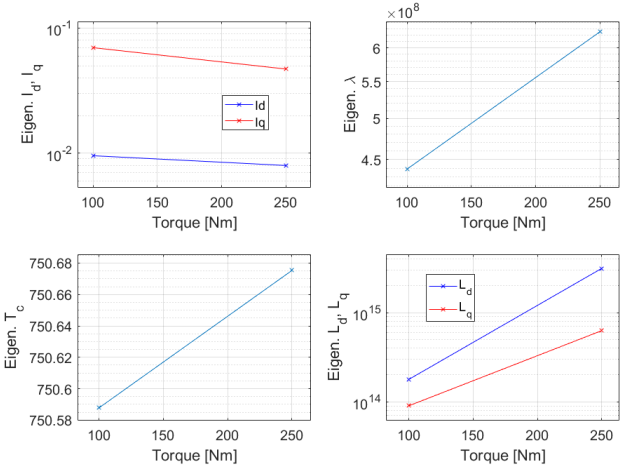

Figure 6.5: Eigenvalues of $\mathscr{O}_x$ for the continuous-time standard inductance system, linearized around different operating points to show the impact of changes in torque. With the exception of the currents, the observability of the states increased with torque.

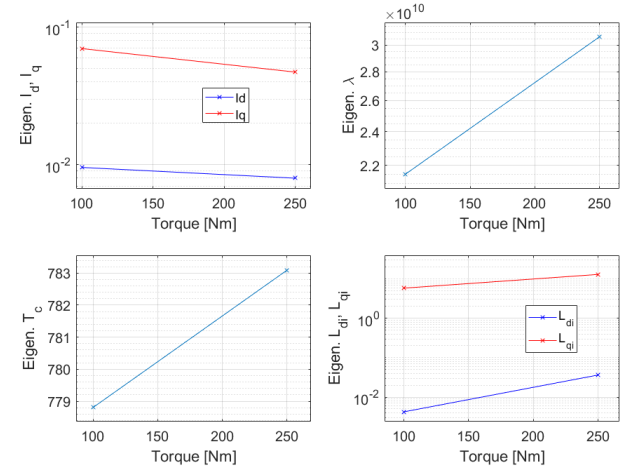

Figure 6.6: Eigenvalues of $\mathscr{O}_x$ for the continuous-time inverted inductance system, linearized around different operating points to show the impact of changes in torque. With the exception of the currents, the observability of the states increased with torque.

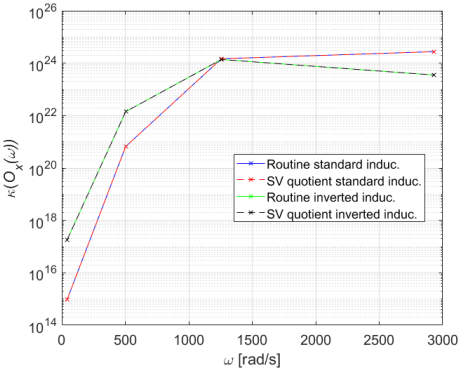

Figure 6.7: A comparison of the condition number $\kappa(\mathcal{O}_x)$, between the standard and inverted inductance continuous-time design at different operating points. Calculating the condition number using the Matlab routine `cond()` and using the singular values with (3.29) yielded identical results.

Discrete-Time System Analysis

An observability analysis was also conducted on the discrete-time system. To be able to create a stable discrete-time system using the forward Euler method, with all eigenvalues strictly within the unit circle, a sampling frequency of $\approx$ 163 kHz was required for the high speed operating point (7000 rpm). Using a 2 kHz sampling frequency, similar to the previous KF design, was only fast enough for the very low speed operating point (100 rpm) and a sampling frequency of 10 kHz was only sufficient up to the low speed point (1200 rpm). Hardware-intensive approaches to handle the unstable discrete-time dynamics is possible by increasing the sampling frequency or by using a different discretization method such as backward Euler with a root finding method. Another approach that will be tested is to suppress the observer gains at higher speed by recalibrating Q and R, in a simple form of gain scheduling [Glad and Ljung, 2003]. The discrete-time $\mathcal{O}_x$ eigenvalues are found in Figure 6.8 and in Figure 6.9 for the standard and inverted inductance EKFs, respectively. The eigenvalue decomposition was the same as the continuous-time system with regards to the increased mix of the inductance directions, and to a lesser extent the mix of the currents, at very low speeds. The two designs had very similar eigenvalue characteristics for the different operating points. Similar to the continuous-time system, best flux linkage estimation results appeared to occur at the high torque and low speed operating point and the lowest observability at the very low speed point. The currents experienced a large increase in observability at high speeds, while L_q estimation appeared best during high torque operating points and L_d estimation appeared worst during mid torque and speed operating points. The major difference between the EKF designs is the reordering of the eigenvalue

magnitudes and a comparison of $\kappa(\mathcal{O}_x)$ is shown in Figure 6.10 for the discrete-time systems. The discretized system has a significantly lower condition number than the continuous-time system, but, in contrast to the KF designs, the required sampling frequency to create a stable system at higher speeds is extremely demanding. Figure 6.10 does, however, show a substantial reduction in the condition number using the discretized standard inductance EKF for all operating points compared to the inverted inductance design.

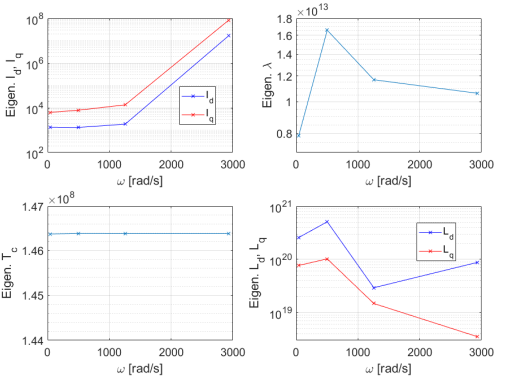

Figure 6.8: Eigenvalues of $\mathcal{O}_x$ for the discrete-time standard inductance system, linearized around different operating points. Discretized using the forward Euler method with a sampling frequency of 163 kHz.

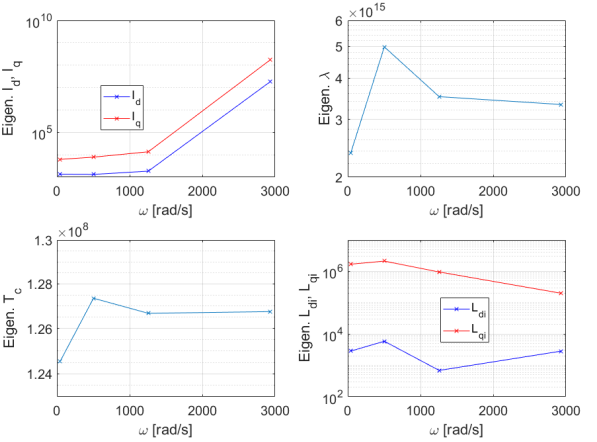

Figure 6.9: Eigenvalues of $\mathcal{O}_x$ for the discrete-time inverted inductance system, linearized around different operating points. Discretized using the forward Euler method with a sampling frequency of 163 kHz.

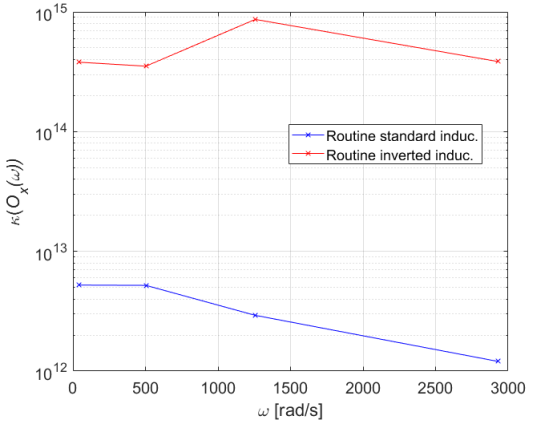

Figure 6.10: A comparison of the condition number $\kappa(\mathcal{O}_x)$, between the standard and inverted inductance discrete-time design at different operating points. Discretized using the forward Euler method with a sampling frequency of 163 kHz.

6.5 EKF Algorithm Description

The EKF algorithm implementation includes a few modifications, such as a near standstill estimator that activates when the speed is close to zero. The observability analysis in Section 6.4 showed a greatly reduced observability when both the torque and speed were low but by solely using a very low speed threshold, the low-observability estimator only remains active for a brief period if the torque is not small as well. The near standstill estimation is based on the low-speed dynamic-T_c KF design in Section 4.8, stopping the estimation error covariance matrix update and estimating the flux linkage solely with the model dynamics that slowly converge towards the coolant temperature. The inductances have a similar reduction of observability as the flux linkage near standstill and a more drastic observer gain increase at very low speeds, but the inductances do not have an equivalent of the low-speed flux linkage estimation to model their near standstill behavior. An inductance estimation solely based on the system dynamics results in the estimation slowly drifting towards the lower saturation limits during a prolonged cool down period and gives a large initial settings error when starting up afterwards. The old inductance values are therefore kept from before the switch to the near standstill estimator.

Because the inductance states appear in the denominator of some of the terms, they are saturated to avoid estimation singularities. The inductance saturation was most vital during simulations with poor initial settings. The saturation limits were chosen as modestly expanded values from the inductance LUTs, with the inverted inductance limits based on the same values.

A simple form of gain scheduling was also introduced to alter Q and R, to suppress the observer gains in an effort to deal with the unstable observer dynamics at higher rotor speeds. A more thorough analysis of the speed limits and noise covariance matrix calibrations are presented in the EKF simulation study in Section 7.1. An algorithm description is found in Algorithm 5 for both the standard and inverted inductance EKF implementations. The two designs have the same algorithm description; the differences are the system transition function $f(x,u)$ and its Jacobian F_k (or $f_{inv}(x_{inv},u)$ and F_{inv_k} respectively for the inverted inductance design), the process noise covariance matrix Q calibration, the initial settings for the states and the saturation limits. Both the state transition function and the Jacobians used in the algorithm description are the symbolically defined forward Euler discretized versions. The high-speed recalibration activates for electrical angular speeds over a high-speed threshold ω_{HS}, were Q_{HS} and a R gain k_R are used to suppress large estimation changes.

Algorithm 5 EKF with near standstill estimator switch, inductance saturation and high-speed Q and R recalibration.

Initialize internal states: $\mathrm{E}(x_0) = \hat{x}_{1|0}$, $P_{1|0} = Q$
1: **repeat**
2: **function** <EXTENDED KALMAN FILTER>(u_k, y_k, ω_k)
Q, R high-speed recalibration
3: **if** $|\omega_k| \geq \omega_{HS}$ **then**
4: $Q_k = Q_{HS}$
5: $R_k = R \cdot k_R$
6: **else**
7: $Q_k = Q$
8: $R_k = R$
9: **end if**
10: **if** $|\omega_k| \geq \omega_{threshold}$ **then**
Measurement update
11: $\varepsilon_k = y_k - h(\hat{x}_{k|k-1}, u_k)$
12: $S_k = H_k P_{k|k-1} H_k^T + R_k$
13: $K_k = P_{k|k-1} H_k^T S_k^{-1}$
14: $\hat{x}_{k|k} = \hat{x}_{k|k-1} + K_k \varepsilon_k$
15: $P_{k|k} = (I_k - K_k H_k) P_{k|k-1}$
Time update
16: $\hat{x}_{k+1|k} = f(\hat{x}_{k|k}, u_k)$ ▷ $f_{inv}(\hat{x}_{inv_{k|k}}, u_k)$ in inverted inductance design
17: $P_{k+1|k} = F_k P_{k|k} F_k^T + Q_k$ ▷ F_{inv_k} in inverted inductance design
18: **else**
Near standstill estimator
19: $L_d^{old} = \hat{x}_{k-1}(5)$
20: $L_q^{old} = \hat{x}_{k-1}(6)$
21: $\varepsilon_k = y_k - H_k \hat{x}_{k|k-1}$
22: $S_k = H_k P_{k|k-1} H_k^T + R_k$
23: $K_k = P_{k|k-1} H_k^T S_k^{-1}$
24: $K_k(3,:) = 0$
25: $\hat{x}_{k|k} = \hat{x}_{k-1|k-1} + K_k \varepsilon_k$
26: $\hat{x}_{k+1|k} = f(\hat{x}_{k|k}, u_k)$ ▷ $f_{inv}(\hat{x}_{inv_{k|k}}, u_k)$ in inverted inductance design
27: $\hat{x}_{k+1}(5) = L_d^{old}$
28: $\hat{x}_{k+1}(6) = L_q^{old}$
29: **end if**
30: **Saturate**$(\hat{L}_d, \hat{L}_q)$ ▷ $\hat{L}_{inv_d}, \hat{L}_{inv_q}$ in inverted inductance design
31: **return:** $\hat{x}_{k+1}$
32: **end function**
33: **until** Shutdown

6.6 Rescaling State-Variables

Analogous to normalizing the system description for the KF, a rescaling of the state variables to improve numerical computational robustness for the EKF estimation was attempted. The largest noticeable change from inverting the inductance states up to this point is the reordering of the state magnitudes, with the smallest state magnitude L_d becoming the largest after inversion. A more controlled rescaling of the smallest states can be done with the scaling factor k_λ to give the new flux linkage state λ_n:

$$\lambda_n = k_\lambda \cdot \lambda \tag{6.18}$$

and for the inductances with:

$$L_n = k_L \cdot L \tag{6.19}$$

Using the new rescaled state variables, the scaling factors also have to be introduced to the state transition function to preserve the validity of the system model. This results in the rescaled standard inductance state transition function:

$$f(x,u) = \begin{bmatrix} \frac{-R_s I_d k_L + \omega L_{qn} I_q + V_d k_L}{L_{d_n}} \\ \frac{-\omega L_{d_n} I_d - R_s I_q k_L - \frac{\omega \lambda k_L}{k_\lambda} + V_q k_L}{L_{qn}} \\ \frac{-\lambda + \lambda_{m0} B_r T_c k_\lambda + \lambda_0^0 k_\lambda}{\tau_m} \\ -\frac{T_c}{\tau_m} \\ -\frac{L_{d_n}}{\tau_L} \\ -\frac{L_{qn}}{\tau_L} \end{bmatrix} \tag{6.20}$$

The scaling factors are introduced to the inverted inductance model in a similar manner, before using the forward Euler method to discretize the system and finally partially differentiating the discrete-time state transition function using the rescaled variables. The scaling factor was chosen to place all the state magnitudes in a similar range. Figure 6.11 displays the effect the scaling factor has on $\kappa(\mathcal{O}_x)$ for the discrete-time standard inductance system using a sampling frequency of 163 kHz. Choosing more assertive scaling factors worked well with the continuous-time system but the discrete-time system responds better to the smaller scaling readjustments $k_\lambda = 1$ and $k_L = 500$. The eigenvalues of $\mathcal{O}_x$ for this scaling factor configuration are shown in Figure 6.12. The directions of the eigenvector decomposition for the rescaled system is, however, a lot more mixed than previously, especially during the very low speed operating point. The current eigenvectors are slightly dependent on each other and there is some dependence on λ and L_d for L_q. The greatest dependence between states is, however, between λ and L_d, which occurs for all operating

points. There are still a lot of similarities to the unscaled system in Figure 6.8, except for a increase in λ eigenvalues and a large decrease of inductances eigenvalues, with the caveat that the eigenvectors from the rescaled system are more dependent on multiple states.

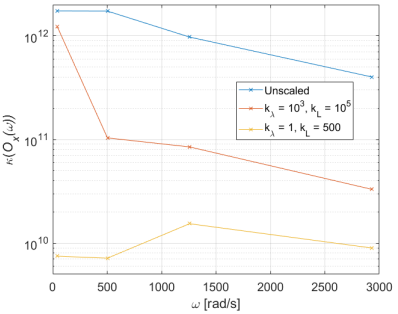

Figure 6.11: Condition number of the discrete-time standard inductance observability Gramian, with different scaling factors. The sampling frequency is 163 kHz.

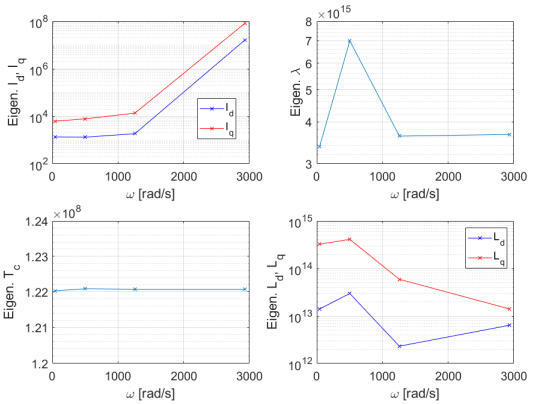

Figure 6.12: Observability Gramian eigenvalues for the discrete-time standard inductance system, with scaling factors $k_\lambda = 1$ and $k_L = 500$ and with sampling frequency 163 kHz.

The $\kappa(\mathcal{O}_x)$ for the discrete-time inverted inductance system with different scaling factors can be seen in Figure 6.13. The scaling factors that gave the best results for the discrete-time inverted inductance system were with slightly larger readjustments using $k_\lambda = 10^4$ and $k_L = 10^{-3}$, instead of using factors that placed the state magnitudes closest to a similar operating range as the remaining states. The best

scaling factors were found through manually testing different configurations and can be improved slightly with more fine tuning. The inverted inductance system does, however, have slightly larger condition numbers with the scaling factors tested, but the unscaled system also starts at higher values compared to the standard inductance system. The $\mathcal{O}_x$ eigenvalues using the scaling factors that gave the largest reduction in condition number can be found in Figure 6.14. The eigenvector decomposition is once again more mixed than the unscaled design, especially during the very low speed operating point, with the largest dependence between the T_c and λ states. A slightly lower dependence between the L_{q_i} and λ states is also present. Compared to the unscaled version in Figure 6.9, there is a large decrease in current eigenvalues, an increase for L_{d_i} and a more uniform increase in observability with increased speed for all states. The observability for T_c also experiences a large increase with increased speed compared to the other design, where the eigenvalue remained relatively constant for all operating points. This was, however, most likely due to the strong eigenvector dependence on λ.

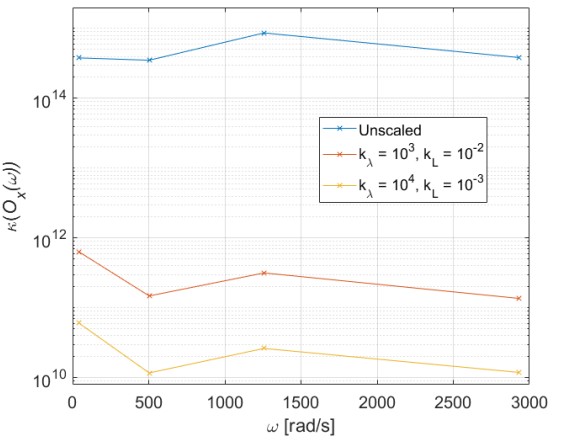

Figure 6.13: Condition number of the discrete-time inverted inductance observability Gramian, with different scaling factors. The sampling frequency is 163 kHz.

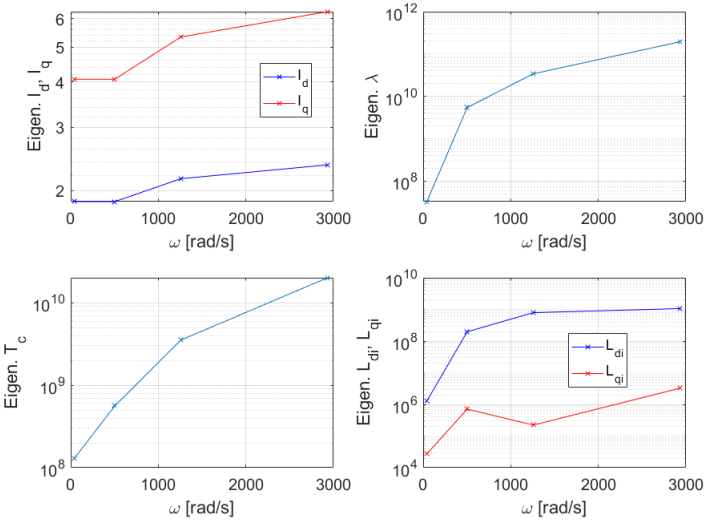

Figure 6.14: Observability Gramian eigenvalues for the discrete-time inverted inductance system, with scaling factors $k_\lambda = 10^4$ and $k_L = 10^{-3}$ and with sampling frequency 163 kHz.

7

Simulation Study, Extended Kalman Filter

This section is dedicated to the simulation-study results and analysis of the EKF with unknown inductances. A fair performance comparison was conducted, comparing the EKF design to the KF design with limited inductance accuracy. With very limited inductance information, the flux linkage and PM temperature estimation was very poor, as seen in the KF simulation results with constant inductances in Figure 5.3, and a EKF design can be a possible alternative. The inductance saturation limits are an expansion of the LUT used in the KF simulation study and the inductance initial conditions are also based on the LUT results with speed and torque inputs equal to zero. It is, however, also possible to find and tune the settings through testing. The EKF simulations were conducted with a discrete-time system discretized using forward Euler method and a 2 kHz sampling frequency, which gives an unstable system model for a majority of the operating speed range, further details can be found in Section 6.4.

7.1 Noise Covariance Matrix Simulation Analysis

Standard Inductance State Design

High-Speed Noise Covariance Matrix Simulation Analysis

The EKF was much more sensitive to noise covariance matrix settings compared to previous KF designs and a lot of effort can be dedicated to fine tuning. The default Q and R settings were chosen as in Section 6.2, (6.16), with the exception of a change to σ_λ:

$$\sigma_\lambda = 1.8 \cdot 10^{-4}\,\text{Wb-t} \tag{7.1}$$

Because the discretized system became unstable for higher rotor speeds when using the forward Euler method with a sampling frequency of 2 kHz, the noise covariance matrices were altered to suppress estimation changes at higher speeds. To calibrate

the high-speed noise covariance matrices, the first 800 seconds of the WLTC high-speed dynamic test cycle was used, see Figure 5.2. Without any calibrations for high-speed the L_d and λ estimates can strongly diverge, leading to large PM temperature estimation errors. Similarly to the sensitivity analysis in Section 5.8, the L_d estimation error did not, however, lead to any major torque estimation errors. By identifying at which rotor speeds the estimation starts to diverge, a high-speed process noise recalibration was implemented at $\omega \geq 1600$ rad/s for σ_λ and σ_{L_d}:

$$\sigma_\lambda = 1 \cdot 10^{-8}\,\text{Wb-t} \quad \sigma_{L_d} = 1 \cdot 10^{-10}\,\text{H} \tag{7.2}$$

The rotor temperature and torque estimation results, with and without high-speed Q calibration, are shown in Figure 7.1. Without altering the noise covariance matrix settings at higher speeds, the rotor temperature estimation error magnitude exceeded 200 °C but the torque estimation error magnitude was surprisingly small and never exceeded 1 Nm.

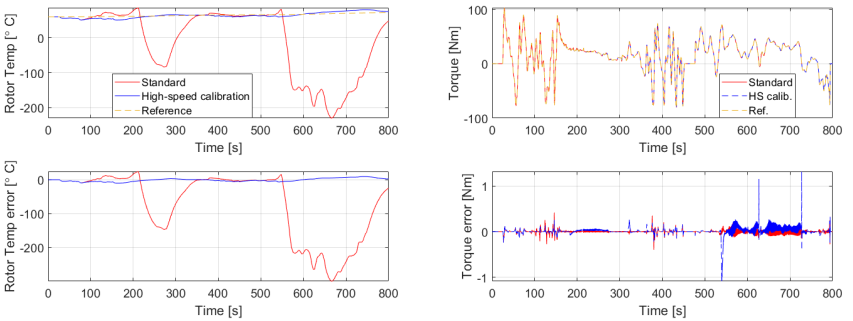

(a) Rotor temperature estimation.

(b) Torque estimation.

Figure 7.1: Rotor temperature and torque estimation results with and without the high-speed Q calibration. The standard test results refer to no alterations of Q at higher speeds, where the rotor temperature estimation error grew very large but the torque estimation performed surprisingly well.

Interpolating Design, Standard Inductances

Another design was also implemented that interpolates the Q settings between the different operating speeds and avoids excessive estimation-change suppression at mid tier operating ranges. A σ_{L_q} calibration was also introduced to avoid issues that could emerge when the σ differences were too large. Examples of neglecting σ_{L_q} changes can be found for the inverted inductance state design in Section 7.1 in Figures 7.8 and 7.9. The standard deviation, SD, of the process noise as a function of ω is shown for the interpolating design in Figure 7.2.

The rotor temperature and torque estimation results for the interpolating high-speed Q design can be found in Figure 7.3. The interpolating design allows for

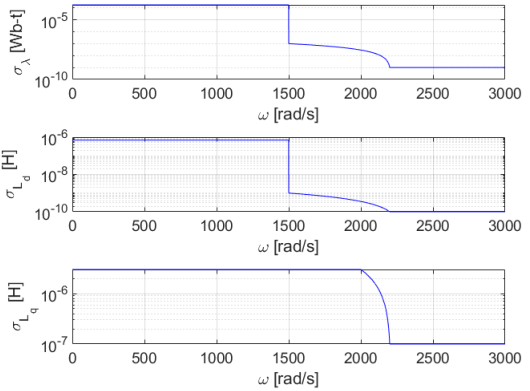

Figure 7.2: The SD of the process noise as a function of ω for the standard inductance high-speed interpolating design. Between 1500 rad/s $\leq \omega \leq$ 2200 rad/s, σ_λ linearly decreases from $1 \cdot 10^{-7}$ Wb-t to $1 \cdot 10^{-9}$ Wb-t and σ_{L_d} from $1 \cdot 10^{-9}$ H to $1 \cdot 10^{-10}$ H. Moreover, σ_{L_q} decreases from $3 \cdot 10^{-6}$ H to $1 \cdot 10^{-7}$ H between 2000 rad/s $\leq \omega \leq$ 2200 rad/s.

greater estimation changes at medium tier operating speeds and the introduction of σ_{L_q} recalibration during high-speeds reduces the maximum torque estimation error. The design can be further fine tuned by adjusting operating ranges, the number of interpolation points and start and end values. The process was, however, delicate because of how the noise covariance settings for one state can affect the other states and the need to balance improving the rotor temperature estimation at the detriment of the torque estimation. The efficacy of utilizing an interpolating design is questionable and is largely dependent on how efficiently it can be implemented because the difference compared with only using two sets of calibrations was small.

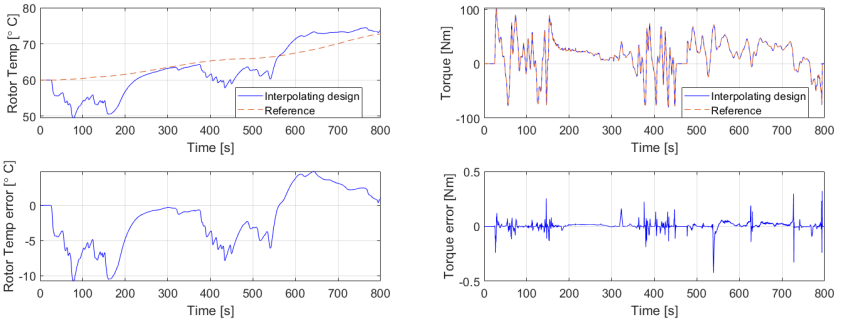

(a) Rotor temperature estimation.

(b) Torque estimation.

Figure 7.3: Rotor temperature and torque estimation results using the interpolating high-speed Q calibration that also introduces σ_{L_q} alterations.

Dynamic Test Cycle with Additional Noise

The performance was also evaluated using the WLTC high-speed test run segment with additional noise introduced in the Motor-CAD reference signal generation, identical to the simulation tests in Section 5.6. A gain on R, k_R, was once again applied to increase the weight of the model reliance. The estimation error with different k_R can be found in Figure 7.4 for the flux linkage estimation. The rotor temperature estimation error results are in Figure 7.5 and correspondingly for the torque estimation in Figure 7.6. It is also important to acknowledge that the flux linkage reference signal also was noisy and the flux linkage estimation error results are therefore not as conclusive as the other results.

Increasing k_R, reduced the noisiness of the flux linkage estimation. The large flux linkage estimation spikes were also generally reduced with increasing k_R, which can be seen in Figure 7.4. The large $\hat{\lambda}$ spikes resulted in larger maximum rotor temperature estimation errors when k_R was low but the torque estimation did still perform well overall. The simulation results from using a large k_R, have a generally lower maximum rotor temperature error but the designs did not perform well during the section the high-speed Q calibration was in use. The best overall results were obtained when $k_R = 10$ and $\hat{\lambda}$ still was relatively noisy, but the high-speed Q calibration still works reasonably well. Unlike the previous KF design, increasing k_R to deal with a noisier input signal was not enough and the high-speed Q calibration had to be tuned specifically for each choice of k_R.

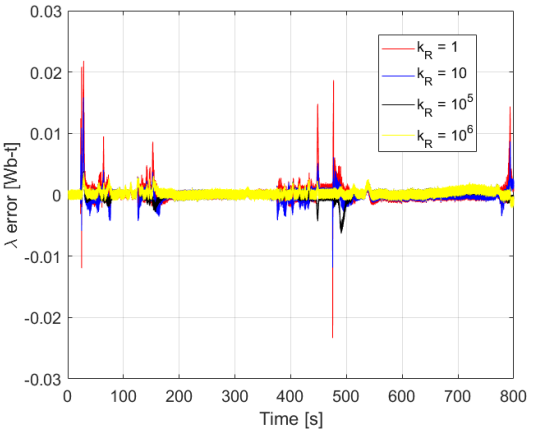

Figure 7.4: The flux linkage estimation error for a noisy WLTC test cycle. The flux linkage estimation noisiness and spikes were greatly reduced when the R gain, k_R, increased.

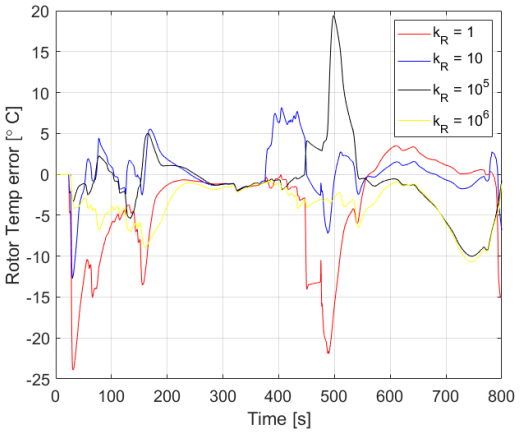

Figure 7.5: The rotor temperature estimation error for a noisy WLTC test cycle. The performance varied widely but the best results were with only a smaller R gain, $k_R = 10$. The worst performance when using a large k_R occurred when the high-speed Q calibration was active and a specific tuning for every k_R was required.

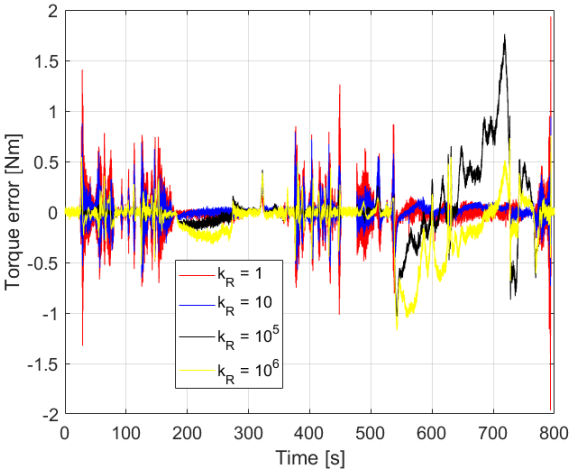

Figure 7.6: The torque estimation error for a noisy WLTC test cycle. The performance generally degraded with increasing R gain. The worst performance when using a large k_R occurred when the high-speed Q calibration was active and a specific tuning for every k_R was required.

Inverted Inductance States

The inverted inductance design was also tested with the same default Q and R settings as in Section 6.2, (6.17), and the same alteration to σ_λ as previously:

$$\sigma_\lambda = 1.8 \cdot 10^{-4}\,\text{Wb-t} \tag{7.3}$$

For the high-speed Q recalibration, the λ and L_{di} states were suppressed when $\omega \geq 1500$ rad/s with the following changes:

$$\sigma_\lambda = 1 \cdot 10^{-8}\,\text{Wb-t} \quad \sigma_{L_{di}} = 1 \cdot 10^{-2}\,\text{H}^{-1} \tag{7.4}$$

A comparison between using no high-speed Q calibration and with high-speed σ_λ and $\sigma_{L_{di}}$ alterations can be seen for the rotor temperature estimation in Figure 7.7. The improvement of using the high-speed recalibration was substantial and when comparing the results to the standard inductance state design in Figure 7.1, it can also be seen that the rotor temperature estimation error diverged positively as opposed to negatively during the high-speed segments.

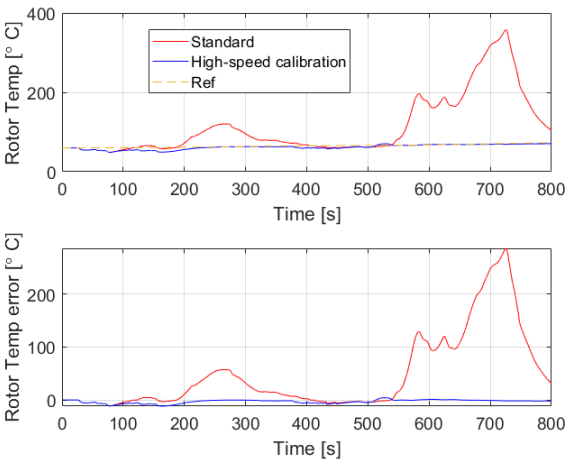

Figure 7.7: Rotor temperature estimation results with and without the high-speed Q calibration for the inverted inductance design. Without altering Q at higher speeds the rotor temperature estimation error became very large.

To alleviate issues that arise when the discrepancy in Q settings was too large after the high-speed recalibration, another design was tested where $\sigma_{L_{qi}}$ also was altered when $\omega \geq 1600$ rad/s, as follows:

$$\sigma_{L_{qi}} = 1\,\text{H}^{-1} \tag{7.5}$$

The inductance estimation results comparing the introduction of $\sigma_{L_{qi}}$ to the high-speed recalibration can be found in Figure 7.8 and the resulting torque estimation and error in Figure 7.9. After introducing changes to $\sigma_{L_{qi}}$ during high-speed operating ranges, the L_{qi} estimation spikes reduced drastically which consequently also improved the torque estimation.

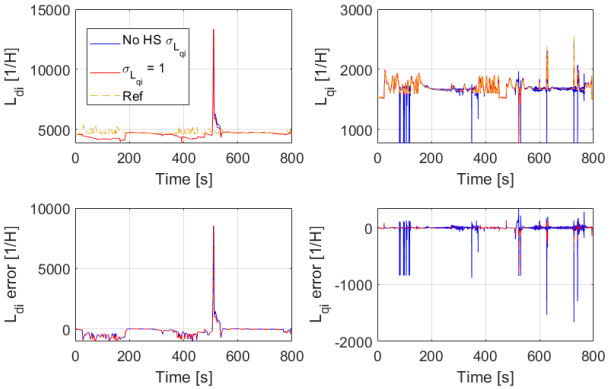

Figure 7.8: Inductance estimation results with and without a high-speed Q calibration of $\sigma_{L_{qi}}$ for the inverted inductance design. The L_{qi} estimation performed reasonably well during high speeds, but the high-speed Q recalibration to improve the λ and L_{di} estimations subsequently caused issues for the L_{qi} estimation when $\sigma_{L_{qi}}$ was too large comparatively, and reducing $\sigma_{L_{qi}}$ to 1 H^{-1} during the high-speed calibration improved the L_{qi} estimation.

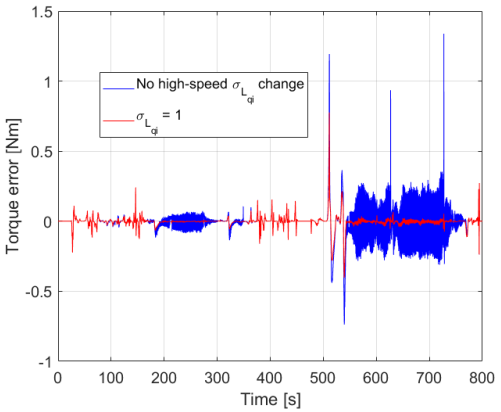

Figure 7.9: Torque estimation results with and without a high-speed Q calibration of $\sigma_{L_{qi}}$ for the inverted inductance design.

Interpolating Design, Inverted Inductances

An interpolating design was also tested that increased the estimation suppression linearly with increasing ω when $1500 \leq \omega \leq 2200$ rad/s. The SD of the process noise as a function ω in addition to the R gain k_R is shown for the interpolating design in Figure 7.10.

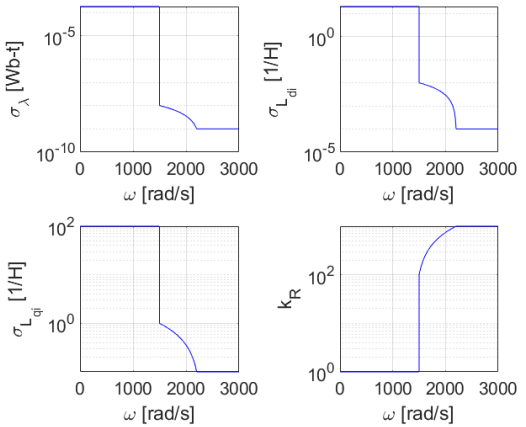

Figure 7.10: The SD of the process noise as a function of ω for the inverted inductance high-speed interpolating design. Between 1500 rad/s $\leq \omega \leq$ 2200 rad/s, σ_λ linearly decreases from $1 \cdot 10^{-8}$ Wb-t to $1 \cdot 10^{-9}$ Wb-t, $\sigma_{L_{di}}$ goes from $1 \cdot 10^{-2}$ H^{-1} to $1 \cdot 10^{-4}$ H^{-1} and $\sigma_{L_{qi}}$ from 1 H^{-1} to 0.1 H^{-1}. In addition to the changes to Q, a R gain k_R was also introduced between $1500 \leq \omega \leq 2200$ rad/s that increases from 10^2 to 10^3.

The rotor temperature and torque estimation results can be found in Figure 7.11. Comparing the results to the interpolating standard inductance state design in Figure 7.3, shows that there was no clear improvement compared to using the inverted inductance state design. Fine tuning of Q and R and the high-speed recalibration of the noise covariance matrices have a large impact on the performance, but utilizing the inverted inductance design requires a relatively greater amount of high-speed estimation suppression for a similar performance. The analysis of the observability Gramian in Section 6.4 also showed that $\kappa(\mathcal{O}_x)$ for the discrete-time system was larger for the inverted inductance design. A more deliberate rescaling effort with scaling factors appears to be a more promising avenue and the standard inductance state design was instead the focus for the remainder of the simulation study.

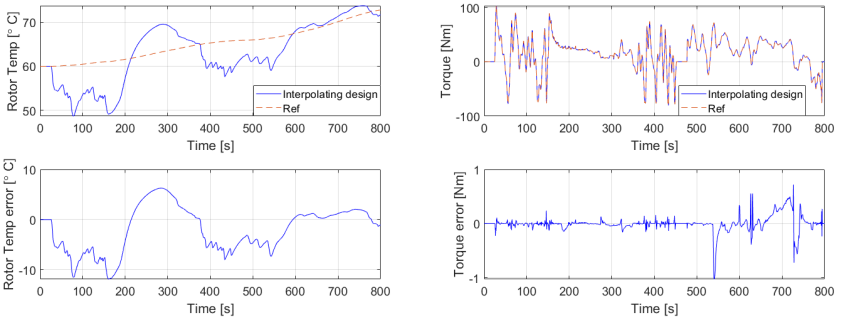

(a) Rotor temperature estimation.

(b) Torque estimation.

Figure 7.11: Rotor temperature and torque estimation results using the interpolating high-speed Q calibration with a R gain k_R for the inverted inductance design. The overall estimation suppression with high-speed noise covariance recalibration was relatively large when using the inverted inductance design for a slightly worse performance compared to the standard inductance design.

7.2 Near Standstill Estimator

To evaluate the near standstill estimator, which activates when the speed is close to zero, the standard inductance design with interpolating high-speed Q adjustments was employed for a NEDC test cycle. In the dynamic-T_c KF in Algorithm 4, the low-speed estimator activated when the observability was low and the observer gains for the flux linkage estimation spiked. From the analysis of the observability Gramian in Section 6.4, the low-observability estimator was instead chosen to activate near standstill and through tuning from simulation tests, the speed threshold was chosen to be:

$$|\omega_{threshold}| = 2.6\,\text{rad/s} \tag{7.6}$$

The simulation results, however, surprisingly showed that the L_q estimation performed much better than the L_d estimation. Using the same strategy as the dynamic-T_c KF during the low-observability estimator by: stopping the update of the estimation error covariance matrix P, keeping the old inductance values and only updating the flux linkage estimation with the model (the near standstill estimator in Algorithm 5) instead caused issues for the L_q estimation. A design was also evaluated, where the P matrix update is perpetually active and the L_q estimation is unimpeded, showed in Algorithm 6. In the alternative near standstill estimator, the old L_d estimation is, however, still retained and the λ estimation slowly converges towards the coolant temperature.

Algorithm 6 Near standstill estimator with unimpeded L_q estimation.

Near standstill estimator

$L_d^{old} = \hat{x}_{k-1}(5)$
$\varepsilon_k = y_k - H_k \hat{x}_{k|k-1}$
$S_k = H_k P_{k|k-1} H_k^T + R_k$
$K_k = P_{k|k-1} H_k^T S_k^{-1}$
$P_{k|k} = (I_k - K_k H_k) P_{k|k-1}$
$K_k(3,:) = 0$
$\hat{x}_{k|k} = \hat{x}_{k-1|k-1} + K_k \varepsilon_k$
$\hat{x}_{k+1|k} = f(\hat{x}_{k|k}, u_k)$
$P_{k+1|k} = F_k P_{k|k} F_k^T + Q_k$
$\hat{x}_{k+1}(5) = L_d^{old}$

Simulation Comparison

The flux linkage estimation comparing no estimator switch and the two near standstill estimator designs can be found in Figure 7.12. The low-observability estimator that does not update the P matrix near standstill yields the best λ and L_d estimation results, which according to the sensitivity analysis in Section 5.8 were very important to the rotor temperature estimation. The design with unimpeded L_q estimation had pronounced flux linkage estimation spikes that also could occur for the design with no low-obsersvability estimator. The rotor temperature and torque estimation error for the designs can be found in Figure 7.13. The design that suspended the P matrix update, improved the rotor temperature estimation considerably but at the detriment of the torque estimation. The design that left the L_q estimation unimpeded did, however, retained the rotor temperature estimation improvements without compromising the torque estimation. A potential issue for the low-observability estimator with unimpeded L_q estimation emerged during long cool-down periods, where the L_q estimation slowly drifted towards the lower saturation limit. To avoid a large initial settings error after long cool down periods, the L_q estimation had to be reset to the initial conditions if the motor remains inactive for a certain time period.

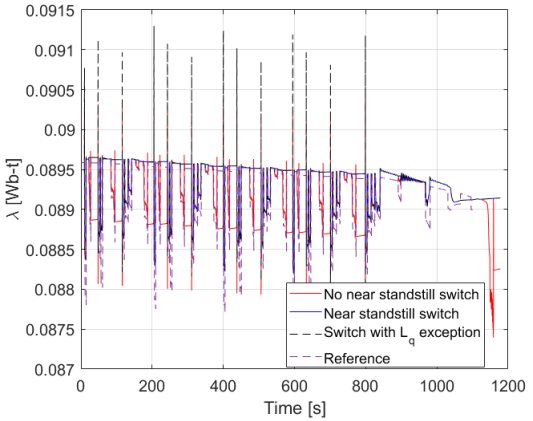

Figure 7.12: Flux linkage estimation comparing no low-observability estimator and two near standstill estimator designs. The near standstill estimator that suspends the P matrix update and retains the old inductance values from before the switch yields the best flux linkage estimation results. The near standstill estimator design that allows the L_q estimation to continue has large flux linkage estimation spikes.

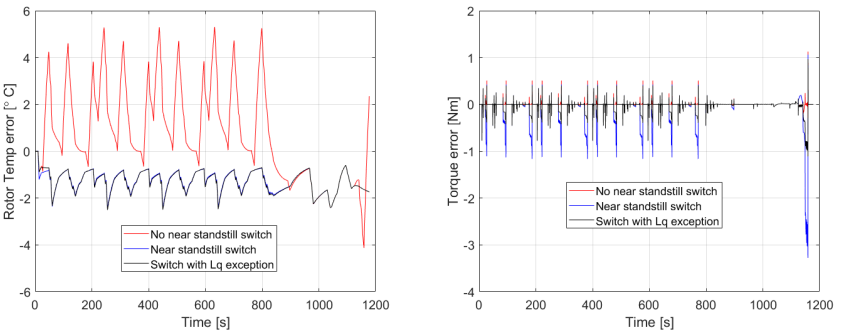

(a) Rotor temperature estimation error.

(b) Torque estimation error.

Figure 7.13: Rotor temperature and torque estimation error comparing no low-observability estimator and two near standstill estimator designs. The LP-filter with comparatively long time constant, used to smooth out the λ_{m0} working point changes for the rotor temperature estimation, also helped with the flux linkage estimation spikes that can occur for both the unimpeded L_q estimator design and the design without a low-observability estimator switch. The design that left the L_q estimation unimpeded retains the rotor temperature estimation improvements from a low-observability estimator switch without compromising the torque estimation.

7.3 Rotor Temperature Estimation Tuning

Compared to the previous KF designs, the EKF had problems accurately following the flux linkage fluctuations that occurred with torque variations. The sensitivity analysis in Section 5.8 showed that accurate L_d values were very important for the flux linkage estimation performance and the EKF L_d estimation has to be largely suppressed to avoid the λ estimation to greatly diverge. The rotor temperature was calculated with (2.10) and used the λ_{m0} reference point that is obtained from a LUT with torque and speed inputs. To address the unresponsive flux linkage estimation during torque variations because of the poor L_d estimation, the λ_{m0} reference point was instead obtained by limiting the rate of change for the torque input to the LUT. A comparison between the standard λ_{m0} LUT results and with a torque input rate limit can be found in Figure 7.14 for a NEDC test cycle.

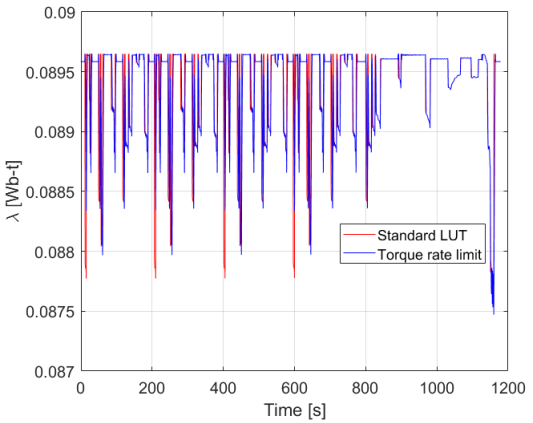

Figure 7.14: The λ_{m0} LUT reference point results with and without a torque input rate limit. The λ_{m0} fluctuations were reduced with the LUT adjustments.

The L_1-norm of the average error for the rotor temperature estimation for different rate-limit magnitudes can be found in Figure 7.15. The torque input rate-limit magnitude that gave the best results was 14 Nm/s and a plot of the rotor temperature estimation results along with the results without a torque input rate limit is shown in Figure 7.16. The same LP time constant of 30 s was used as in the previous KF designs to smooth out the λ_{m0} working point changes. Without a torque input rate limit, the average L_1 estimation error of the rotor temperature was $\|\tilde{T}_r\|_1 = 1.2847$ and with a rate limit of 14 Nm/s it noticeably improved to $\|\tilde{T}_r\|_1 = 0.8792$.

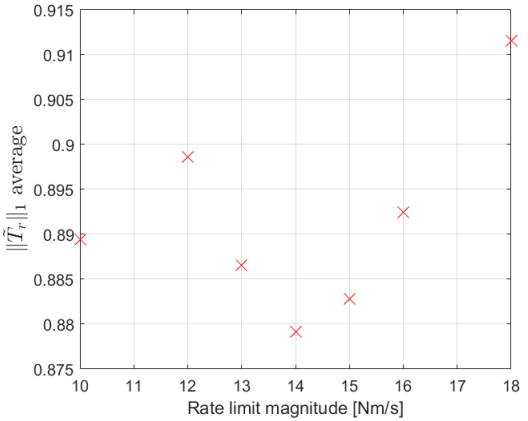

Figure 7.15: The L_1-norm of the average rotor temperature estimation error for different torque input rate limit magnitudes. For comparison, $\|\tilde{T}_r\|_1 = 1.2847$ without a rate limiter.

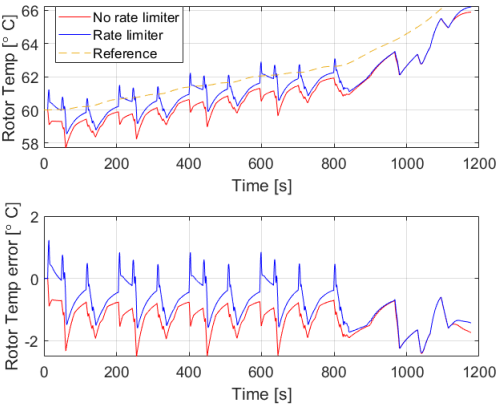

Figure 7.16: Rotor temperature estimation results with and without a torque input rate limiter. The results were from a rate-limit magnitude of 14 Nm/s and show a noticeable improvement.

7.4 Initial Condition Analysis

The initial condition settings have been very accurate thus far with: the correct starting coolant temperature T_c and a λ value that corresponds to the coolant temperature, currents starting from zero and inductance values that are obtained from a LUT

with torque and rotor speed inputs equal to zero. To test the EKF performance with imperfect initial conditions, the starting values for each state was increased twofold. Since the current starting values were set to zero, they were instead chosen to start from 50 A, a value in the lower operating range. A table summarizing the average error magnitude for incorrect initial conditions for the respective states can be found in Table 7.1.

Table 7.1: The average estimation error with erroneous initial conditions. The starting value was increased twofold, but because the current starting values were 0 A, they were instead set to 50 A.

L_1-norm average error with incorrect initial conditions for the respective states.			
State with erroneous initial condition	$\|\tilde{\lambda}\|_1$ average [mWb-turns]	$\|\tilde{T}_r\|_1$ average [°C]	$\|\tilde{\tau}\|_1$ average [Nm]
Standard	0.16326	0.8792	0.0382
I_d	0.16326	0.8792	0.0382
I_q	0.16328	0.8796	0.0382
λ	0.92777	10.89	0.0383
T_c	0.16326	0.8792	0.0382
L_d	0.16367	0.8771	0.0382
L_q	0.16325	0.8795	0.0382

The results show that the flux linkage initial condition was the most sensitive setting but the torque estimation still performed well. The flux linkage to rotor temperature conversion is, however, particularly sensitive and a twofold increase results in a large rotor temperature error which can be seen in Figure 7.17, which includes the T_r and λ estimation error with a twofold increase of the λ initial condition. The LP-filter introduced in the rotor temperature estimation to smooth out the λ_{m0} working point changes further prolongs the time before the error was corrected. The rotor temperature estimation error was also exacerbated by the low-observability estimator, which only slowly converges to the flux linkage value corresponding to the coolant temperature and is not well suited to correct poor initial flux linkage settings. The EKF does, however, quickly correct the flux linkage estimate once it was active, which can be seen in Figure 7.17, where it switched to the regular EKF at around 10 seconds. The low-observability estimator caused similar issues for the L_d estimate, because it holds onto the old inductance value. The flux linkage estimation does, however, not make use of the inductances during the low-observability estimator and the torque estimation was not greatly affected either due to the small currents when the low-observability estimator was active. The L_d initial condition error's effect on the performance was therefore not as detrimental, evident by the results in Table 7.1. In spite of the fact that the discrete-time system is unstable for most rotor speeds, the state estimates rebounded quickly with the chosen default Q and R noise covariance matrix settings. If there are concerns that the λ initial condition is poorly calibrated, there is also a possibility of introducing a settling time

for the rotor temperature estimate based on the LP-filter time constant and when the standard EKF is first activated.

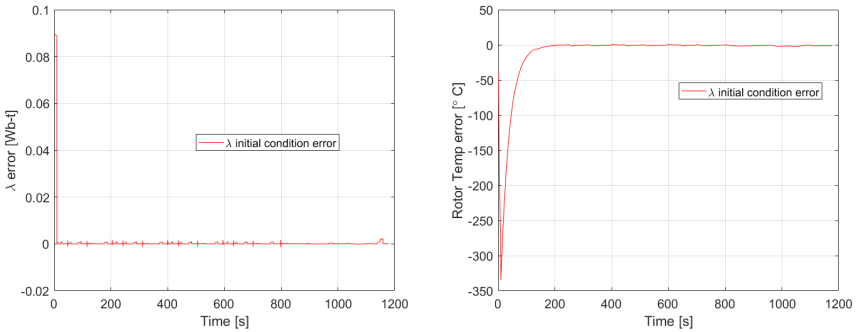

(a) Flux linkage estimation error.

(b) Rotor temperature estimation error.

Figure 7.17: Flux linkage estimation and rotor temperature error with a twofold increase of the λ initial condition. In the first 10 seconds of the NEDC test cycle, the low-observability estimator was active and the λ estimate quickly recovers after the standard EKF activates. The rotor temperature estimation error takes longer to recover because of the LP-filter introduced in the rotor temperature estimation to smooth out λ_{m0} working point changes.

Inductance Saturation

The inductance saturation is not a relevant concern when the observer is well calibrated, but with very poor initial conditions the estimated inductance can cross zero and cause estimation singularities. The consequences of poor calibrations can be greatly mitigated. To illustrate the effects, the rotor temperature and torque estimation error with and without inductance saturation is shown in Figure 7.18 for an initial condition error of 200 A for I_q. The inductance estimation results from the tests can also be found in Figure 7.19. A starting value of 200 A is extremely inaccurate, but the effects were substantially minimized after saturating the inductances but both designs eventually recovered.

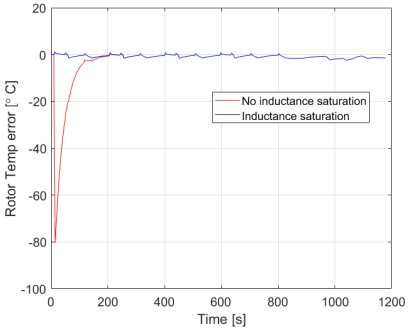

(a) Rotor temperature estimation error.

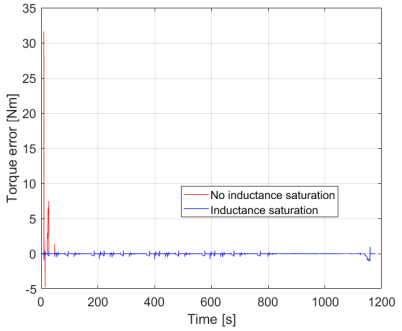

(b) Torque estimation error.

Figure 7.18: Rotor temperature and torque estimation error with an initial condition error of 200 A for I_q. The effects were greatly minimized when saturating the inductances.

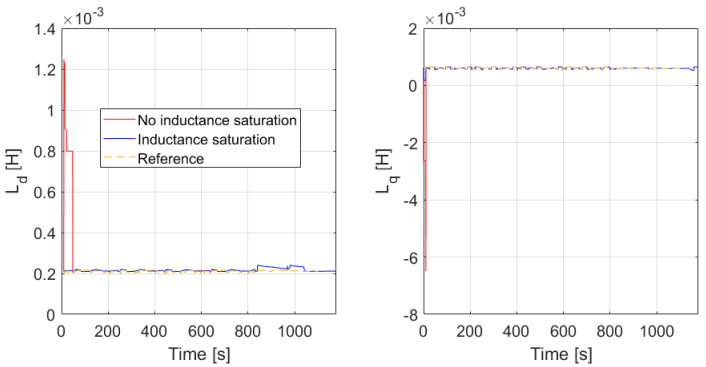

Figure 7.19: Inductance estimation with an initial condition error of 200 A for I_q. By saturating the inductances and never letting the estimations cross zero, the effect was greatly minimized.

7.5 Sample Rate Analysis

The EKF performance was evaluated for different sampling frequencies, which, opposed to the KF designs, also affected the operating speed range for which the system was unstable. The flux linkage estimation results for varying sampling frequencies using a NEDC test cycle are shown in Figure 7.20 and the rotor temperature and torque estimation errors in Figure 7.21. A table composed of the L_1-norm average estimation errors is displayed in Table 7.2. The results were not as straightforward as the KF simulation tests, but the torque estimation performance did generally improve with higher sampling frequencies. Lower sampling rates resulted in

an unstable system for a larger portion of the operating range and an overall more dynamic flux linkage estimation. That a lower sampling frequency had an improved estimation result, is a sign that indicates that the default process noise σ_λ setting for the faster sampling rates was slightly too small and suppressive for low to medium operating speeds. The faster sampling rates did, however, perform better during the latter portion of the NEDC test cycle, when the rotor speeds were highest, and also have a generally lower maximum rotor temperature estimation error. The rotor temperature estimation results were also affected by the torque input rate limit tuning for the λ_{m0} LUT reference point. A more appropriate comparison between different sampling frequencies each require a specific tuning of: the Q and R matrices, the high-speed noise covariance matrix recalibrations and a torque input rate-limit magnitude to match. Unless the sampling rate is high enough to greatly increase the stable ω operating region, the expected improvements for increasing the sampling rate was overshadowed by the incorrect Q, R and torque input-rate limit tuning.

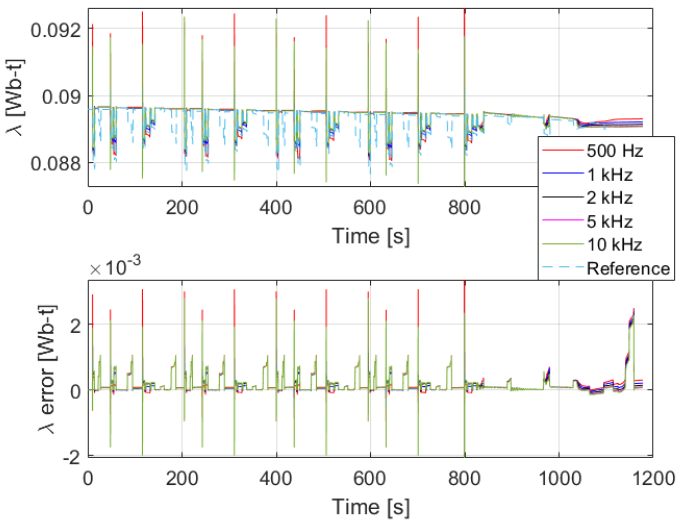

Figure 7.20: Flux linkage estimation results of a NEDC test cycle using different sampling frequencies. A lower sampling frequency increases the unstable λ operating region and gives a more dynamic flux linkage estimation result.

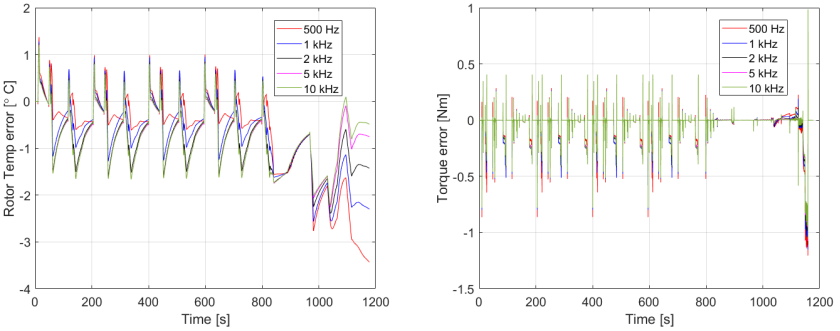

(a) Rotor temperature estimation error.

(b) Torque estimation error.

Figure 7.21: Rotor temperature and torque estimation error of a NEDC test cycle using different sampling frequencies. The torque estimation generally improves with increased sampling frequency. The rotor temperature results are also dependent on the torque input rate-limit magnitude tuning.

Table 7.2: The average estimation errors for a NEDC test cycle using different sampling frequencies.

L_1-norm average error for various sampling frequencies.			
Sampling frequency [kHz]	$\|\tilde{\lambda}\|_1$ average [mWb-turns]	$\|\tilde{T}_r\|_1$ average [°C]	$\|\tilde{\tau}\|_1$ average [Nm]
0.5	0.16372	0.8236	0.0421
1	0.15826	0.8402	0.0429
2	0.16326	0.8792	0.0382
5	0.16327	0.8413	0.0356
10	0.16280	0.8147	0.0358

7.6 Simulation Analysis with Rescaled State Variables

Even though the Matlab simulation environment has very high numerical precision, a lack of hardware precision can cause issues when implementing the design. In Section 6.6, state variables were rescaled to reduce the observability Gramian condition number and simulation tests were done with the following scaling factors:

$$k_L = 500 \quad k_\lambda = 10 \tag{7.7}$$

The default Q and high-speed noise covariance matrix settings have to be tuned specifically for each combination of scaling factors and with the chosen scaling factors, the default process noise covariance matrix Q was altered as follows:

$$\sigma_\lambda = 7 \cdot 10^{-4}\,\text{Wb-t} \quad \sigma_{L_d} = \sigma_{L_q} = 1 \cdot 10^{-3}\,\text{H} \tag{7.8}$$

and the high-speed recalibration was implemented at three discrete points with the following changes active between 1500 rad/s $\leq \omega \leq$ 2000 rad/s :

$$k_R = 10 \quad \sigma_\lambda = 1 \cdot 10^{-5}\,\text{Wb-t} \quad \sigma_{L_d} = 1 \cdot 10^{-5}\,\text{H} \quad \sigma_{L_q} = 4 \cdot 10^{-4}\,\text{H} \tag{7.9}$$

where k_R is the gain on R. Between 2000 rad/s $\leq \omega \leq$ 3000 rad/s further alterations were made with:

$$k_R = 30 \quad \sigma_\lambda = 2 \cdot 10^{-6}\,\text{Wb-t} \quad \sigma_{L_d} = 3 \cdot 10^{-6}\,\text{H} \quad \sigma_{L_q} = 2 \cdot 10^{-4}\,\text{H} \tag{7.10}$$

and at $\omega \geq$ 3000 rad/s with:

$$k_R = 40 \quad \sigma_\lambda = 9 \cdot 10^{-7}\,\text{Wb-t} \quad \sigma_{L_d} = 1 \cdot 10^{-6}\,\text{H} \quad \sigma_{L_q} = 1 \cdot 10^{-4}\,\text{H} \tag{7.11}$$

The tested combination of scaling factors that gave the best reduction of the condition number in Section 6.6, were instead with k_λ = 1. The EKF observability analysis was, however, limited to a maximum electrical angular speed of ω = 3000 rad/s and simulation tests were problematic during operating speeds over 3000 rad/s. Increasing the flux linkage and inductance state magnitude with a scaling factor allows for state estimation with greatly increased Q settings. With k_λ = 1 the large discrepancy in high-speed settings for λ and the inductances for operating ranges over 3000 rad/s were hard to calibrate without a large k_R. A large k_R greatly reduced the estimation convergence for all states and impairs the L_q estimation, leading to poor torque estimation results.

Simulation results with the aforementioned settings can be seen in Figure 7.22 for the flux linkage estimation. The rotor temperature and torque estimation results are shown in Figure 7.23, where the torque input rate limit for the λ_{m0} LUT was slightly reduced to 12 Nm/s for the PM temperature calculations. The average error magnitude for the respective signals were: $\|\tilde{\lambda}\|_1$ = 0.1536 mWb-turns, $\|\tilde{T}_r\|_1$ = 1.313 °C and $\|\tilde{\tau}\|_1$ = 0.0082 Nm.

The simulation test with rescaled λ and inductance state magnitudes gave improved torque estimation, but degraded the rotor temperature estimation. It is, however, hard to directly compare the different designs because each design has specific default Q and high-speed noise covariance matrix settings. It is possible to find a combination of scaling factors with a specific tuning that can improve both the rotor temperatue and torque estimation but fine tuning the noise covariance matrix settings for each operating region of ω is very delicate, time consuming and has to be redone for every choice of scaling factors. The estimator performed well if it was properly calibrated but there are concerns regarding the robustness of the estimator under slightly different operating conditions, when experiencing unforeseen disturbances. Using scaling factors for λ and the inductances, greatly increased the σ settings for Q, which otherwise were extremely small for the unscaled designs, and reduce the required numerical precision of the hardware. Increased hardware intensive approaches are, however, most likely unavoidable to increase the robustness of the estimator, either by using a sampling frequency that is stable for the entire ω operating region or with a more hardware demanding discretization technique, such as the backward Euler method discussed in Section 6.1.

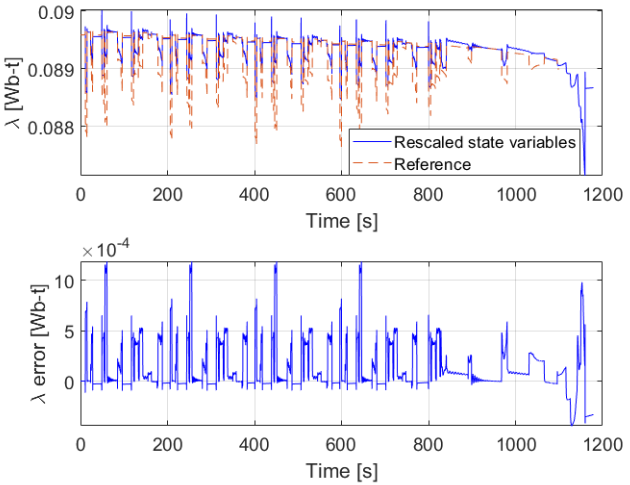

Figure 7.22: Flux linkage estimation results for a rescaled state variable system using $k_L = 500$ and $k_\lambda = 10$. The Q settings were greatly increased compared to the unscaled state variable designs.

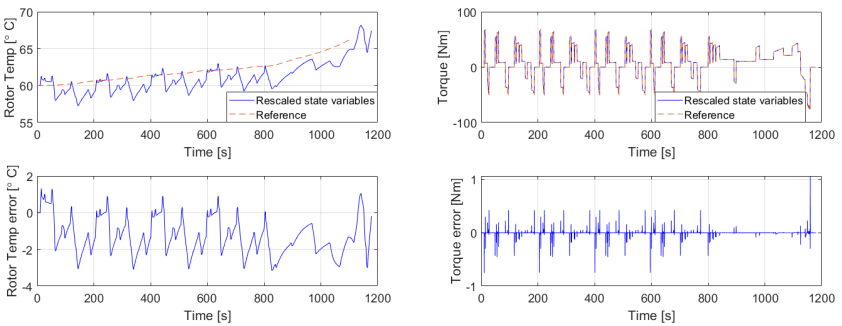

(a) Rotor temperature estimation.

(b) Torque estimation.

Figure 7.23: Rotor temperature and torque estimation results for a rescaled state variable system using $k_L = 500$ and $k_\lambda = 10$. With the Q and R settings used, the torque estimation was greatly improved at a slight cost of the rotor temperature estimation performance.

7.7 EKF Comparison with KF with Constant Inductances

To assess how the EKF design performs in comparison to the KF with limited inductance accuracy, simulation tests were conducted on the normalized system KF,

found in Section 5.10, with constant inductances and the standard inductance interpolating EKF design, found in Section 7.1, with the near standstill estimator in Algorithm 6. The two designs were chosen because they both gave the best overall estimation results, but the vast improvement in computational robustness of the normalized system KF over the EKF designs also has to be taken into consideration. The PM temperature estimation results using the NEDC test cycle, comparing the KF with constant inductances and the EKF design is shown in Figure 7.24 and the torque estimation results in Figure 7.25. The constant and estimated inductances are also showed in Figure 7.26.

The rotor temperature estimation during low to medium speeds was comparable, but the difference during high speeds was pronounced, where the KF could reach a maximum temperature-estimation error magnitude of around 10 °C while the EKF never exceeded 2.5 °C. It was also during the high-speed segment that the differences between inductances were the largest and most prolonged, resulting in the largest difference of the slowly changing rotor temperature estimate. The EKF torque estimation, conversely, consistently outperformed the KF across the simulation test. If the hardware running the observers can manage the increased computational uncertainty of the EKF designs, it can be a valid alternative to the KF designs when knowledge of the inductances is poor.

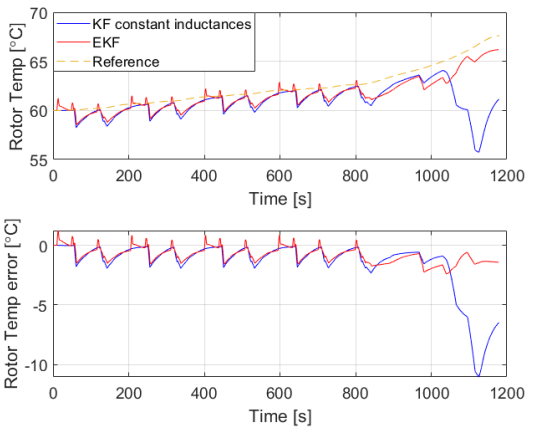

Figure 7.24: Rotor temperature estimation results for the normalized system KF with constant inductances and the standard inductance, high-speed interpolation EKF design. The average T_r error magnitude for the KF was $\|\tilde{T}_r\|_1 = 1.51$ °C and $\|\tilde{T}_r\|_1 = 0.879$ °C for the EKF. The EKF design showed great improvement over the KF design during the high-speed segments of the NEDC test cycle.

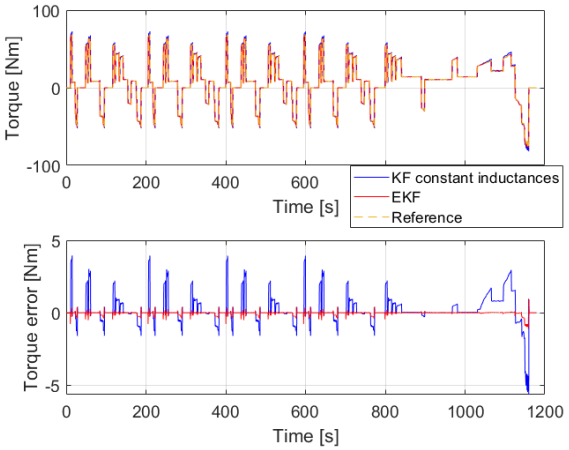

Figure 7.25: Torque estimation results for the normalized system KF with constant inductances and the standard inductance, high-speed interpolation EKF design. The average τ error magnitude for the KF was $\|\tilde{\tau}\|_1 = 0.473$ Nm and for the EKF it was $\|\tilde{\tau}\|_1 = 0.038$ Nm. The EKF design consistently outperformed the KF design across the NEDC test cycle.

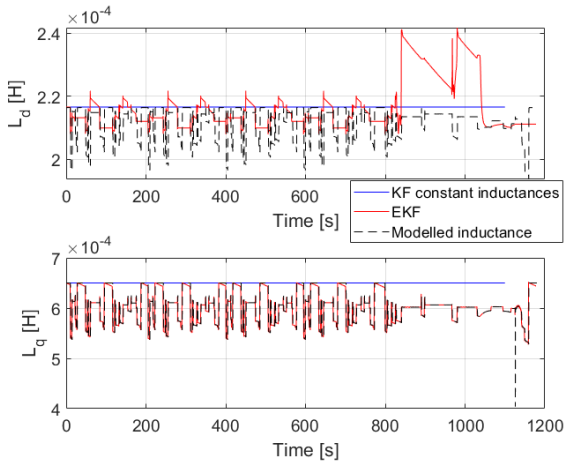

Figure 7.26: The constant inductances used for the normalized system KF and the estimated inductances of the standard inductance, high-speed interpolation EKF design. The largest and most prolonged difference occurred during the high-speed segment. It is also possible to see how much better the L_q estimation performed and why a smaller σ_{L_d} was necessary.

8

Measurement Data Study

The focus of the analysis in this thesis has been on simulation results using a detailed motor model, but to briefly conclude the analysis, estimation results and analysis from real measurement data are also presented. The measurements were conducted on a different e-machine than the one used in the simulation analysis and the previous observer tuning was consequently not applicable. The measurement analysis was conducted with the normalized system direct-T_c KF, which was the lowest order KF and the easiest to calibrate because of the lowest number of tuning variables and a simpler low-speed switch logic. The normalized system KF in the simulation analysis in Section 5.10, allowed for tuning that placed a greater reliability on the measurement signal, improved numerical robustness and was also implemented for the different motor.

8.1 Setup

Experimental Setup

The evaluation data used in the analysis presented this section was collected from rig tests performed with a Borg-Warner e-machine, which had been equipped with thermocouples in the rotor shaft, close to the magnets. Motor currents, voltage references and speed were collected in addition to the measured rotor temperature. The e-machine was connected to a break dynamometer which allowed for dynamic test-cycle testing. To collect data from scenarios that would be realistic in a vehicle, a NEDC, and a city-driving cycle (CDC) were executed. During the cycles, the e-machine coolant was controlled to 50 °C, and a cool-down period was also measured after each cycle, in order to capture the cool-down characteristics.

Model Setup

The parameters for the motor come from LUTs that were working point dependent and they have been optimized with measurement data using system identification techniques, provided by BorgWarner. The measurement data was collected from a

NEDC test cycle, which can be seen in Figure 8.1, and it was slightly different from the test cycle in the simulation analysis. The observer was also tested on a City Driving Cycle (CDC), part of the Worldwide harmonized Light vehicle Test Cycles (WLTC), which can be seen in Figure 8.2.

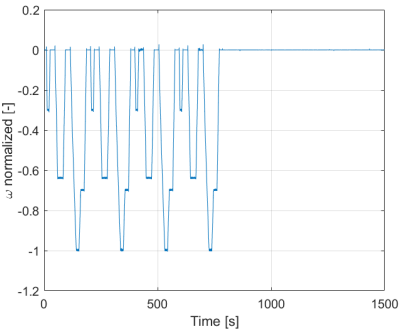

(a) NEDC electrical angular speed ω.

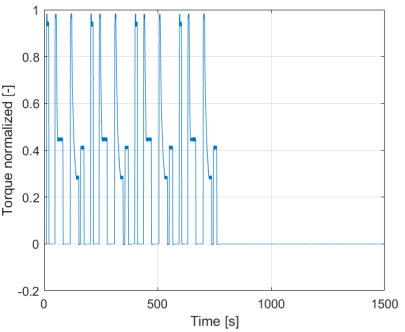

(b) NEDC torque.

Figure 8.1: The normalized ω and torque of a NEDC cycle over time.

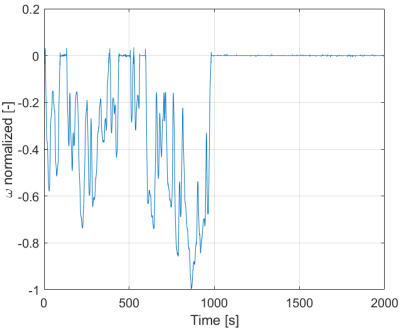

(a) CDC electrical angular speed ω.

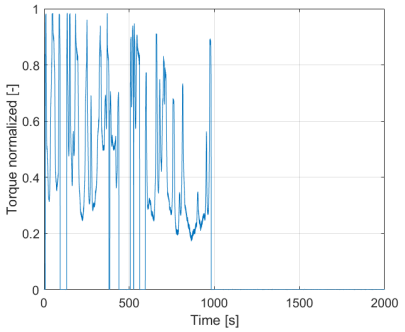

(b) CDC torque.

Figure 8.2: The normalized ω and torque of a CDC cycle over time.

The estimation results from the normalized system direct-T_c KF used a 2 kHz sampling frequency and had the following noise covariance matrix Q settings:

$$\sigma_{I_d} = 10\,\text{A} \quad \sigma_{I_q} = 3\,\text{A} \quad \sigma_{\lambda} = 3.5 \cdot 10^{-3}\,\text{Wb-t} \tag{8.1}$$

and the following R settings with a R gain, k_R:

$$\sigma_{I_d} = 1\,\text{A} \quad \sigma_{I_q} = 1\,\text{A} \quad k_R = 5.5 \tag{8.2}$$

The low-observability estimator threshold was chosen as $\omega_{threshold}$ = 420 rad/s, the PM temperature time constant as τ_m = 1300 s and the LP-filter to smooth the working point λ_{m0} changes for the rotor temperature estimation had a time constant of 120 s.

8.2 Results

The estimation results from the normalized system, direct-T_c KF with real measurement data are shown in Figure 8.3 for the flux linkage estimation of the NEDC test cycle and in Figure 8.5 for the CDC cycle. There was no flux linkage measurement, but the reference signal in the estimation results was the corresponding flux linkage value converted from the rotor temperature measurement and operating point with (2.10). The rotor temperature estimation and measurement for the NEDC test cycle are found in Figure 8.4 and in Figure 8.6 for the CDC test cycle.

The KF design tuning for the motor in the simulation analysis was much more thorough, but the estimation results from the measurement data still performed decently, with a maximum PM temperature estimation error magnitude within $\pm$ 7 °C for the NEDC test cycle. The observer performed slightly worse for the CDC test cycle with a maximum PM temperature estimation error magnitude within $\pm$ 12 °C. The largest deviation of the PM temperature estimate occurred for the CDC test cycle around 500 s, where the motor strongly decelerates to standstill and the low-observability estimator continues to converge towards the lower coolant temperature value.

The λ estimate was, however, not the sole contributing error factor. Possible errors could also be the result of imperfect inductances, which affect the T_r estimation through the λ estimate. There was also some degree of measurement uncertainty, with deviations between the rotor temperature measurements from different sensors.

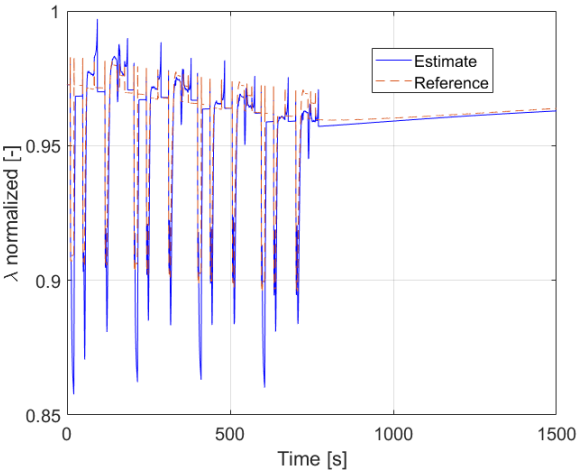

Figure 8.3: The normalized flux linkage estimation results using real measurement data for a NEDC test cycle. The reference signal is the corresponding flux linkage value converted from the rotor temperature measurement.

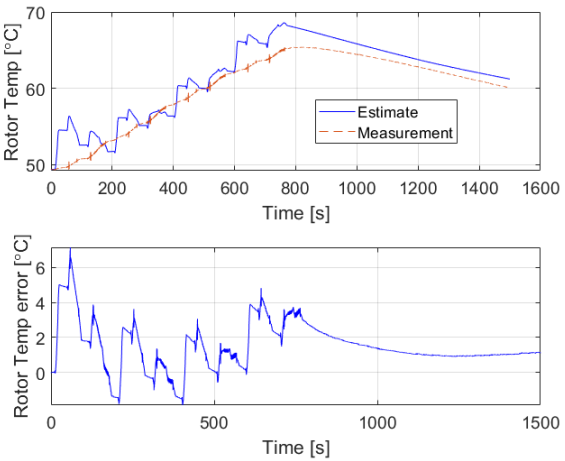

Figure 8.4: Rotor temperature estimate and measurement for a NEDC test cycle. The average PM temperature error magnitude was $\|\tilde{T}_r\|_1 = 1.66$ °C. The accuracy for different working points was more inconsistent for the PM temperature estimation than in the simulation analysis, resulting in larger PM temperature estimation fluctuations.

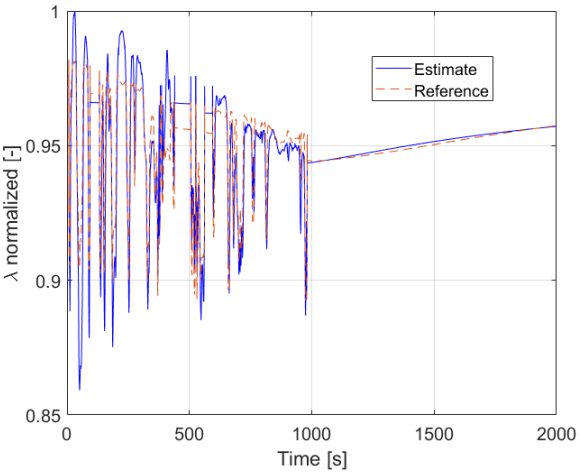

Figure 8.5: The normalized flux linkage estimation results using real measurement data for a CDC test cycle. The reference signal is the corresponding flux linkage value converted from the rotor temperature measurement.

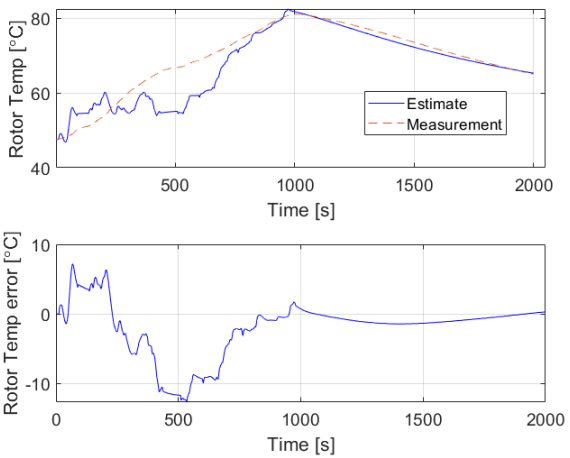

Figure 8.6: Rotor temperature estimate and measurement for a CDC test cycle. The average PM temperature error magnitude was $\|\tilde{T}_r\|_1 = 2.80$ °C.

9

Conclusion

9.1 Objectives in Problem Formulation

The objective of this thesis was to provide analysis of different observer-based approaches to rotor temperature and torque estimation with current and voltage measurements. The problem formulation identified some important consideration that required special attention. The parameter-varying characteristics of the motor model was an unavoidable facet in obtaining adequate estimation accuracy over the entire operating range. A sensitivity analysis of model parameters and input signals was conducted to give insight into the affects of parameter uncertainty, which later informed the decision to develop an EKF with inductance estimation.

Another key issue that was identified was observability problems at certain operating points and limited, non-persistent excitation. The observability of the system was thoroughly analyzed and low-observability estimators, which utilized the coolant temperature, was developed.

Another goal was to investigate possible relationships between the optimal observer gain and the operating speed. The observer gain analysis gave some idea of the behavior of the observer at low-speed operating ranges, but was quite limited. The most significant impact the relationship between the operating speed and the observer gain had during the development of observers was when utilizing gain scheduled noise covariance matrices for the EKF. The tuning could, however, vary a lot from other factors, such as sampling frequency and state variable rescaling.

The last topic identified during the problem formulation was computational and memory demand. Hardware resources was an important consideration during the observer development and analysis, with performance evaluations with different filter sampling frequencies, the analysis on numerical robustness and the design choices of the EKF with forward Euler discretization and gain scheduling. Potential memory issues could occur when managing large LUTs on an embedded system, but never appeared to be an issue and was not part of the analysis.

9.2 Summary

Both the extensive simulations and the more limited measurement analysis showed that an indirect observer-based approach to estimate the rotor temperature and torque from the currents and voltages has potential. The worst performance was for the motor used in the measurement analysis, with a rotor temperature error within $\pm$ 12 °C. It is, however, hard to judge if the error falls within an acceptable range, as the required error tolerance is very application specific. The torque error tolerance could range from only a few percentages to a much larger value depending on how easily torque inaccuracies can be compensated for externally. When calculating the currents to generate a desired torque value, the PM temperature, or flux linkage, can be utilized when attempting to solve for the currents that yield the Maximum Torque Per Ampere. The PM temperature or flux linkage can also be used to obtain the current torque estimate and the maximum/minimum available torque for an operating point. All the different uses can help improve motor regulation and have their own acceptable error tolerance. Using the PM temperature instead of the flux linkage estimate in a torque compensation schemes does, however, introduce possible errors from working points inaccuracies when converting the flux linkage into a corresponding rotor temperature. It was, however, difficult to ascertain the accuracy of the flux linkage estimate, as it was not included in the measurement analysis. The rotor temperature can also be utilized in the motor's cooling system and that has its own set of requirements.

Improper observer tuning was most likely not the only source of errors during the measurement analysis. Other possible contributing factors, include inductance inaccuracies and measurement uncertainty. Tuning the observers was, however, very time consuming and tricky because changes to improve the PM temperature estimation were often to the detriment of the torque estimation. In comparison to the EKF tuning, the KF designs were much easier to accurately calibrate and more straightforward when handling noisy reference signals. By simply introducing an R gain, the KF designs could manage a noisy input signal, while the EKF required retuning of the high-speed noise covarariance matrices.

The 2 kHz sampling frequency which was used for the majority of the simulation analysis, worked well for the KFs, with diminishing return for tests with increased sampling frequency. Using a sampling rate based on the crossover frequency was not necessary for the KF. The sampling frequency required to stabilize the discrete-time EKF using the forward Euler method was extremely high, 163 kHz at $\omega = 3000$ rad/s. Considering the strain that such a high sampling frequency would place on the implemented hardware, state estimation of a mostly unstable discretized system with gain scheduling noise covariance matrices was instead attempted. Even though gain scheduling with respect to the noise covariance matrices was a possible and less hardware-intensive solution, it came at the cost of the robustness of the observer and challenging tuning requirements. The expected improvements from increasing the sampling frequency during simulation tests ap-

peared to be overshadowed by incorrect high-speed noise covariance tuning.

Another vital aspect of the performances for both the KF and EKF was the parameter accuracy, which also was an important factor for the different motor model used in the measurement analysis. The sensitivity analysis showed that estimation results were most sensitive to parameter errors during high torque and low speed operating points, when the currents are large as well. The increased parameter sensitivity during high torque and low speed was, however, somewhat mitigated by the different low-observability estimators. The accuracy of the inductances were important for the flux linkage estimation with greater emphasis placed on L_d, which in turn was essential for the rotor temperature estimation. The L_d parameter errors were, however, not especially pronounced in the torque estimation unlike L_q errors which were important for the torque estimation but not as essential for the PM temperature estimation. The inductance error sensitivity was also evident in the EKF simulation analysis, where the L_q estimation performed considerably better than the L_d estimation and consistently yielded an accurate torque estimation as a results.

Kalman Filter

Low-Speed Estimator

The Bode magnitude plots of the noise transfer functions showed a strong sensitivity to flux linkage process noise at low rotor speeds, when observability also was low. It was also seen during the simulation analysis that without the low-speed estimator the flux linkage estimation spiked, leading to large rotor temperature estimation errors. Letting the flux linkage estimation slowly converge to the coolant temperature was a much better alternative and the low-speed estimator thresholds from the observability Gramian worked fairly well. There is also a balance to consider of allowing the KF to remain active for as much as possible and avoid the more sensitive low-observability region.

Direct and Dynamic Coolant Temperature Designs

The dynamic-T_c KF has a slight bias towards the coolant temperature over the low-observability threshold, but the most pronounced difference between the designs was the direct-T_c KF feedback system for the starting low-speed estimator PM temperature, from when the observability still was high. The low-speed estimator slowly converged to the corresponding flux linkage value of the coolant temperature. Because of the sensitivity of the flux linkage to PM temperature conversion, the flux linkage value for which the dynamic-T_c KF stopped at when the low-speed estimator activated was very important. The low-observability threshold for the dynamic-T_c KF required special attention to avoid strong deceleration near the observability threshold, where the low-speed estimator had trouble correcting the flux linkage estimate. Using different low-observability thresholds and retaining the λ_{m0} working point from before the switch for the dynamic-T_c KF resulted in a similar performance between the two designs. The flux linkage estimation was

worse for the dynamic-T_c KF, but it yielded a slightly better PM temperature estimation with only a minor deterioration of the torque estimate.

LP-Filters
The LP-filters were very important for the signals used as inputs in the LUTs of the model parameters. With filtered current measurement signals the torque estimation-error was substantially reduced and using a full-order state observer should probably be reconsidered. A reduced-order observer that only includes the relevant dynamics to estimate the required states could have a similar performance, but be easier to implement with fewer parameters to tune. The LP-filter to smooth λ_{m0} working point changes was also remarkably essential, because of the sensitivity of the flux linkage to PM temperature conversion, the estimate could otherwise vary considerably.

Normalized System
The observability Gramian of the discrete-time model had a lower condition number than the continuous-time system and by normalizing the system, it started off relatively high but decreased to under 10 already before $\omega = 500$ rad/s. Using a low-speed estimator, it was possible to avoid the region where the condition number was largest. The system without normalization, however, had a condition number of the observability Gramian that started low but increased to 10^4 at maximum rotor speeds. The simulation results for both the KF and the EKF, showed that normalizing the system or rescaling the state variables had a large effect on the noise covariance matrices Q and R settings. The normalized system KF did not need to use an R gain and with slightly larger σ_λ, it gave the best torque and rotor temperature estimation results. The differences were not directly apparent in a simulation environment with very high numerical precision, but it performed well overall.

Extended Kalman Filter

The EKF expanded with inductance estimation showed promise in circumstances where the inductance accuracy was limited. Without a mechanism to accurately update the inductances, the observers had issues in some area of the operating region. The downside, conversely, was a very laborious and sensitive calibration process of the noise covariance matrices. When tuning the EKF with gain scheduling, it was better to try to avoid large R gains, as it would slow down the estimation speed for all states, but if it proved too difficult to only adjust the Q matrix, an R gain was also incorporated. Moreover, the L_q estimation performed much better than expected from any observability analysis, which also resulted in a consistently great torque estimation. An alternative approach could be a reduced-order observer with L_q estimation and focusing on a more accurate LUT for L_d, if there are memory limitations in hardware. The poor L_d estimation, which according to the sensitivity analysis had the greatest affect on the λ and T_r estimation, required heavy estimation change suppression to avoid large PM temperature estimation deviations. This also meant that the flux linkage estimate had trouble accurately following fluctuations caused by varying torques, but using a rate limiter on the torque input for

the λ_{m0} reference point LUT, alleviated the issues for the PM temperature estimation. Attempting to estimate three different parameters from effectively two current equations was possibly a bit ambitious. Luckily, L_d parameter errors did not have a great affect on the torque estimation and the observer performed decently when tuned properly.

Inverted Inductance State Design
The observability Gramian for the discrete-time inverted inductance system had a larger condition number than its standard inductance counterpart and no combination of rescaling factors could be found to reduce the condition number below the rescaled standard inductance design. The interaction of rescaling state variables could be further investigated in the simulation analysis, but finding a combination of scaling factors with a corresponding noise covariance tuning for the standard inductance state design was already challenging. A more fruitful endeavour is most likely an investigation of a more robust discretization method that also can be symbolically differentiated. The process noise covariance settings for the standard inductance design were extremely small and might not be feasible to implement on an embedded system. Even though the default Q settings for the inverted inductance design were more manageable, the high-speed calibration was still very small considering how large the inverted inductance states were.

Rescaled State Variables
The rescaled state variable simulation analysis showed improvement in the torque estimation at a cost of the rotor temperature estimation. The search for possible combinations of scaling factors with corresponding noise covariance matrice calibrations, which improved both the torque and PM temperature estimation, was unsuccessful. The observability analysis for the EKF was, however, limited to a few number of operating points with the maximum speed of $\omega = 3000$ rad/s. The originally chosen scaling factors, found in the EKF design, had high-speed noise covariance calibration troubles when $\omega \geq 3000$ rad/s. The results of the observability analysis were also not directly applicable, because a stable system was required for the observability Gramian, and were generated with a sampling frequency of 163 kHz while the observer only used a 2 kHz sampling frequency. Similar to the normalized system KF, the increased numerical precision was never pertinent to the Matlab Simulink simulation environment, but it could be important for an implementation on an embedded system. Furthermore, the extremely small high-speed Q settings were somewhat alleviated with the rescaled state variables.

High-Speed Noise Covariance Matrix Calibration
When utilizing the forward Euler method to discretize and symbolically differentiate the system, the sampling frequency required to have a stable system for the entire ω operating range was extremely high. The trade-off for using the less computationally demanding method, was an unstable system that required a lot of effort tuning and which was not robust. Without the high-speed calibrations, the overall

suppression has to be very large or the rotor temperature estimation would devolve into large estimation errors, which the torque estimation was surprisingly unaffected by. The tuning was very time consuming and sensitive, but it did give acceptable estimation results for a less computationally resource-intensive design.

Low-Observability Estimator
The original low-observability estimator, based on the dynamic-T_c KF that suspends the P matrix update, improved the PM temperature estimation to the detriment of the torque estimation. The limited observability analysis did not accurately depict how much better the L_q estimation was compared to L_d and an alternative low-observability estimator with unimpeded L_q estimation was used instead. The alternative near standstill estimator had short and relatively large estimation spikes, but the torque estimation performance was overshadowed by the accuracy improvement of the L_q estimation. The LP-filter with comparatively long time constant in the rotor temperature also smoothed the effects caused by the short λ spikes and still yielded an overall improvement compared to not using a low-observability estimator. It was never a concern during the simulation analysis, but a prolonged cool-down period will cause the L_q estimation to drift towards the lower saturation limit. Although the tests with initial-condition errors and saturation limits showed that the states quickly recovered with the default Q and R settings, logic could be introduced to reset the L_q estimate to initial conditions during long cool-down periods.

9.3 Future work

The work can be continued in a number of different avenues, the most readily apparent option is a continuation of the real measurement data analysis. More work has to be done testing all the observer designs, improving the tuning and using measurement data from more tests cycles. There are also potential PWM inverter model inaccuracies that could be investigated. Another option is focusing on implementing the designs on an embedded system, working under stricter hardware limitations and real-time requirements. It then becomes more important to optimize the design, possibly with a reduced-order observer, and being able to handle the introduction of delays. The low-observability design with the temperature estimation slowly converging to the coolant temperature was also very basic and could be further refined, e.g., taking in consideration the current magnitudes during low-observability. There are also a few different options for further EKF developments. Estimating both the inductances was tricky, but only estimating L_q could be a potential workaround, allowing for alternative measures to acquire accurate L_d information. Other, more robust, discretization methods can also be investigated, where the aim is to keep the system stable over the entire ω operating region with reasonable increases in computational demands and also being able to symbolically define the Jacobians.

Bibliography

Alaküla, M., L. Gertmar, and O. Samuelsson (2013). "Elenergiteknik". In: KFS AB, Lund, pp. 47–63, 151–184.

ANSYS Inc (2019). *Motor-CAD integrated multiphysics analysis software for electric motor design*. Last accessed 15 January 2022. URL: https://www.motor-design.com/wp-content/uploads/About-Ansys-Motor-CAD-Brochure.pdf.

Bojoi, R., M. Pastorelli, J. Bottomley, P. Giangrande, and C. Gerada (2013). "Sensorless control of PM motor drives — a technology status review". In: pp. 168–182. ISBN: 978-1-4673-5656-5. DOI: 10.1109/WEMDCD.2013.6525177.

Cheng, D. K. (1989). "Field and wave electromagnetics". In: 2nd ed. Addison-Wesley, Tsinghua, pp. 253, 258, 267–268, 343.

Cho, S.-Y., W.-G. Shin, J.-S. Park, and W.-H. Kim (2018). "A torque compensation control scheme of PMSM considering wide variation of permanent magnet temperature". *IEEE Transactions on Magnetics* **PP**, pp. 1–5. DOI: 10.1109/TMAG.2018.2864649.

DieselNet (2019). *Worldwide harmonized light vehicles test cycle (WLTC)*. Last accessed 15 January 2022. URL: https://dieselnet.com/standards/cycles/wltp.php.

Ding, H., X. Gong, and Y. Gong (2020). "Estimation of rotor temperature of permanent magnet synchronous motor based on model reference fuzzy adaptive control". *Mathematical Problems in Engineering* **2020**, pp. 1–11. DOI: 10.1155/2020/4183706.

Glad, T. and L. Ljung (2003). "Reglerteori flervariabla och olinjära metoder". In: 2nd ed. Studentlitteratur AB, Lund, pp. 59–62, 79–81, 86–87, 144–158, 193–194, 417–420, 500.

Gustafsson, F. (2012). "Statistical sensor fusion". In: 2nd ed. Studentlitteratur AB, Lund, pp. 153–209.

Holst, A. and V. Ufnarovski (2014). "Matrix theory". In: 1st ed. Studentlitteratur AB, Lund, pp. 290–292, 336.

Ichikawa, S., M. Tomita, S. Doki, and S. Okuma (2006). "Sensorless control of synchronous reluctance motors based on extended EMF models considering magnetic saturation with online parameter identification". *IEEE Transactions on Industry Applications* **42**:5, pp. 1264–1274. DOI: 10.1109/TIA.2006.880848.

Kumar, R., S. Das, P. Syam, and A. K. Chattopadhyay (2014). "Review on model reference adaptive system for sensorless vector control of induction motor drives". *IET Journals*. DOI: 10.1049/iet-epa.2014.0220.

Linquip Technews (2020). *Salient pole rotor: learn the features simply with the non-one too*. Last accessed 15 January 2022. URL: https://www.linquip.com/blog/salient-pole-rotor-learn-the-features-simply/.

Linquip Technews (2021). *The beginner's guide to permanent magnet synchronous motors*. Last accessed 15 January 2022. URL: https://www.linquip.com/blog/permanent-magnet-synchronous-motors/.

Massachusetts Institute of Technology (n.d.). *Analysis and design of feedback control systems*. http://web.mit.edu/2.14/www/Handouts/PoleZero.pdf. Last accessed 20 February 2022.

MathWorks (n.d.[a]). *Clarke to park angle transform, implement 0 to dq0 transform*. Last accessed 15 January 2022. URL: https://se.mathworks.com/help/physmod/sps/ref/clarketoparkangletransform.html.

MathWorks (n.d.[b]). *Clarke transform, implement abc to 0 transform*. Last accessed 15 January 2022. URL: https://se.mathworks.com/help/physmod/sps/ref/clarketransform.html.

MathWorks (n.d.[c]). *PMSM, permanent magnet synchronous motor with sinusoidal flux distribution*. Last accessed 15 January 2022. URL: https://se.mathworks.com/help/physmod/sps/ref/pmsm.html.

MathWorks (n.d.[d]). *Simulating thermal effects in rotational and translational actuators*. Last accessed 16 January 2022. URL: https://se.mathworks.com/help/physmod/sps/ug/simulating-thermal-effects-in-rotational-and-translational-actuators.html.

Michael Zeltkevic (1998a). *Forward and backward Euler methods*. https://web.mit.edu/10.001/Web/Course_Notes/Differential_Equations_Notes/node3.html. Last accessed 20 March 2022.

Michael Zeltkevic (1998b). *Predictor-corrector methods*. https://web.mit.edu/10.001/Web/Course_Notes/Differential_Equations_Notes/node7.html. Last accessed 20 March 2022.

Stanford University (2001). *Controllability and observability*. http://floatium.stanford.edu/engr210a/lectures/lecture9_2001_10_30_01.pdf. Last accessed 8 March 2022.

Štulrajter, M., V. Hrabovcová, and M. Franko (2007). "Permanent magnets synchronous motor control theory". *Journal of ELECTRICAL ENGINEERING* **58**, pp. 79–84.

Touhami, S., Y. Bertin, Y. Lefèvre, J.-F. Llibre, C. Hénaux, and M. Fénot (2017). "Lumped parameter thermal model of permanent magnet synchronous machines". *Electrimacs* **2017**, pp. 1–6.

Vyncke, T. J., R. K. Boel, and J. A. Melkebeek (2010). "On the stator flux linkage estimation of an PMSM with Extended Kalman filters". In: DOI: 10.1049/cp.2010.0150.

Wallscheid, O., A. Specht, and J. Böcker (2017). "Observing the permanent-magnet temperature of synchronous motors based on electrical fundamental wave model quantities". *IEEE Transactions on Industrial Electronics* **64**:5, pp. 3921–3929. DOI: 10.1109/TIE.2017.2652363.

Wittenmark, B., K. J. Åström, and K.-E. Årzén (2016). "Computer control: an overview educational version 2016". In: IFAC Professional Brief. International Federation of Automatic Control, pp. 11, 15–23, 39–45.

Zarei, A., K. Abbaszadeh, and K. Safari (2012). "The analytical analysis of the rotor losses in the PMSM motors". In: *Proceedings of the World Congress on Engineering and Computer Science 2012 Vol II WCECS 2012*, pp. 1044–1048.

Lund University
Department of Automatic Control
Box 118
SE-221 00 Lund Sweden

Document name
MASTER'S THESIS

Date of issue
July 2022

Document Number
TFRT-6156

Author(s)
Daniel Mårtensson

Supervisor
Gabriel Turesson, BorgWarner
Peter Jonsson, BorgWarner
Björn Olofsson, Dept. of Automatic Control, Lund University, Sweden
Anders Robertsson, Dept. of Automatic Control, Lund University, Sweden (examiner)

Title and subtitle
Kalman-Filter Design and Evaluation for PMSM Rotor-Temperature Estimation

Abstract
The permanent magnet synchronous motor, PMSM, is an efficient electrical motor that has seen a greater prevalence in the automotive industry from the increasing demand for electrical vehicles. Managing the temperature of the permanent magnet rotor is important to optimize motor utilization and avoid hardware failures. Direct temperature measurements of the moving rotor with a sensor are, however, both difficult and costly and an observer-based approach to estimate the rotor temperature can instead be attained using measured currents, voltages and a model.

The work in this thesis studies observers based on a Kalman Filter, KF, and an extended Kalman filter, EKF. The observability of the system was found to be poor at low rotational speeds and filter designs were implemented that used low-speed estimators, that slowly drive the rotor temperature estimate towards the coolant temperature. For circumstances when the inductance accuracy in the model was limited, EKFs with inductance estimation and gain scheduled noise covariance matrices were also evaluated. There were also potential numerical robustness issues, so normalized and rescaled state variable system descriptions were evaluated.

The simulation analysis of the KFs showed a great reduction in rotor temperature estimation error of roughly 40°C when using a low-speed estimator, compared to without the use of a low-speed estimator. In circumstances with limited inductance accuracy, the EKF with inductance estimation had a maximum temperature estimation error magnitude of ≈2.5°C compared to ≈11°C of the KF design. Using an EKF with lower sampling frequency and gain scheduling did, however, come at the cost of robustness. Normalizing or rescaling state variables had a visible effect on the noise covariance settings but did not show noticeable improvements of the computational robustness in a simulation environment with high numerical precision.

The thesis was concluded with a brief analysis using measurement from a real but different motor model. The worst case estimation error magnitudes was approximately 12°C for the rotor temperature. The estimation results were very sensitive to model parameter accuracy and more testing has to be conducted using experimental data, but the results presented show some promise.

Keywords

Classification system and/or index terms (if any)

Supplementary bibliographical information

ISSN and key title
0280-5316

ISBN

Language
English

Number of pages
1-137

Recipient's notes

Security classification